LBL-749
c.1

THE INCLUSIVE REACTIONS $pp \to \pi^{\pm}$ + ANYTHING AND $pp \to p$ + ANYTHING AT 6.6 GeV/c COMPARED TO HIGHER ENERGIES

Eugene Ralph Gellert
(Ph. D. Thesis)

October 27, 1972

Prepared for the U.S. Atomic Energy Commission under Contract W-7405-ENG-48

LBL-749
c.1

DISCLAIMER

THE INCLUSIVE REACTIONS $pp \rightarrow \pi^{\pm}$ + anything AND $pp \rightarrow p$ + anything AT 6.6 GEV/C COMPARED TO HIGHER ENERGIES

Eugene Ralph Gellert
Lawrence Berkeley Laboratory
University of California
Berkeley, California 94720

October 27, 1972

ABSTRACT

The π^-, π^+, and proton inclusive distributions resulting from the exposure of a liquid-hydrogen bubble-chamber to a 6.6 GeV/c proton beam are studied and compared to higher energies. In the target region (Feynman's $\underline{x} < -0.4$) the π^- laboratory differential-cross-section is found to be energy independent, provided that $p_\perp < 0.6$ GeV/c. However, the structure function $\rho(x,p_\perp,s) = Ed^3\sigma/dp^3$ is found not to be energy independent in the central region ($p^*_{||} \approx 0$), but the non-scaling term is consistent with $s^{-\frac{1}{4}}$ dependence. The π^+ spectra behave quite differently. In the target region the π^+ laboratory differential-cross-section is found to exceed that at higher energies, whereas in the central region ρ is found to be energy independent for small transverse momentum, at least in incident momentum interval 6.6 to 28.5 GeV/c. For protons ρ is found to decline with energy in the interval 6.6 to 24 GeV/c (and possibly to ISR energies and above) in <u>both</u> the target and central region, with the greatest decline occurring in the central region. Graphs of various single and double differential cross sections are presented.

THE INCLUSIVE REACTIONS $pp \rightarrow \pi^{\pm}$ + anything AND $pp \rightarrow p$ + anything AT 6.6 GEV/C COMPARED TO HIGHER ENERGIES

Contents

LIST OF TABLES

LIST OF FIGURES

Please note: The automatic plotting system used for most of the graphs presented here considers the data point to be at the apex of the triangle symbols, viz. △ and ▽ . It is at the center of all other symbols, viz. ⊡ , ◇ , -•-, etc. (The data point is at the center of the triangle symbol in the hand-drawn fig. IV.4. This is probably also true for figs. IV.6 and V.4, 6, and 8, which were copied photographically from published sources.)

I. INTRODUCTION

In this paper we present single particle spectra for the inclusive reactions $pp \rightarrow \pi^{\pm}$ + anything and $pp \rightarrow p$ + anything at 6.6 GeV/c. These spectra are compared with higher energy experiments in order to determine if pionization and limiting fragmentation occur at energies as low as 6.6 GeV/c.

Section II presents a brief theoretical background on the subject of inclusive reactions and defines many of the variables used in the remainder of the paper.

Section III discusses the various experimental procedures, including the separation of π^+'s and protons. Cross sections are presented in this section.

Section IV reports on the π^- spectra. Some of the results presented here have already been reported in an earlier paper (Ge-2).

Section V reports on the π^+ and proton spectra. The results reported in a preliminary paper on the proton spectra are not repeated here (Ab-2).

Finally, a brief summary of our results, together with the conclusions of this experiment, is given in section VI.

II. THEORETICAL BACKGROUND AND CHOICE OF VARIABLES

A. Introductory Remarks

In this section we only touch on the many theoretical papers which have come out on the subject of inclusive reactions. We mention those predictions of the various theories which can be tested by our data, and we discuss the variables normally used to study these theories. The reader interested in a thorough treatment should consult one of the review articles which have appeared recently (Be-7, Fr-1, Qu-1, Ra-1, Yo-2). Two extensive data compilations have also appeared recently (Di-1, La-1), and there are several conference proceedings devoted primarily or entirely to inclusive reactions (Da-2, Ox-2).

B. The appropriate Independent Variables

1. General Comments

Let us consider the reaction $pp \rightarrow \pi^- +$ anything. If we ignore the internal properties of the blob recoiling against the π^-, there are four kinematical variables needed to describe this reaction. It is usual to chose as one of these four variables $E_{C.M.}$, the center-of-momentum energy of the entire system (or, equivalently, the incident momentum, P_{beam}, or s, the Mandelstam variable). It is also usual to use the three components of the π^- momentum for the remaining three variables. In the center-of-momentum cylindrical coordinate system these three variables are: $p^*_{\parallel}$, the momentum component parallel to the incident beam direction; $p_\perp$, the momentum component perpendicular to the incident beam direction; and ϕ, the azimuthal angle about the

incident beam direction. (If the possibility of confusion exists as to whether a variable is to be evaluated in the C.M. or the laboratory system, following Frazer (Fr-1), we shall designate by v^* the C.M. value of the variable, and we shall designate by v or v (lab) the value of the variable in the laboratory system.) Of course, because both our beam and target are unpolarized, no structure is possible in the azimuthal angle, unless there are experimental biases. We therefore suppress the variable ϕ in the remainder of this paper.

If one wants to compare distributions at different incident energies in the hope that these distributions might be equal, it seems reasonable to chose a set of two π^- momentum variables for which most of the data are in same domain, independent of the incident energy. Therefore, because of the well known limiting nature of the $p_\perp$ distribution, we use $p_\perp$ and for the longitudinal variable $p_{||}$(lab) or the scaling variables $\underline{x}$ or $\underline{y}$ (defined later).

It should be pointed out that other authors do chose other variables. For example, the choice M_{blob}, $t_{beam,\ blob}$, and $\underline{s}$ is often made in connection with Regge models. Scaling in $\underline{x}$ (defined in the next section) and $p_\perp$ definitely implies sealing in t and M^2/s, for certain regions of phase space. We shall not pursue these other possibilities however.

2. Different Definitions of Feynman's x.

In his paper on the parton-bremsstrahlung-model, Feynman has defined a variable $\underline{x}$ by the equation $\underline{x} = 2p^*_{||}/s^{1/2}$, in order to study the pionization region (i.e. $\underline{x} \approx 0$) (Fe-1). Other papers define slightly different x's, all equivalent at the high energies at which Feynman's theory was developed. In order to avoid confusion, we shall refer to these slightly different $\underline{x}$'s by the use of subscripts; we define

$$x_1 = 2p^*_{\parallel}/s^{1/2} = p^*_{\parallel}/E^*_0 \qquad \text{II.B.1}$$

$$x_2 = p^*_{\parallel}/P^*_0 \qquad \text{II.B.2}$$

$$x_3 = p^*_{\parallel}/p^*_{max} \qquad \text{II.B.3}$$

$$x_4 = p^*_{\parallel}/p^*_{\parallel,\,max}(p_\perp) \qquad \text{II.B.4}$$

where E^*_0 and P^*_0 are the C. M. energy and momentum, respectively, of either of the incident protons; p^*_{max} is the absolute maximum C. M. momentum of the π^- for a given value of $\underline{s}$ ($P^*_{max} \equiv P^*_0$ and therefore $x_2 \equiv x_3$ for an outgoing proton); and $p^*_{\parallel,\,max}(p_\perp)$ is the maximum value of $p^*_{\parallel}$ for a given $\underline{s}$ and $p_\perp$.

It is immediately obvious that all four definitions are essentially identical at high energies. However, this is far from true at our low energy of 6.6 GeV/c (table 1).

Because x_2 has become the most popular definition of $\underline{x}$, our more recently made plots are presented in terms of this variable. We warn the reader that some of our earlier plots are presented in terms of x_3, however.

3. Plots in the Laboratory

Benecke, Chou, Yang, and Yen work in the lab. or beam rest frame, since these frames are most appropriate for their beam and target fragmentation picture (Be-1). Because of the symmetry between target and beam in our proton-proton experiment, these two frames are equivalent, and we simply plot our distributions in terms of $p_{\parallel}$ (lab) in order to compare with this theory.

Table II.1 Values of the 4 different x's for 2 different values of $p_\perp$ and $p_{\parallel}^*$ for π^- from $pp \to \pi^- +$ anything at 6.6 Gev/c.

$p_\perp$ (Gev/c)	$p_{\parallel}^*$ (Gev/c)	x_1 [a]	x_2 [a]	x_3 [a]	x_4 [a]
0.0	1.546 [b]	0.71	0.82	1.00	1.00
0.5	1.250 [c]	0.66	0.76	0.92	1.00

a. See Eqn. s III.B.1 to III.B.4 for the definitions of x_1 to x_4. This table does not apply to π^+ and proton production.

b. i.e. $p_{\parallel}^* = p_{max}^*(\pi^-)$

c. i.e. $p_{\parallel}^* = \left\{ \left[p_{max}^* (\pi^-) \right]^2 - p_\perp^2 (\pi^-) \right\}^{1/2}$

4. Rapidity

Another frequently used longitudinal variable is the rapidity, y (Fe-1, Wi-1). It can be defined in any of the following equivalent ways in any frame.

$$y = \tfrac{1}{2} \ell n \left[(E+p_{\parallel}) / (E-p_{\parallel}) \right] \qquad \text{II.B.7a}$$

$$= \ell n \left\{ \left[p_{\parallel} + (p_{\parallel}^2 + \mu^2)^{1/2} \right] / \mu \right\} = \sinh^{-1}(p_{\parallel}/\mu) \qquad \text{II.B.7b}$$

$$= \tanh^{-1}(p_{\parallel}/E) \qquad \text{II.B.7c}$$

where the longitudinal mass $\mu = (m^2 + p_\perp^2)^{1/2}$. II.B.7d

This variable has the useful property that a change in Lorentz frames is accomplished merely by the addition of a constant to all values of y, so that all frames are put on an essentially equivalent basis.

We also note that the rapidity is a function only of a particle's longitudinal velocity, $\beta_{\parallel}$. We can see this by substituting the well known relations

$$\bar{\gamma} = E/m$$

$$\text{and } \vec{\eta} = \vec{\beta}\bar{\gamma} = \vec{P}/m$$

into equation 7a. The result is

$$y = \tfrac{1}{2}\ln\left[(1+\beta_{\parallel})/(1-\beta_{\parallel})\right]. \qquad \text{II.B.8}$$

Because y is a monotonically increasing function of the longitudinal velocity, it is called the rapidity.

C. Testing Scaling and Limiting Fragmentation models

Following Frazer (Fr-1), we define an invariant production-cross-section by:

$$\rho(p_{\parallel}, p_{\perp}, s) = Ed^3\sigma/dp^3 \qquad \text{II.C.1}$$

where E and p are the energy and momentum of the outgoing particle in question (in this case the π^-) in the frame of interest and s is the Mandelstam variable which is equal to the invariant mass squared of the entire reaction. The function ρ is invariant under Lorentz transformations, and removes an uninteresting phase-space factor, E.

According to the scaling hypothesis, which Feynman develops from his parton-bremsstrahlung-model (Fe-1), the function $\rho(p^*_{\parallel}, p_{\perp}, s)$ actually only depends on $p_{\perp}$ and x (see III.B for a discussion of the various x's), that is

$$\rho(p^*_{\parallel}, p_{\perp}, s) = \rho(x, p_{\perp}). \qquad \text{II.C.2}$$

On the other hand, according to the limiting-distribution hypothesis of Benecke, Chou, Yang, and Yen (Be-1), ρ approaches an asymptotic limit for large s given by:

$$\rho(p_{\parallel}, p_{\perp}, s) = \rho(p_{\parallel}, p_{\perp}) \qquad \text{II.C.3}$$

provided that $p_{\parallel}$(lab) does not carry a significant fraction of the energy $s^{1/2}$. Both models have been shown to be equivalent at high energies (Ve-1).

If we average the differential cross section over the uninteresting azimuth angle ϕ, we obtain:

$$\frac{d^3\sigma}{dp^3} = \frac{1}{2\pi p_{\perp}} \frac{d^2\sigma}{dp_{\perp} dp_{\parallel}} . \qquad \text{II.C.4}$$

Equations 1 and 4 are combined to yeild:

$$\rho(p_{\parallel}, p_{\perp}, s) = \frac{(p_{\parallel}^2 + p_{\perp}^2 + m^2)^{1/2}}{2\pi p_{\perp}} \frac{d^2\sigma}{dp_{\perp} dp_{\parallel}} \qquad \text{II.C.5}$$

where m is the mass of the outgoing particle.

From equations 5 and 3, it is evident that the content of equation 3 can equally well be expressed by the statement that the laboratory differential-cross-section is independent of the total C.M. energy of the reaction, $s^{1/2}$, for small values of $p_{\parallel}$, that is:

$$\frac{d^2\sigma}{dp_{\perp} dp_{\parallel}} (p_{\parallel}, p_{\perp}, s) = \frac{d^2\sigma}{dp_{\perp} dp_{\parallel}} (p_{\parallel}, p_{\perp}) \qquad \text{II.C.6}$$

This is the form in which the limiting-distribution hypothesis was stated by BCYY (Be-1). (It is only when we compare distributions at different $p_{\parallel}$, for example, when we compare distributions having the same $p_{\perp}$ and x (eq. 2), that it is important to use ρ rather than the ordinary differential cross section, in order to eliminate an uninteresting phase space factor.)

Obviously we can integrate equation 6 over all $p_{\perp}$. Now it is true that the limits of integration depend on s (for the π^-

$$p_{\perp,max} = \frac{1}{2s^{\frac{1}{2}}} \left[s + m_{\pi}^2 - (2m_p + m_{\pi+})^2 \right] \approx \frac{1}{2} s^{\frac{1}{2}}$$

at high energies). However it is well known that $d^2\sigma/dp_\perp dp_{||}$ is very small at large $p_\perp$. Therefore even at infinite energies the integral between $p_{\perp,max}$ for our experiment and $p_{\perp,max}$ at infinite energies is completely negligible. Thus, integrating equation 6 yields.

$$\frac{d\sigma}{dp_{||}}(p_{||},s) = \frac{d\sigma}{dp_{||}}(p_{||}). \qquad \text{II.C.7}$$

We also define a function $\underline{F}$ by the equation:

$$F(p^*_{||}, s) = \int_0^{p^2_{\perp max}} \rho(p^*_{||}, p_\perp, s)\, dp^2_\perp \qquad \text{II.C.8}$$

According to the previous discussion, scaling (eqn. 2) implies that $\underline{F}$ depends only upon $\underline{x}$, i.e. scaling implies the relation:

$$F(p^*_{||}, s) = F(x) \qquad \text{II.C.9}$$

Similarly, we define a function $B(y,s)$, where $\underline{y}$ is the rapidity defined by equations II.B.7, by the relation

$$B(y,s) = \int_0^{p^2_{\perp}, max} \rho(y, p_\perp, s)\, dp^2_\perp . \qquad \text{II.C.10}$$

The limiting-distribution hypothesis of BCYY implies that: $B(y,s) = B(y)$. II.C.11

We note that equations II.B.7 and II.C.5 can be combined to yeild

$$\rho = (c/\pi) d^2\sigma/dydp_\perp \qquad \text{II.C.12}$$

and therefore

$$B = (c/\pi) d\sigma/dy \qquad \text{II.C.13}$$

This last relation is very useful for relating the number of particles produced at a given energy to the value of ρ.

Of course we can also integrate ρ over all x. We define

$$G_j(p_\perp, s) = \int_{x_{j,min}}^{x_{j,max}} \rho \, dx_j \qquad \text{II.C.14}$$

(see the previous section for a discussion of the different definitions of $\underline{x}$). Therefore scaling (eqn. 2) implies that

$$G(p_\perp, s) = G(p_\perp). \qquad \text{II.C.15}$$

D. $s^{-\frac{1}{4}}$ Dependence Near x = 0

If a three - particle elastic - scattering Mueller graph is relevant for the description of the central region (Mu-2), Abarbanel (Ab-1) showed that we can write

$$\rho(p_{\parallel}^* = 0, p_\perp, s) = f(p_\perp) - g(p_\perp) s^{-\frac{1}{4}} \qquad \text{II.D.1}$$

This equation can be integrated to yield

$$F(p_{\parallel}^* = 0, s) = \int_0^\infty \rho \, d\vec{p}_\perp^{\,2} = a - b s^{-1/4} \qquad \text{II.D.2}$$

We may divide by $\sigma_{T\infty}$ (and multiply by π) to obtain

$$F_F(p_{\parallel}^* = 0, s) = \frac{\pi}{\sigma_{T\infty}} \int \rho \, dp_\perp^{\,2} = c - d' s^{-\frac{1}{4}} \qquad \text{II.D.3}$$

or, because

$$s = 2m_{tgt}E_{bm} + m_{tgt}^2 + m_{bm}^2$$

$$\approx 2m_{tgt}P_{bm} \quad \text{if } P_{bm} >> m_{tgt} \text{ and } m_{bm}$$

We can also write

$$F_F(p_{\parallel}^* = 0, s) = c - dP_{bm}^{-1/4} \qquad \text{II.D.4}$$

Because of the factorizibility of the Regge amplitude when $s \to \infty$, $\underline{c}$ should be a universal constant.

Ferbel recently published a plot of F_F vs $P_{bm}^{-\frac{1}{4}}$ for several reactions, using the worlds published data (Fe-2). It strongly supports the idea that $\underline{c} = 0.76 \pm 0.05$ describes all the reaction $xp \to \pi$ + anything.

III. EXPERIMENTAL PROCEDURES

A. The Exposure

From mid-August to November 1, 1965, we exposed the Alvarez 72-inch liquid-hydrogen bubble-chamber to 6.6 and 5.4 GeV/c protons from the Bevatron external-beam (We-1). We took a total of 493,000 pictures at both energies (table 1). All 493,000 pictures were scanned and measured for events with strange-particle signatures (that is events with V's or decays of some of the charged tracks). However, less than half the 6.6 sample was scanned and measured for 2,4, and 6-prong events with non-strange signatures, because of the much larger cross-sections for these events (table 5). Also, the 5.4 GeV/c sample was not scanned for non-strange events.

The results of investigating various exclusive reactions contained in this data have been reported elsewhere (see ref. Ge-1, Be-12, Co-1 to 6, Du-1 & 2, and Ma-2). They will not be discussed here.

B. The Beam-Line

Our beam-line was originally set up by William Chinowsky for a 6.0 GeV/c proton-proton experiment, and was slightly modified for our experiment - by the addition of another collimating slit, spectrometer, and quadrapole magnet - by Gerald Allen Smith and Arthur Barry Wicklund (Ki-1, Du-1).

C. The Beam-Momentum Determination

Both the average incident momentum, $\bar{p}$, and the spread in

Table III.1 The proton exposure

	Nominal momentum		
	5.4 GeV/c	6.6 GeV/c	Total
No. of pictures	142 000	351 000	493 000
Total path length on film (events/μb)	6.1±0.2	14.7±0.4	20.8±0.45
Rolls of film (total)	215	518	733
Rolls scanned and measured for:			
2-prongs	0	65	65
4-prongs	0	138	138
6-prongs	0	226	226
(both 4- and 6-prongs	0	71	71)
8-prongs	0	24	24
10-prongs	0	24	24
Strange particles	215	518	733
Events measured and fitted for:			
2-prongs	0	23 385	23 385
4-prongs	0	37 052	37 052
6-prongs	0	3 636	3 636
8-prongs	0	0	0
10-prongs	0	0	0

momentum, Δ p, are determined by measuring the curvature of long tracks in the hydrogen bubble-chamber with the Franckenstein measuring machines. We find, that when the beam first becomes visible in the bubble chamber, it has an average momentum of 6.607 GeV/c for the 6.6 exposure, and 5.423 GeV/c for the 5.4 exposure (table 2). The momentum changed from time to time during the film taking. These changes, which averaged $\pm$20 MeV/c, seem to have occurred when magnets M3 and Q3 and the beam defining collimator (called the uranium mass slit on the layout drawings) were moved in order to get the beam to enter the center of the vacumn tank window. This was necessary because the beam was aimed somewhat high during the early part of our run, so that many of the beam particles missed the vacuum tank window and went through 1 1/2 to 3 inches of steel (table 2). Also, during the first few rolls, the current in M1 and M2 was varied, with a resulting change in momentum of about $\pm$ 100 MeV/c. (Fig. 1 or ref. Du-1 is a diagram of the beam layout.)

Each event was measured on the Franckenstein, SMP, or Spiral Reader (table 3), and processed through the programs POOH or PANAL, TVGP, and SQUAW (the two prongs were processed through SIOUX instead of TVGP and SQUAW) (Po-1, Al-1, So-1, Da-3).

Considerable errors are introduced if one uses the measured beam momentum for each event, rather than the "beam average" momentum. In table 4, we compare the "beam average" momentum with the value of the beam momentum obtained when some events of the 4-prong sample are fit to the best kinematic hypothesis (including the missing-mass hypothesis) using only measured momenta as input. We observe a considerable spread in momentum. The very large spread in momentum for Spiral Reader I is clearly due to the fact that we can measure, at most, 40 cm. of the beam track on that machine. The shift in momentum for the SMP's and Spiral Reader can be

Table III.2 Beam-momenta for this experiment[a]
(all momenta are in MeV/c

		Nominal momentum 5400 Normal beam	6600 Normal beam	6600 High[b] beam
Δp				
1.	Average measured spread for each roll-interval	±39	±35	±49
2.	Momentum bite determined from bean optics	≈±30	≈ ±30	≈ ±30[c]
3.	Average difference in momentum between different groups of rolls	0	±20	±20[d]
$\bar{p}$				
4.	Average momentum at y = -85.95 cm. (beginning of bubble-chamber visible region)	5423	6607	6568
5.	Average momentum at y = 0[e] (center of bubble-chamber)	5402	6586	6547

a. All quantities (except no.2) are determined by the measurement of long tracks on the Franckenstein.

b. These are protons that came in above the vacuum - tank window, and therefore went through $1\frac{1}{2}$ to 3 inches of stainless steel. This column is only computed for the first 109 rolls, where the entire beam was aimed high and therefore a substantial number of protons are in this category. These events are used in this paper.

c. If the coulomb scattering in $1\frac{1}{2}$ to 3 inches of steel is added to this number, it will agree with the measured spread (item no.1).

d. These values do not include the effects of the six tun-up rolls taken at 6510 and 6705 (normal beam) (6545 and 6675 for the high protons).

e. This quantity is computed by subtracting a 0.248 MeV/c per cm. energy loss in hydrogen (from Pa-1).

Table III.3 Measuring machines used for this experiment

Topology	Per cent of events of each topology measured on each machine		
	Franck-ensteins	SMP'S	Spiral Reader I (40cm radius)	Spiral Reader II (80cm radius)
2-prongs	0 %[a]	0 %	32 %	68 %
4-prongs	~ 50	$\lesssim$ 10	40	0
6-prongs	100	0	0	0
Strange Particles	100	0	0	0

a. except for re-measurements which were done on the Franckenstein's, but are not part of the sample reported in this paper, because there is no ionization information available for them.

Table III.4 Deviation of the fitted momentum from the beam average value[a]

Measuring machine	Shift in[b] P_{fitted} (MeV/c)	Spread in[c] P_{fitted} (MeV/c)	Avg. error[d] assumed in TVGP (MeV/c)
Franckenstein	22	±92	±78
S.M.P.'s	76	±245	±135
Spiral Reader I (40 cm. radius)	-65	±403	±174

a. The beam average value of the momentum at bubble-chamber coordinate y = -85.95 is the value obtained from the measurement of long tracks. This is a roll dependent quantity.

The fitted momenta are the values of momenta obtained from fitting 4-prongs (all constraint classes) for a sample of events processed without the beam-averaging procedure. A correction is made for energy loss in order to calculate the values at bubble-chamber coordinate y = -85.95.

b. the average value of $P_{fitted} - P_{beam\ avg.}$

c. the spread in the distribution $P_{fitted} - P_{beam\ avg.}$

d. the average value of the distribution of TVGP assumed errors for this same sample of events.

explained by optical distortions in these machines, if these distortions have not been fully corrected for. In fact the Spiral Reader had a bent mirror at one time (Ga-5). The Franckenstein measures in the film plane, and should not be subject to optical distortion. We assume that the shift in momentum for events measured on the Franckenstein was due to distortions in the bubble chamber optical system. Since these distortions affect both the "beam average" and fitted momentum, we cannot be certain which is correct.

A beam average procedure was employed in this experiment, using the roll-dependent average beam momentum determined from the previously mentioned long-track study.

We have included this section for purposes of completeness. However, we point out that errors in the beam momentum determination, or in the determination of the momentum of outgoing fast tracks, should have very little effect on the results presented in this thesis. This is because most of the positive tracks we plot are in the backward C.M. hemisphere, and most of the π^-'s do not go too fast in the lab. (section G). It is easy to measure the momentum of such tracks fairly accurately. Also, we depend mainly on ionization, rather than kinematic fitting, to identify the particle mass assignments for each track.

The underestimation of errors in TVGP, one instance of which is shown in table 4, has caused our caluclation of the confidence level to be too low. This means that some good fits were thrown out or fit to lower constraint class reactions (the actual confidence level cutoff was 2 to 3 %, and even higher for four constraint events measured on the Spiral Reader). However, because we normalize our events to the prong

cross sections (and the elastic cross section) (see section D), this fact should not introduce any error into the inclusive distributions presented in this paper. A small error of about 3 °/o may well be introduced into distributions plotted for different exclusive reactions, however.

D. Topological Cross-Sections

The 2-prong eleastic and inelastic cross sections, and the 4-prong cross section for this experiment, have already been reported by E. Colton (Co-1). We briefly summarize his procedure here.

(1) A 10 roll sample, consisting of 7209 usable frames is selected for investigation.

(2) The path length is determined by looking at 1/10 of these frames - 722 frames to be exact. The total number of beam tracks on these frames is counted (a double scan procedure is employed), and the number of interactions is calculated according to the usual formula

$$N_{int} = N_{BT}(1 - e^{-\rho\sigma x})$$

where N_{int} is the number of interactions of all kinds, N_{BT} is the number of beam tracks, ρ is the density of the liquid hydrogen in the bubble chamber, σ is the total pp cross section at 6.6 GeV/c, determined from the world data (41± 1mb.) and x is the length of the fiducial volume scanned. The path length for these 722 frames was therefore N_{int}/σ. As a check, the number of interactions on these frames are also counted, yielding a cross section of 43.6±1.7mb. A double scan was performed which yielded a 99.3 °/o efficiency for both scans. This number was taken into account in determining the cross section.

(5) All the events found are then measured on the SMP's, and processed through TVGP and SQUAW. The elastic events are identified through kinematic fitting, and subtracted from the total 2-prong sample, to obtain the 2-prong inelastic cross section.

The 2-prong inelastic cross section and the 4-prong cross section found by the above procedure are listed in table 5. They agree with the world data (Ha-1). Further calculations must be performed in order to obtain the elastic, and therefore the total 2-prong cross section, however. This is because proton tracks below 100 MeV/c cannot be seen in the bubble chamber. Because the elastic events are extremely peripheral, many of them fall into this category. Also, protons in the 100 to 250 MeV/c range cannot be seen if they have relatively large transverse momentum (required by kinematics for the elastic events) and are dipping or rising. This is quite obvious if we make a scatter plot of the laboratory momentum, p, against the azimuth angle about the beam direction, φ (fig. 1). The result of this loss is a dip in $d\sigma/dt$ near $t = 0$ for the elastic events (fig. 18 of ref. Co-1). Colton finds that a good straight line fit can be made to the data for $t < -0.05$ and the optical point at $t=0$, if we assume that the real part of the forward scattering amplitude is zero. Colton then uses this fit to correct his data, yeilding an elastic cross section of 10.16±0.55 mb. However, at 6.8 GeV/c, Foley et al. obtained an elastic cross section of 11.79±0.22mb (Fo-1), and cross sections at nearby energies are also in this range (Ha-1). Also, as Colton points out, Foley et al. have determined that the ratio of the real to the imaginary part of the scattering amplitude in the vicinity of 6.6 GeV/c is close to -0.33 for t=0 (Fo-2). Therefore

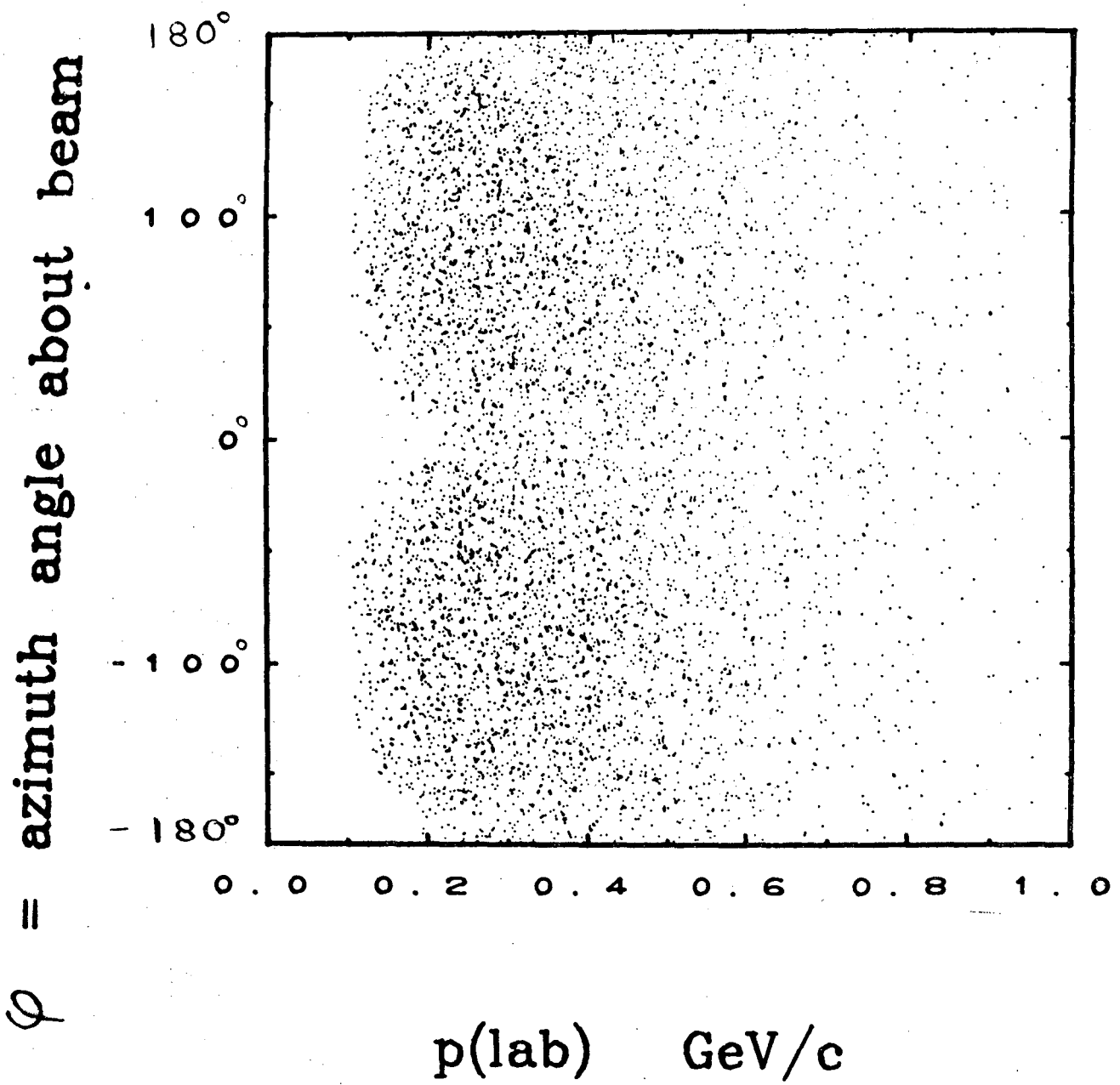

Fig. III.1 Azimuth angle about the incident beam direction for protons produced in the elastic reaction pp → pp at 6.6 GeV/c. Straight up (toward the cameras) is 0°, and 90° is in the horizontal plane.

$$d\sigma/d\Omega = |Re(f)|^2 + |Im(f)|^2$$

so that at $\theta = 0$

$$d\sigma/d\Omega = |Im\ f(0)|^2 \left[1 + 0.33^2\right] = 1.11\ |Im\ f(0)|^2$$

Raising the entire curve on fig. 18 of ref. Co-1 by this 11 °/o is still consistent with the data, and results in an elastic cross section of 11.28±0.61 mb, in agreement with the world's data. However, since the cross section is more accurately determined in other experiments, we use the value of Foley et al. (11.79 ± 0.22 mb) in calculating the 2-prong cross sections in this paper.

[One plot (fig. V.10a) was made using 10.16 mb as the value of the elastic cross section. We have not bothered to correct this plot, but the reader can do so by multiplying all the elastic points by 11.79/10.16.]

We determined the 6 to 4-prong ratio by scanning selected rolls of film for both 4 and 6-prongs. Unfortunately, the scanning of this sample was not as accurate as it might have been. From the second scan and check scans we were able to estimate the maximum error introduced in the 6 to 4-prong ratio by this inaccuracy. This error was much greater than the statistical error in the number of 6-prong events, and is essentially the entire error quoted for this ratio in table 5.

The 6-prong cross section is then determined by multipling this ratio by the previously determined 4-prong cross section.

The eight and ten prong cross sections are determined in the same way. Here, there are so few events, that only the statistical errors are given.

Table III.5 Topological Cross Sections and related quantities at 6.6 GeV/c

Topology	Cross Sections[a] (mb)	
Total cross section[b]	41	± 1
Total inelastic-cross-section[c]	28.8	± 0.8
2-prongs		
elastic[d]	11.79	± 0.22
inelastic[e]	16.83	± 0.70
total[f]	28.62	± 0.73
4-prongs[g]	10.50	± 0.46
6-prongs[h]	0.727	± 0.094
8-prongs[i]	0.022	± 0.008
10-prongs[i]	0.009	± 0.005
Strange particles[j]	0.674	
	Cross Section Ratios	
$\sigma_{6\text{-prong}}/\sigma_{4\text{-prong}}$[h]	0.0692	± 0.0084
$\sigma_{8\text{-prong}}/\sigma_{4\text{-prong}}$[i]	0.0021	± 0.0008
$\sigma_{10\text{-prong}}/\sigma_{4\text{-prong}}$[i]	0.0009	± 0.0005
	Events remaining after fiducial criteria are imposed[k]	
2-prongs		
elastic	6286	
inelastic	12908	
total	19194	
4-prongs	25535	
6-prongs	2750	
	Path length after fiducial criteria are imposed (events/μb)[k]	
2-prongs		
elastic	0.619	
inelastic	0.767	
total	0.711	
4-prongs	2.43	
6-prongs	3.78	

Table III.5 (continued)

a. Dalitz pairs do not make an important contribution to any of the cross sections presented here. (see appendix A)

b. from other experiments - see Ha-1

c. the sum of all the topological cross sections listed below except the elastic cross section.

d. from Fo-1 for 6.8 GeV/c. See text for why our value was not used.

e. calculated from the results reported in ref. Co-1

f. sum of elastic and inelastic 2-prongs

g. from ref. Co-1

h. The error in $\sigma_{\text{6-prong}} / \sigma_{\text{4-prong}}$ is almost entirely the result of uncertainties in scanning efficiency, not the statistical error in the number of events scanned. The 6-prong cross section was obtained by multiplying this ratio by the 4-prong cross section. The error in the 6-prong cross section thus obtained is due almost entirely to the error in this ratio.

i. The error presented is essentially the result of the statistical error of 7 and 3 events (for the 8-prongs and 10-prongs, respectively); no attempt was made to estimate the scanning biases.

j. Arthur Barry Wicklund (Argonne Nat'l Lab.), personal communication, 1968. He also reports that the strange particle cross section at 5.4 GeV/c is 0.624 mb.

k. refers only to the fiducial criteria used for this paper

Contamination by Dalitz-pairs does not affect any of the results presented in this paper (see appendix A).

In order to insure that there is a reasonable amount of track to measure, we restrict the volume of the bubble chamber in which the interaction must take place. Along the beam direction, there is a about 170 cm. length over which an interaction is visible. Our most severe volume cut (in terms of the number of events lost) restricts the allowed region for the interaction vertex to the central 120 cm of this length. Restrictions are also placed on the other two dimensions.

To eliminate non-beam events, the beam momentum is restricted to be between 6350 and 6850 MeV/c, and the entering angle is restricted to being within 5 degrees of the average entering angle.

We found that this fiducial cut significantly improved the accuracy of our measured momentum.

The effect of this cut on the total number of events in the physics sample can be seen by comparing tables 1 and 5.

The path lengths listed in tables 1 and 5 were determined from the cross sections reported in table 5.

E. Cross Sections by Constraint Class and the Number of π's in the Final State

The only unseen hadrons produced in appreciable quantities are π's and neutrons. We shall ignore the small amount of photons which are produced, for example, by η decay. We shall also ignore deuteron and kaon final states. Since the only final state particles are therefore pions, neutrons, and protons, it is obvious that adding a neutral particle means increasing the number of pions by one for any given topology (refer to table B.1).

We present below, a table of cross sections by constraint class and number of pions. These numbers came from ref. Co-1 whenever possible, except for the previously discussed case of the elastic cross section. Rough estimates were made of the other numbers.

Table III.6 Cross Sections by constraint class and number of π's (mb)

No. of constraints	2-prongs	4-prongs	6-prongs
4	11.8±0.2 (0π)	3.0±0.2 (2π)	0.28±0.04(4π)
1	7.0±0.3 (1π)	5.1±0.4 (3π)	0.40±0.06(5π)
0	9.9±0.6(≥2π)	2.4±0.4(≥4π)	0.05±0.03(≥6π)
Total	28.7±0.9	10.5±0.5	0.73±0.09

F. How the Plots Are Made

Each track is assigned a weight, consisting of the product of three numbers, as will be explained below. Denote the weight for track $\underline{i}$ by w_i. For each plot that we wish to make, we accumulate histograms of w_i and w_i^2. The $\underline{w}$ histogram gives the value of the data points and the square root of the w^2 histogram gives the error of the data points. (Actually, we add a typical track to the w^2 histogram. This means that our error corresponds to $(n+1)^{\frac{1}{2}}$ rather than $n^{\frac{1}{2}}$, where n is the number of events per bin. This is a more correct procedure if $\underline{n}$ is experimentally determined rather than theoretically predicted.)

In the following discussion we suppress the subscript $\underline{i}$. We just said that we can write

$$\underline{w} = w_1 w_2 w_3. \qquad \text{III.E.1}$$

We shall call w_1 the topology weight. It gives the number of microbarns for each track of a given topology[+], and is calculated from the cross sections and numbers of events presented in table 5, i.e.

$$w_1 = \sigma/\text{no. of events}. \qquad \text{III.E.2}$$

It is necessary to use this procedure because we have measured different amounts of film for the different topologies.

We call w_2 the distribution weight. It depends on the particular distribution being plotted. For example, when we plot $d^2\sigma/dp_\perp dp_{||}(\text{lab})$, w_2 is given by

$$w_2 = 1/(\Delta p_\perp \Delta p_{||}(\text{lab})) \qquad \text{III.E.3}$$

[+]The elastic events are treated as a separate topology, for the reasons explained in section D.

where $\Delta p_\perp$ and $\Delta p_{||}$ are the bin widths of the weight histogram. Similiarly, if we want to plot ρ, we accumulate a weight histogram in $\Delta p_\perp \Delta p_{||}^*$, where w_2 is given by

$$w_2 = E^*/(2\pi p_\perp \Delta p_\perp \Delta p_{||}^*)$$

(see eqn. II.C.5)

We call w_3 the sampling weight. It depends on what fraction of the total number of tracks are used. If all the tracks are used once, it is simply set to one. If we take advantage of the symmetry of pp interactions in order to increase our statistics, by considering a given track frist in the target rest frame (laboratory) and then in the beam rest frame, as we do for the π^-, we set w_3 equal to $\frac{1}{2}$ each time we accumulate the track. If the subtraction method is used, w_3 may be set to -1 and $-\frac{1}{2}$ as well (see the next section).

G. Identification of Particles

1. Outline of the Problem

In this paper we report only on those events having no strange particle signature (no charged particle decays and no V's). There are therefore six possible particles of interest: the $\pi^{\pm}$, $K^{\pm}$, proton, and deuteron (Dalitz-pairs can be ignored, as is shown in appendix A.) Since the π^- is the only negative particle produced in appreciable quantities, all negative tracks are assumed to be π^-'s. Identification of the positive particles is not so simple.

2. Particle Identification Through the Application of Energy-Momentum Conservation to the Entire Event

In principle, those events having at most one neutral particle can be identified by the application of energy-momentum conservation. Furthermore, there are inequality conditions for events with two or more missing neutrals. In practice, however, the errors in the measured momentum often prevent the reliable determination of the final state by this method - except for those events with no unseen particles (see Appendix B). However, only a small fraction of the events have no unseen final state particles (table 6). To do an inclusive experiment, we must be able to identify a particle, no matter what other particles are produced along with it. Therefore, another, or at least an additional particle identification method, must be employed.

3. Particle Identification Through the Use of Measured Bubble-Density

It is well known that the bubble density of a track, relative to a minimum ionizing track, is given by

$$\text{RBD} = \frac{1}{\beta^2} = 1 + \frac{M^2}{p^2}, \qquad \text{III.F.1}$$

where β is the velocity of the particle that made the track and M and p are its mass and momentum. Of course, in practice, dipping or rising tracks are forshortened, and this increases the track density (TD) on the film.

For those events measured on the Spiral Reader, the darkness of each track (pulse height) is recorded. These pulse heights can be used to calculate a bubble-density χ^2 for the entire event. For a given kinematic hypothesis, TD is computed for each track, based on the momentum, angle, and supposed mass of that track. These TD's are compared with the TD's determined from the pulse height measurement, and a χ^2 is computed for the entire hypothesis . For those events measured on the Franckensteins and SMP's (about half the 4-prongs and all the 6-prongs), no pulse height information is recorded. However, all the 4-prongs were looked at by a person, who determined which of the various predicted track densities were correct (hypotheses with incorrect track densities were rejected). When these events were measured and processed (1967), the track densities determined from the Spiral Reader pulse-hights were somewhat less accurate than could be estimated by a person.

Unfortunately, the 6-prong data contains no track density information. However, for reasons that will be stated at the end of section 5, this is not thought to be too important.

Fig. 2 displays the allowed region in $p_\perp p_{||}$ space for outgoing π's and protons. The regions of bubble density < 2 and BD < 1.5 are marked off by very heavy lines. Almost all the π's having $p^*_{||} < 0$ are distinguishable, but protons with $p^*_{||} > -0.16$ GeV/c cannot be separated from the π^+ background on the basis of bubble density alone. [Fig. 2 also shows that tracks at very high lab momenta must be protons. For ease in programming, we do not make use of this fact, however. Using these events does not significantly increase the region of phase space that we can see.]

Fig 3 is a distorted version of figure 2, with a selection of events plotted on it. It so happens that we have only plotted the 2 and 3π final states from 4-prong reactions. We also tabulate the number of particles in the various regions of these scatter plots (table 7).

Because the proton distribution for 2-prongs is more sharply peaked backward and forward than for these 4-prongs, a larger fraction of the protons from 2-prong events should be identifiable from their bubble densities. Even so, the situation is not satisfactory, since we are quite interested in protons near $p^*_{||} = 0$.

4. Determination of the π^+ Spectrum

We have just shown that the use of measured bubble densities enables us to identify almost all the π^+ tracks in the backward hemisphere of the C. M. system. Because the target and beam are identical particles, we therefore know the π^+ distribution everywhere in the C.M. system, and, in fact, everywhere in all frames.

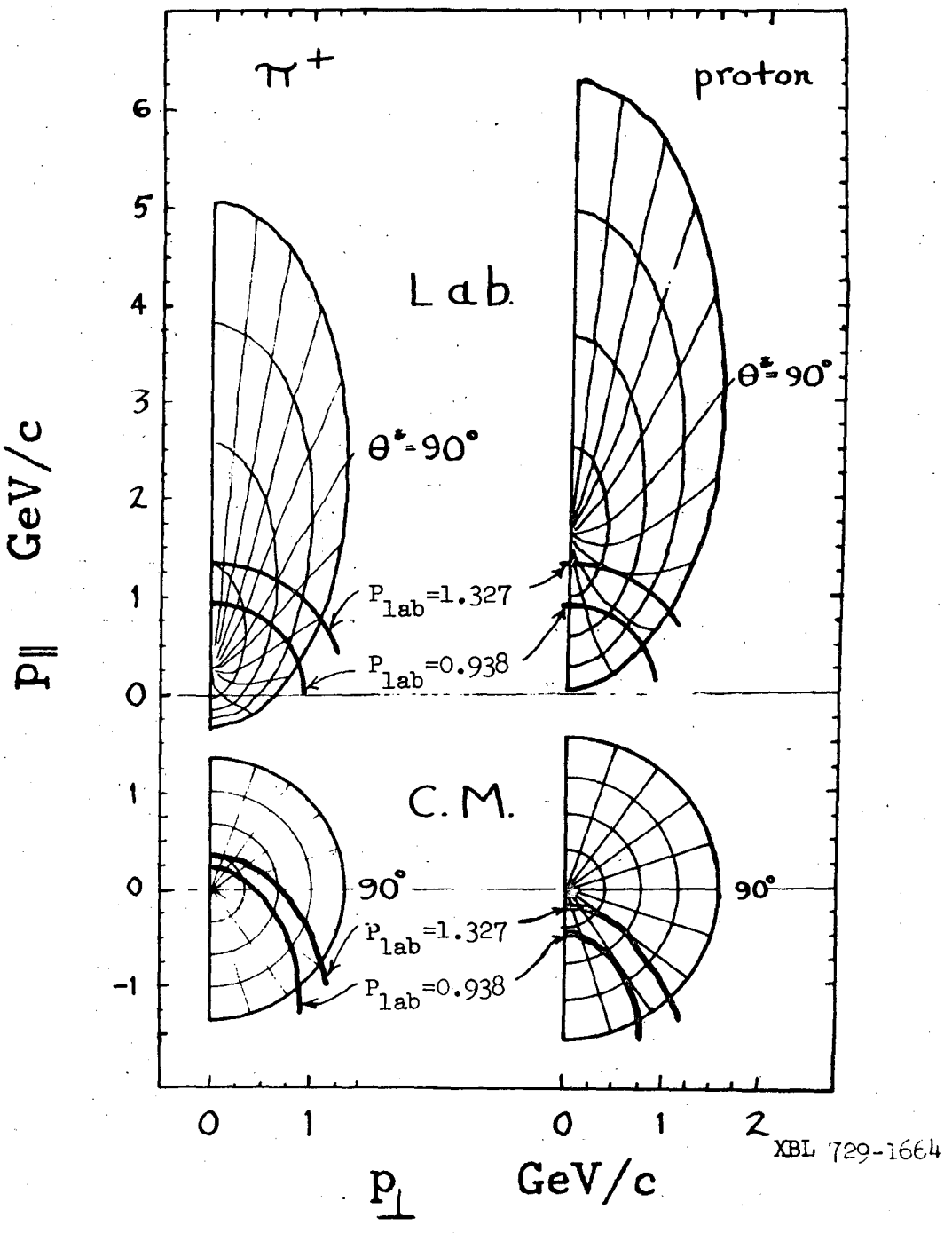

Fig. III.2 Allowed phase space, in both the lab. and C.M., for outgoing π's and protons from the reaction $pp \rightarrow pp\pi^+\pi^-$ at 6.6 GeV/c. Four curves of constant C.M. momentum are drawn on each graph. ($p^* = \frac{1}{4}p^*_{max}$, $\frac{1}{2}p^*_{max}$, $\frac{3}{4}p^*_{max}$, and p^*_{max}). There are also 11 curves of constant C.M. scattering angle ($\theta^* = 0°, 18°, 36°, \ldots, 180°$). Curves of $p_{lab} = 0.938$ and 1.327 GeV/c, which correspond to proton relative bubble densities (RBD) of 2 and 1.5, are also drawn on each graph. A proton with RBD $\geq$ 2 can easily be distinguished from a π, whereas a proton with RBD < 1.5 cannot.

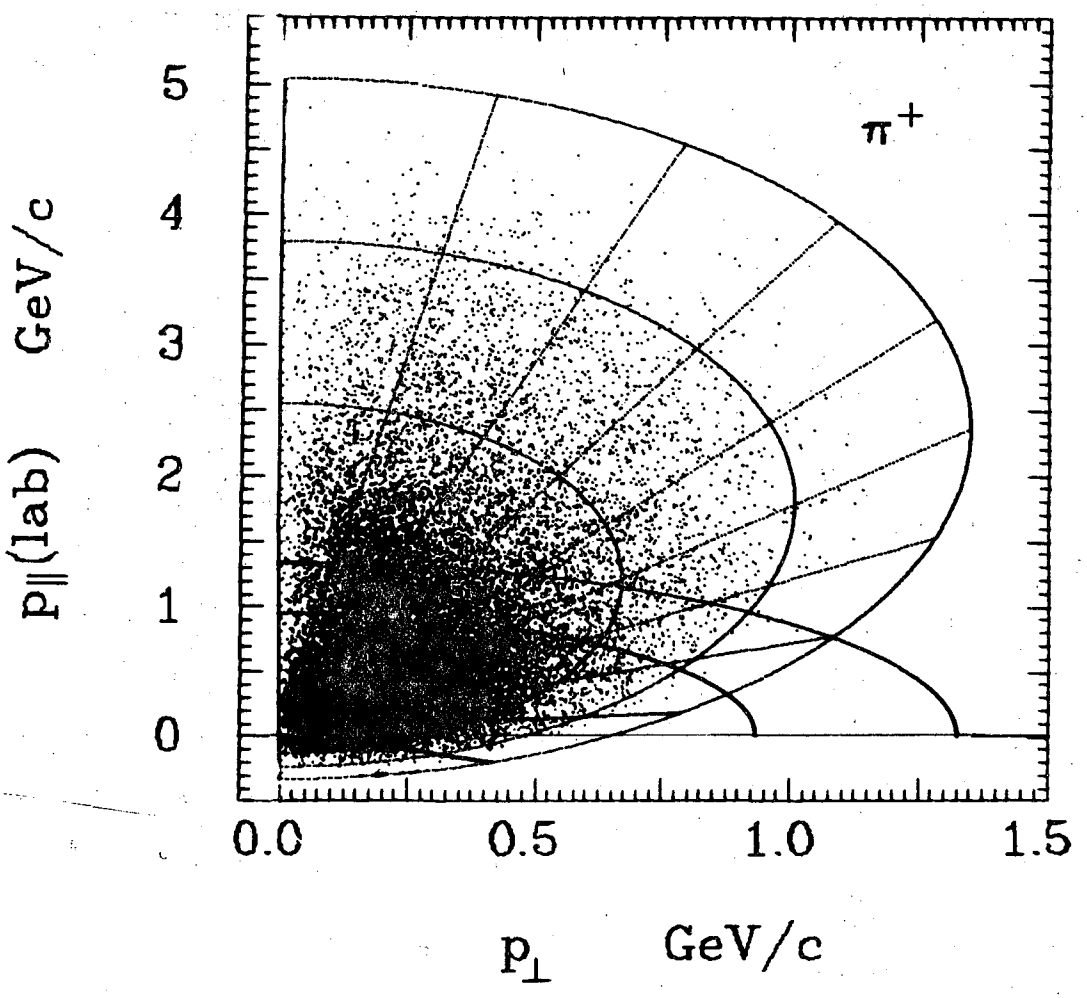

Fig. III.3 $p_\perp$ vs. $p_{\parallel}$ scatter plots (Peyrou plots) for π^+'s and protons from the reactions $pp \rightarrow pp\pi^+\pi^-$, $pp\pi^+\pi^-\pi^0$, and $pn\pi^+\pi^+\pi^-$ at 6.6 GeV/c. (See fig. 2 for an explanation of the various curves.) The different axes are not drawn to the same scale, in order that the data points may be more clearly seen.

a. π^+ in the laboratory system

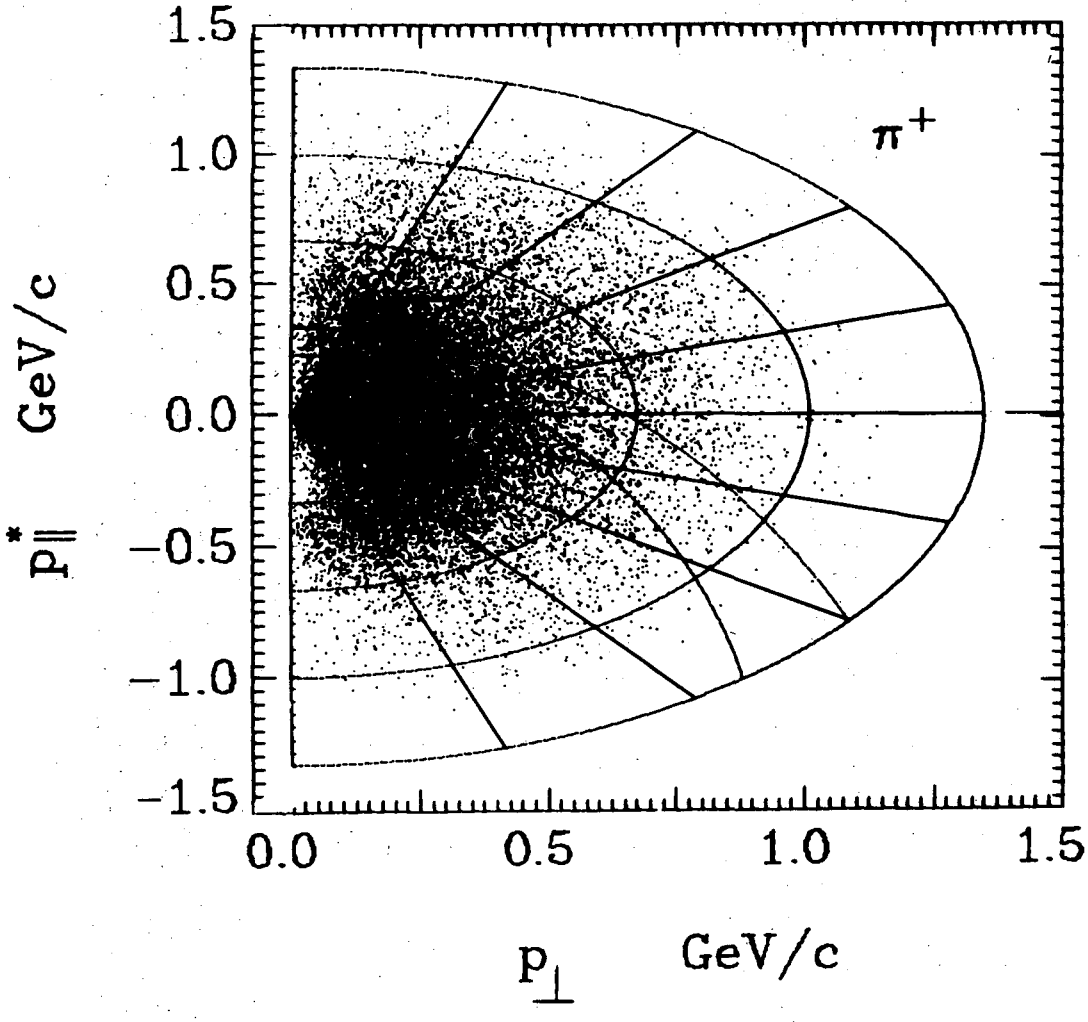

Fig. III.3 $p_\perp$ vs. $p_\parallel$ scatter plots ...
b. π^+ in the C.M. system

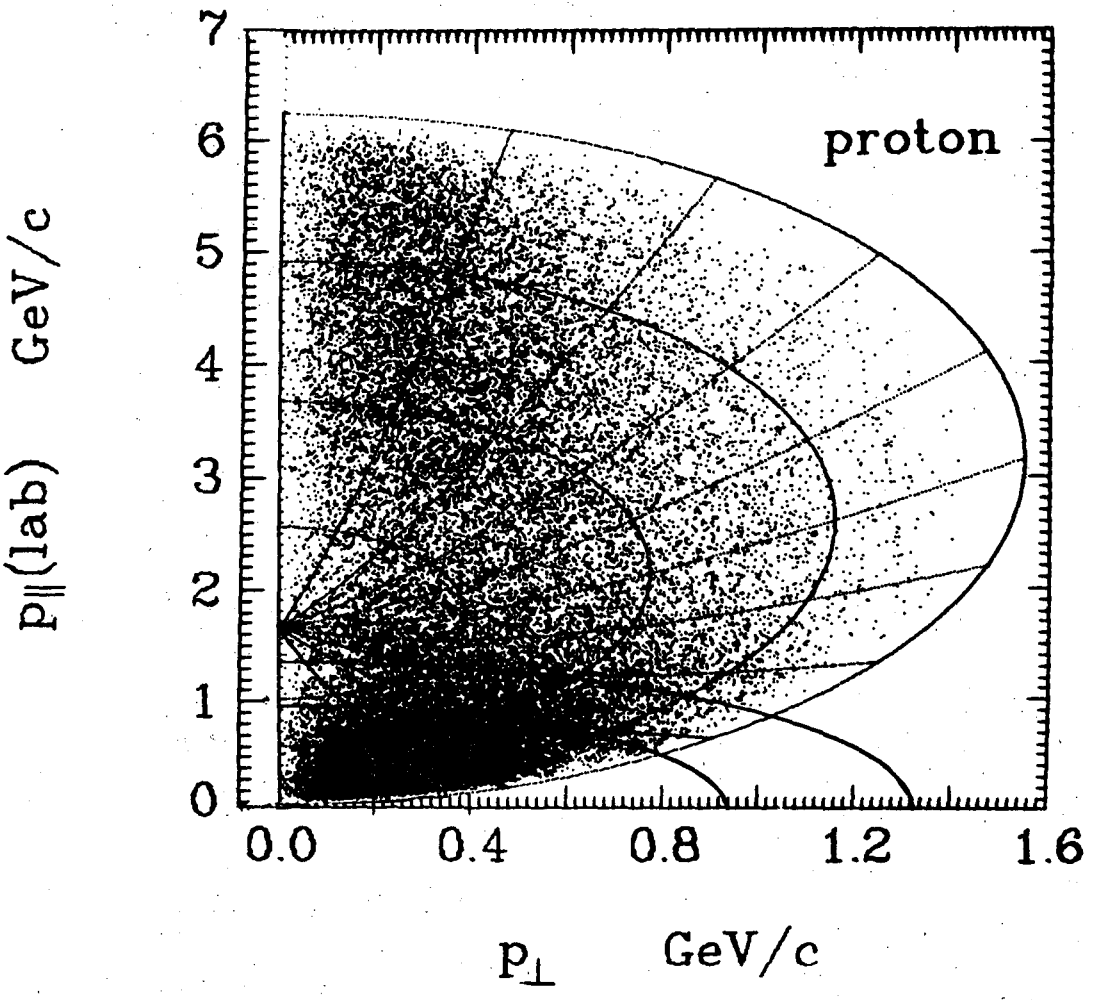

Fig. III.3 $p_{\perp}$ vs. $p_{\parallel}$ scatter plots ...

c. protons in the laboratory system

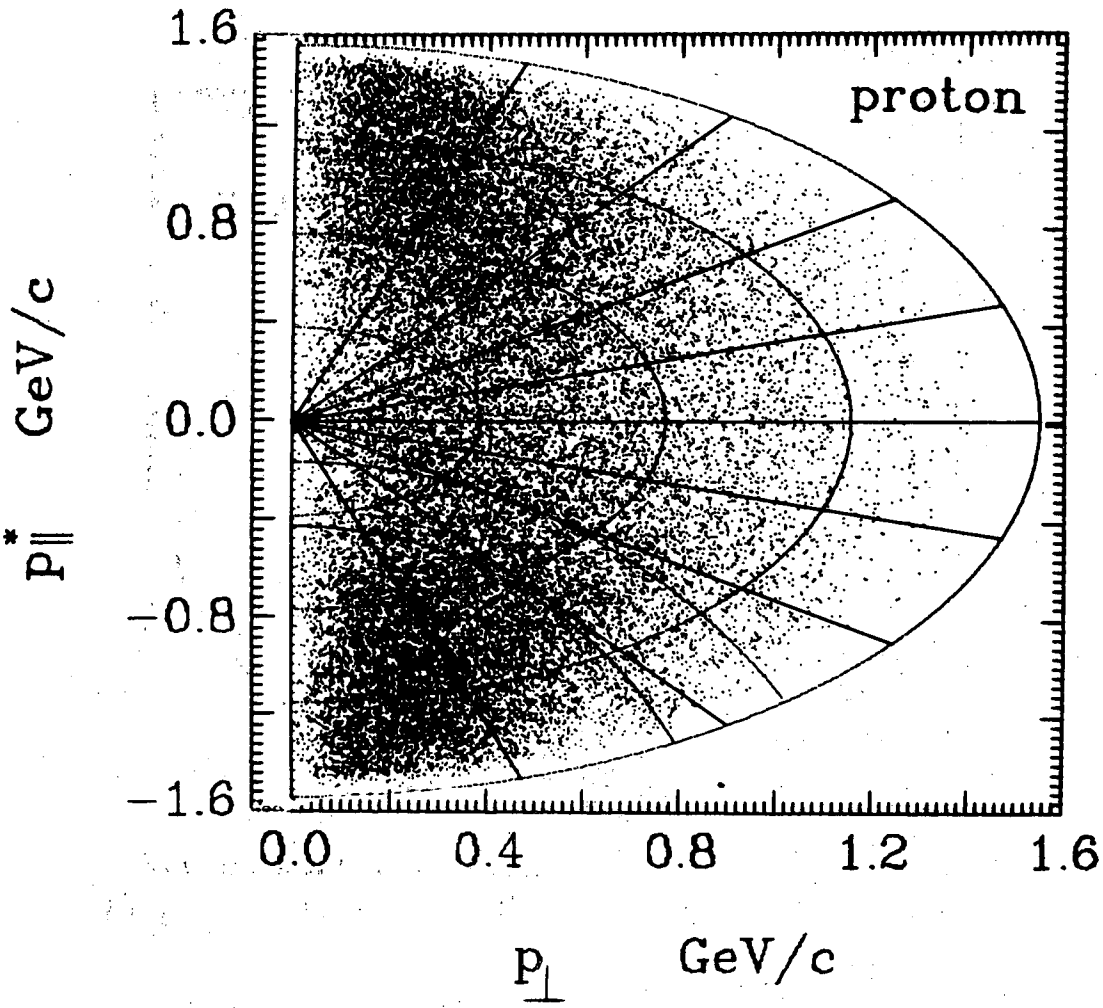

Fig. III.3 $p_\perp$ vs. $p_{\parallel}$ scatter plots ...

d. protons in the C.M. system

In actual fact, each backward π^+ is plotted twice. One time it is plotted with its true momentum, and the other time it is plotted reflected throught $p^*_{\parallel} = 0$ (because of the obvious symmetry, plots in the x variable are only plotted for positive x.) The sampling weight, w_3 is set to 1 (see section F) because, although each π^+ is plotted twice, only half of the π^+'s are plotted.

We have just shown that the π^+ distribution can be determined on the basis of bubble density alone. As a practical matter we make use of the kinematic fit information and the bubble density information for the entire event. This can only improve the situation, enabling us to identify some of the small number of backward π^+'s which cannot be identified on the basis of their measured bubble densities alone. Also, for the reasons detailed in Appendix B, we always accept the result of a 4-constraint fit.

5. Determination of the Proton Spectra - the Method of Subtracted Distributions

We have just seen that it is not possible to isolate all the proton tracks in the backward C.M. hemisphere by the use of bubble densities. However, for the purposes of this paper, we do not need to be able to identify each particle, but only to obtain particle distributions. If, as previously mentioned, we ignore the small amount of K^+ and deuteron production, there are only two types of positive tracks: the π^+ and proton. Now, we obviously know the positive particle distribution everywhere

(in the laboratory frame). However, we have just seen that we also know the π^+ distribution everywhere. We therefore can simply subtract the π^+ distribution from the total positive distribution, to obtain the proton distribution everywhere.

The actual procedure used in this paper also makes use of the fact that some protons can be identified and that 4-constraint fits are very reliable. We also restrict ourselves to the backward C.M. hemisphere for protons.

We now detail the exact procedure used in calculating our proton distributions. In the following discussion, tracks are considered most likely to be protons on the same basis that tracks are considered to be π^+'s in section 4.

(1) All tracks most likely to be protons are added if $p^*_{\parallel}$ (proton) < 0. The 4-vector is determined from p^{meas}_{lab} and the proton mass, where p^{meas}_{lab} is determined from the measured curvature and magnetic field. It depends only slightly on the particle mass, except for low momentum particles, for which particle identification is not a problem.

The sampling weight, w_3, is set to 1. Because of our previously mentioned confidence in 4-constraint fits, steps 2 and 3 are omitted for 4-constraint fits.

(2) If a track is considered most likely to be a π^+, and if (i) $p^*_{\parallel}(\pi^+) > 0$ and (ii) $p^{meas}_{lab} > 938$ MeV/c, than a "proton" 4-vector is formed from p^{meas}_{lab} and the proton mass. This 4-vector is transformed to the C.M. and called p^* (proton). If (iii) $p^*_{\parallel}$ (proton) < 0, we add this "proton" 4-vector to our distribution ($w_3 = 1$).

(3) If a track is considered most likely to be a π^+, and if (i) $p^*_{\parallel}(\pi^+) < 0$, we calculate $\vec{p'}_{lab}$ by first reflecting

the 4-vector $p^*(\pi^+)$ about $p^*_{\parallel} = 0$ [so that $p^*_{\parallel}(\pi^+)_{new} = -p^*_{\parallel}(\pi^+)_{old}$, while $p_{\perp,new} = p_{\perp,old}$], and then transforming this new pion 4-vector back into the laboratory. If (ii) $p'_{lab} > 938$ MeV/c, we form a "proton" 4-vector from $\vec{p}'_{lab}$ and the proton mass. This 4-vector is transformed into the C.M. system, and called p^* (proton). If (iii) $p^*_{\parallel}$(proton) $\lessgtr 0$, we <u>subtract</u> this proton 4-vector from our distribution ($w_3 = -1$).

(4) All the "proton" 4-vectors are now reflected through $p^*_{\parallel} = 0$, and plotted again with the same value of w_3.

Figure V.10a shows the differences in the proton distributions if one uses or does not use this subtraction procedure. They can be as much as 30 °/o for the 2-prongs.

Finally, we must note that because no bubble density measurements were performed on the 6-prong sample (for historical reasons), all the 6-prong π^+ and proton spectra have an unknown systematic error. However, the smallness of the 6-prong cross section should prevent this error from making a serious contribution to the error of the total spectra. Furthermore, there are very few missing mass events in the 6-prong sample, so the problem of particle identification is very much simplified. Also, the π^+ spectra do not seem all that different from the π^- spectra, and the trend of the data with increasing prong number is continued, so things should not be too far off.

The strategy that we just described is a modification of a procedure first developed by J. Anderson and D. Smith (Sm-4, An-4). Their method allows one to determine the π^+ and proton distributions, even if no bubble densities have been measured.

Table III.7 Number of particles in various regions of $p_{\parallel}$ $p_{\perp}$ space for some events fit to $pp \rightarrow pp\,\pi^+\pi^-$, $pp\pi^+\pi^-\pi^o$ and $pn\pi^+\pi^+\pi^-$ at 6.6 GeV/c.

$p^*_{\parallel}$	p(lab) (MeV/c)	Bubble Density for Protons	No. of Particles		Per Cent of Particles in each hemisphere	
			π^+	protons	π^+	protons
≥ 0	< 938	> 2 [a]	5123	0	38	0
	938 to 1327	1.5 to 2	2780	0	21	0
	> 1327	< 1.5	5428	15560	41	100
			13311 [b]	15560 [b]	100	100
< 0	< 938	> 2 [a]	11860	8922	95.0	55
	938 to 1327	1.5 to 2	448	3344	3.6	20
	> 1327	< 1.5	175	4052	1.4	25
			12483 [b]	16318 [b]	100	100

a. B. D. ≈ 1 for π^+'s with $p_{lab} \approx 938$ MeV/c.

b. assymetry parameter $A = \frac{n_F - n_B}{n_F + n_B} = 0.0321 \pm 0.0062$ for π^+ and 0.0237 ± 0.0056 for protons

where n_F = the no. of particles for which $p^*_{\parallel} \geq 0$ and

n_B = the no. of particles for which $p^*_{\parallel} < 0$

H. Particle Production Cross Sections

In inclusive reactions, we count each particle of a particular type, regardless of what other particles are produced along with it. It is therefore relevant to tabulate the cross sections with which different particles are produced.

Since essentially all the negative particles are π^-'s, the number of π^-'s per event depends only on the topology. Therefore, the π^- production cross-sections can be calculated trivially from the topological cross-sections presented in table 5 (i.e. A 4-prong gives one π^- and a 6-prong gives $2\pi^-$'s.). The total π^- production cross-section is 11.95 ± 0.50 mb.

Because both π^+'s and protons contribute to the positive particle cross section, a different procedure must be used. Consider a sample of events of some definite topology. By definition, the average number of particles of type x is simply the total number of particles of type x divided by the total number of events. We obtain the total number of π^+'s and protons by a procedure similar to that used for making plots. This procedure was described in the two preceeding sections.

Specifically, we obtain the total number of π^+'s by counting the number of π^+'s in the backward C. M. hemisphere and multipling by two. This takes advantage of the symmetry of the pp system, eliminating the problem of identifying fast particles. The total number of protons is obtained by using the subtraction method described in the preceeding section. The average numbers of π^+'s and protons, together with the production cross-sections obtained form them, are listed in tables 8 and 9.

Table III. 8 π^+ production cross sections according to the number of charged particles in the final state (prongs) for $pp \rightarrow \pi^+ +$ anything at 6.6 GeV/c

	Interaction Cross Section (mb) [a]	X	Avg. No. of outgoing π^+'s	=	Production Cross Section (mb) [a]
2-prongs (inel.)	16.83 ± 0.70		0.883 ± 0.028 [d]		14.86 ± 0.78 [c]
2-prongs	10.50 ± 0.46		1.460 ± 0.011 [d]		15.33 ± 0.68 [c]
6-prongs	0.727 ± 0.094		2.28 ± 0.04 [d]		1.66 ± 0.22 [c]
total inelastic [e]	28.06 ± 0.84		1.135 ± 0.020 [c]		31.9 ± 1.1 [f]
elastic	11.79 ± 0.22		0		0
total	39.8 ± 1.0		0.833 ± 0.019 [c]		31.9 ± 1.1 [f]

a. from table 5

b. the average is reduced and the error is increased to account for the fact that the uncorrected values give $\langle n_{\pi^+} \rangle + \langle n_{proton} \rangle = 2.05$ for 2 prongs, whereas 2 is the maximum allowed.

c. combined statistical error and error in interaction cross section (s)

d. statistical error only

e. strange particle events and events with more than 6 prongs are not included (see table 5 for their interaction cross sections)

f. calculated from the individual production cross sections listed above.

Table III. 9 Proton production cross sections according to the number of charged particles in the final state (prongs) for $pp \rightarrow p + anything$ at 6.6 GeV/c

	Interaction Cross Section (mb) [a]	×	Avg. No. of outgoing protons	=	Production Cross Section (mb) [a]
2-prongs (inel.)	16.83 ± 0.70		1.116 ± 0.030 [b]		18.78 ± 0.93 [c]
4-prongs	10.50 ± 0.46		1.535 ± 0.014 [d]		16.12 ± 0.72 [c]
6-prongs	0.727 ± 0.94		1.70 ± 0.04 [d]		1.23 ± 0.16 [c]
total inelastic [e]	28.06 ± 0.84		1.288 ± 0.020 [c]		36.1 ± 1.2 [f]
elastic	11.79 ± 0.22		2		23.58 ± .44
total [e]	39.8 ± 1.1		1.499 ± 0.017 [c]		59.7 ± 1.3 [f]

a to f. see footnotes on previous table

IV. RESULTS: π^- SPECTRA

A. Comparison with Higher Energies in the Laboratory System

Dennis Smith showed that for proton-proton collisions from 13 to 28.5 GeV/c the data are consistent with the hypothesis of limiting fragmentation in the target region, that is $d^2\sigma/dp_\perp dp_{||}$(lab) is independent of the overall energy of the reaction (Sm-1). He therefore only tabulates $d^2\sigma/dp_\perp dp_{||}$ averaged over all his energies rather than for each energy separately. We compare our 6.6 GeV/c data with his (fig. 1 and table 1). For seven equal intervals in $p_\perp$, from 0.0 to 0.7 GeV/c, we plot $d^2\sigma/dp_\perp dp_{||}$ for π^- versus $p_{||}$(lab) for both experiments.†,‡ Various vertical lines are drawn on fig. 1 in order to show the relation between the C. M. and lab. systems for each $p_\perp$ interval. The rightmost pair of broken lines on each plot are the minimum and maximum values of $p_{||}$(lab) for $\underline{x} = 0$ for D. Smith's data, and the rightmost pair of solid lines are the same thing for our 6.6 GeV/c data. Going left, the next set of lines correspond to the minimum and maximum values of $p_{||}$(lab) for $\underline{x}_3 = -0.5$. Clearly $p_{||}$(lab) changes slowly with $\underline{s}$, for constant $\underline{x}_3$, in this region of $\underline{x}_3$. Finally, the two leftmost pairs of lines indicate the minimum value of $p_{||}$(lab) possible over the range of $p_\perp$ and $\underline{s}$ in question.

---

† However, before making this plot, we must first divide the values given by D. Smith (in Table VII of ref. Sm-1) by 2. This is necessary because he has actually tabulated $d^2\sigma/dp_\perp dp_{||}$(beam rest frame) + $d^2\sigma/dp_\perp dp_{||}$(lab) in order to improve his statistics, just as we do, but he has not divided the sum by two, as we do (Sm-2).

‡ We plot $d^2\sigma/dp_\perp dp_{||}$ rather than ρ (defined by equation II.C.1) only because D. Smith chose to do this. As we demonstrated in section II.C, $d^2\sigma/dp_\perp dp_{||}$(lab) can be independent of the incident particle energy if and only if $\rho(p_\perp, p_{||}, s) = \rho(p_\perp, p_{||})$.

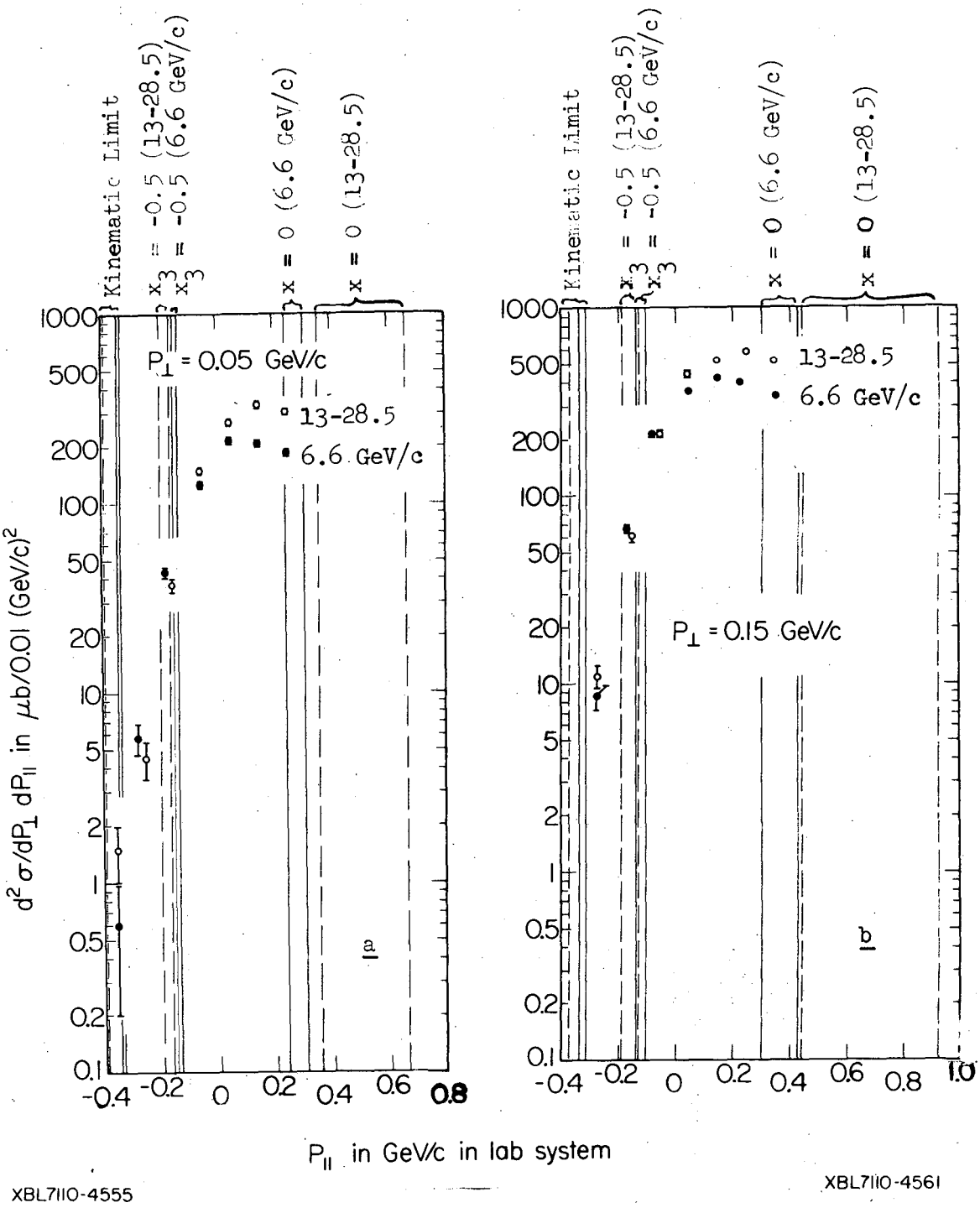

Fig. IV.1 $d^2\sigma/dp_\perp dp_\parallel$ vs. $p_\parallel$(lab) of the π^- for 7 different intervals in $p_\perp$ from 0 to 0.7 GeV/c for $pp \rightarrow \pi^-$ + anything. The open circles (o) are D. Smith's data from 13 to 28.5 GeV/c (ref. Sm-1) and the solid circles (•) are from this experiment at 6.6 GeV/c. The 3 pairs of solid lines delimit (1) the lower kinematic limit of $p_\parallel$(lab), and (2) and (3), the regions where it is possible to have x_3 = -0.5 and x_3 = 0, respectively, for the 6.6 GeV/c data. The broken lines delimit the same regions for the 13 to 28.5 GeV/c data. (Some of these lines lie beyond the plot boundries, and are therefore not shown.) drawn.)

a. $p_\perp$ = 0.05 GeV/c b. $p_\perp$ = 0.15 GeV/c

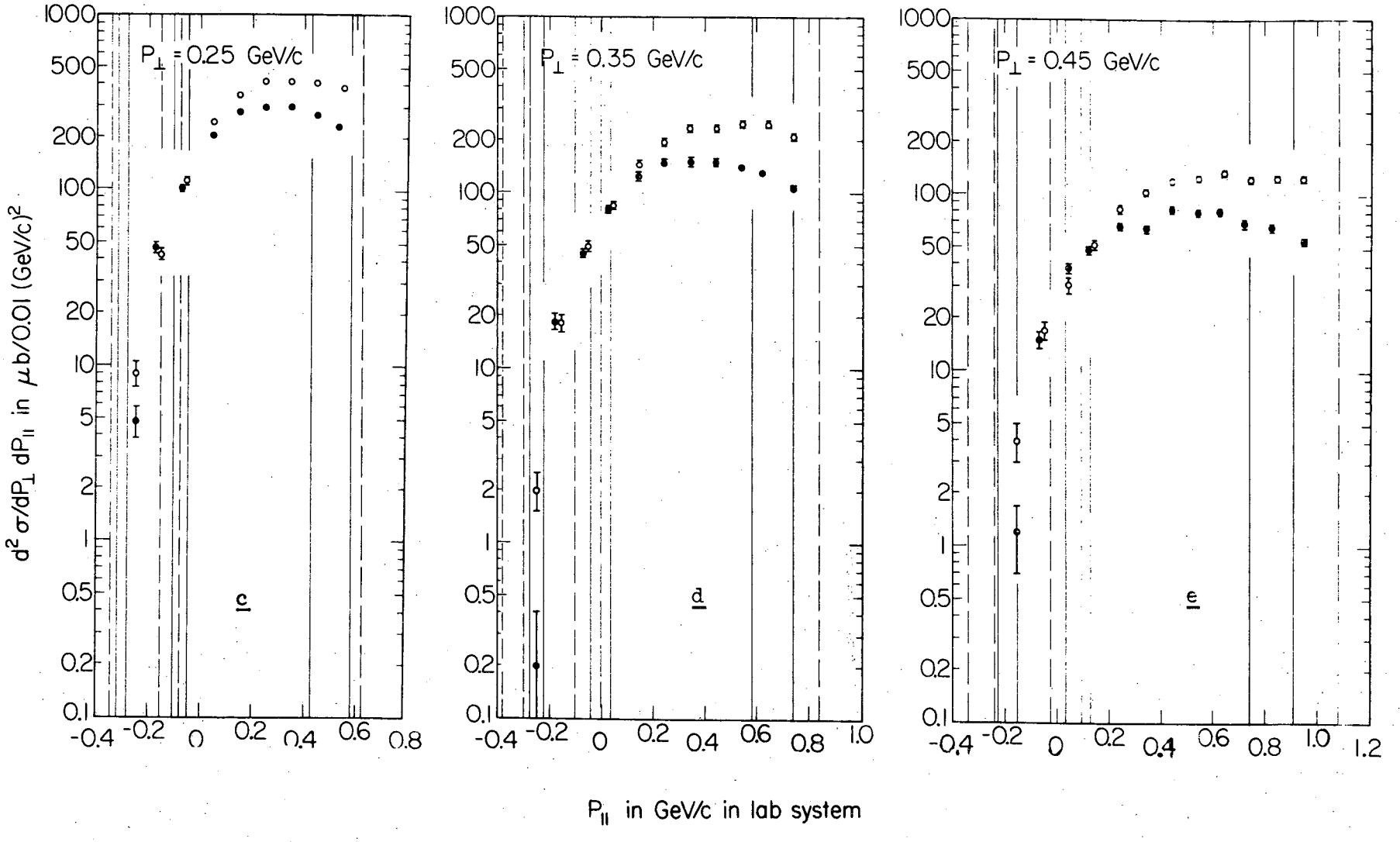

XBL7110-4560

XBL7110-4559

XBL7110-4558

Fig. IV.1 (continued)

c. $p_\perp$ = 0.25 GeV/c

d. $p_\perp$ = 0.35 GeV/c

e. $p_\perp$ = 0.45 GeV/c

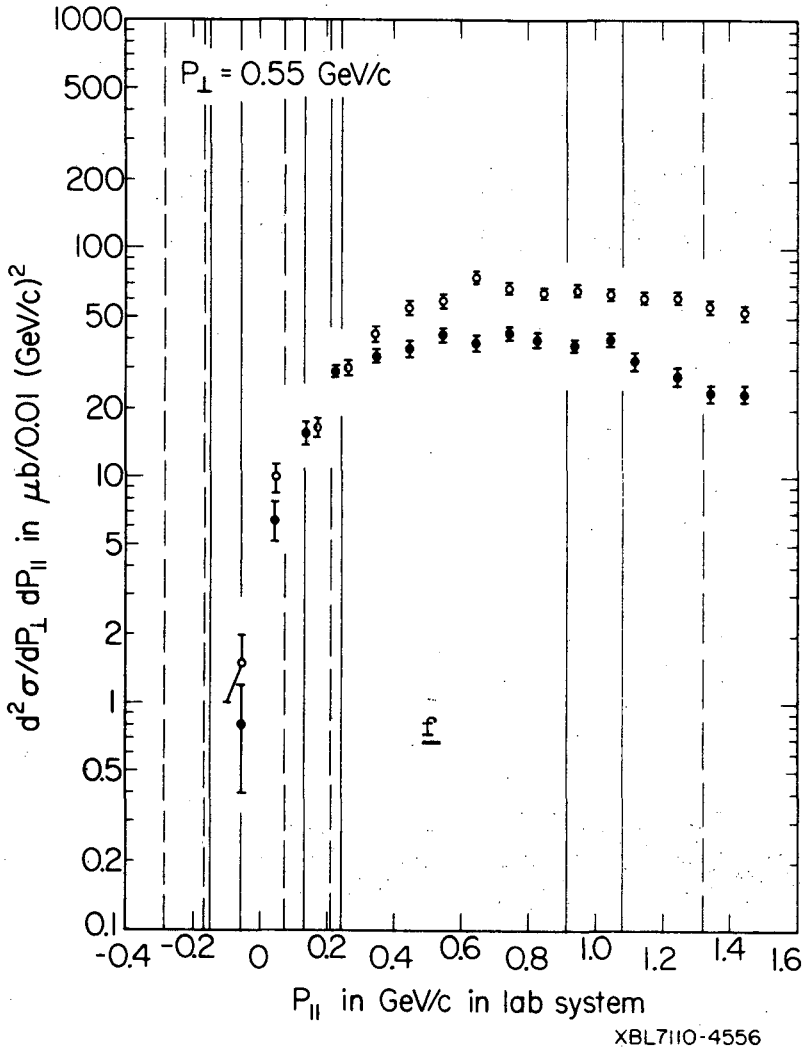

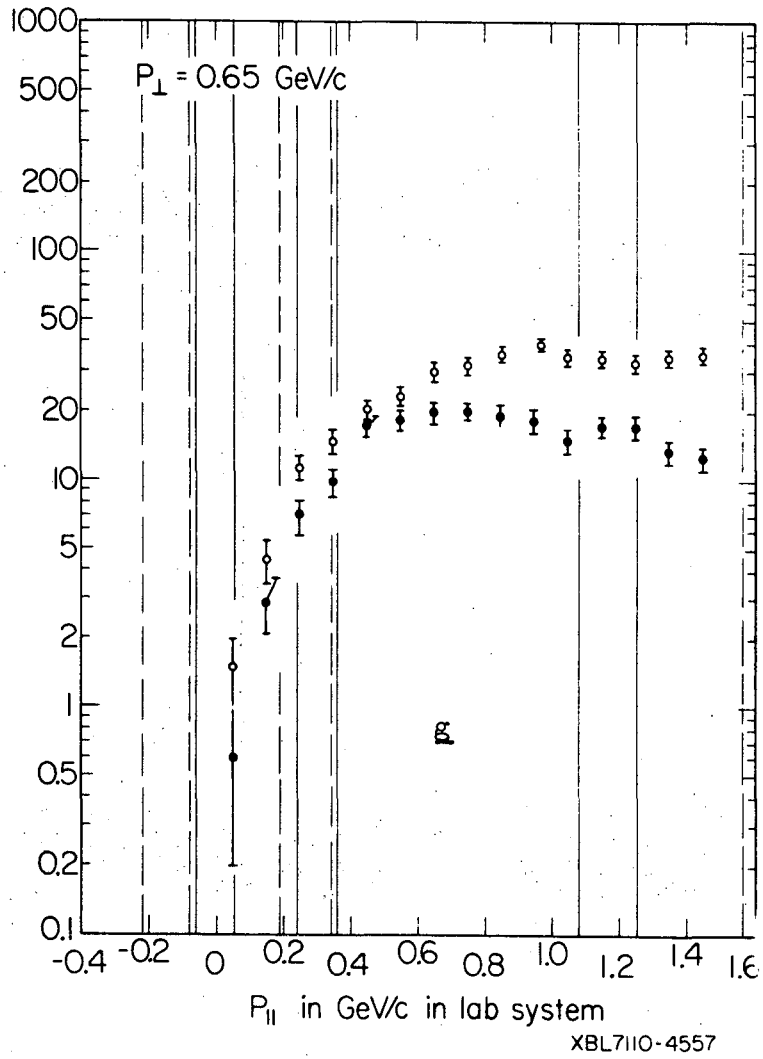

Fig. IV.1 (continued)

f. $p_\perp$ = 0.55 GeV/c

g. $p_\perp$ = 0.65 GeV/c

Table IV.1. A comparison of this experiment (6.6 GeV/c) with D. Smith (13 to 28.5 GeV/c - ref. Sm-1) for the reaction $pp \rightarrow \pi^- +$ anything: $d^2\sigma/dp_\perp dp_{||}$ vs. $p_{||}$(lab) for 7 intervals in $p_\perp$. [tabulation of the data in fig. 1]

			$d^2\sigma/dp_\perp dp_{||}$ μb/0.01(GeV/c)^2		Cross Section
$p_\perp$ (GeV/c)	$p_\perp^2$ (GeV/c)^2	$p_{||}$(lab) (GeV/c)	P_{beam}=13 to 28.5 GeV/c	P_{beam}=6.6 GeV/c	Ratio Smith/this expt.
0.05	0.0025	-0.35	1.5 ± 0.5	0.60 ± 0.4	2.5 ± 1.9
		-0.25	4.5 ± 1.0	5.80 ± 1.1	0.78 ± 0.23
		-0.15	37.0 ± 3.0	43.0 ± 3.0	0.86 ± 0.09
		-0.05	147.0 ± 6.0	125.2 ± 5.0	1.18 ± 0.07
		0.05	267.0 ± 8.5	215.2 ± 6.5	1.24 ± 0.05
		0.15	330.0 ± 10.0	203.9 ± 6.3	1.62 ± 0.07
		0.25	298.0 ± 9.0	184.9 ± 6.0	1.61 ± 0.07
0.15	0.0225	-0.25	11.0 ± 1.5	8.50 ± 1.3	1.29 ± 0.27
		-0.15	60.5 ± 4.0	67.0 ± 3.7	0.90 ± 0.08
		-0.05	211.5 ± 7.5	213.6 ± 6.6	0.99 ± 0.05
		0.05	444.5 ± 11.5	362.4 ± 8.5	1.23 ± 0.04
		0.15	552.5 ± 13.0	413.7 ± 9.0	1.34 ± 0.04
		0.25	578.0 ± 13.5	397.8 ± 8.8	1.45 ± 0.05
		0.35	526.0 ± 13.0	337.7 ± 8.1	1.56 ± 0.05
0.25	0.0625	-0.25	9.0 ± 1.5	4.80 ± 1.0	1.87 ± 0.50
		-0.15	42.5 ± 3.0	46.5 ± 3.1	0.91 ± 0.09
		-0.05	113.0 ± 5.5	100.6 ± 4.5	1.12 ± 0.07
		0.05	239.0 ± 8.0	203.2 ± 6.4	1.18 ± 0.05
		0.15	344.0 ± 10.0	274.7 ± 7.4	1.25 ± 0.05
		0.25	407.0 ± 11.0	293.3 ± 7.6	1.39 ± 0.05
		0.35	408.0 ± 11.0	294.5 ± 7.6	1.39 ± 0.05
		0.45	405.0 ± 11.0	264.4 ± 7.2	1.53 ± 0.06
		0.55	377.5 ± 10.5	231.9 ± 6.7	1.63 ± 0.07

Table IV.1 (continued

p (GeV/c)	$p_\perp^2$ $(GeV/c)^2$	$P_{\parallel}$(lab) (GeV/c)	$d^2\sigma/dp_\perp dp_{\parallel}$ μb/0.01(GeV/c)^2 P_{beam}= 13 to 28.5 GeV/c	$d^2\sigma/dp_\perp dp_{\parallel}$ μb/0.01(GeV/c)^2 P_{beam}=6.6 GeV/c	Cross Section Ratio Smith/this expt
0.35	0.1225	-0.25	2.0 ± 0.5	0.2 ± 0.2	10.0 ± 10.3
		-0.15	18.0 ± 2.0	18.3 ± 1.9	0.98 ± 0.15
		-0.05	49.0 ± 3.5	44.8 ± 3.0	1.09 ± 0.11
		-0.05	83.5 ± 4.5	80.4 ± 4.0	1.04 ± 0.08
		0.15	143.5 ± 6.0	122.6 ± 5.0	1.17 ± 0.07
		0.25	193.0 ± 7.0	148.6 ± 5.4	1.30 ± 0.07
		0.35	234.0 ± 8.0	150.9 ± 5.5	1.55 ± 0.08
		0.45	236.5 ± 8.0	151.2 ± 5.5	1.56 ± 0.08
		0.55	248.0 ± 8.5	140.1 ± 5.3	1.77 ± 0.09
		0.65	244.5 ± 8.0	130.9 ± 5.1	1.87 ± 0.10
		0.75	209.0 ± 7.5	105.8 ± 4.6	1.98 ± 0.11
0.45	0.2025	-0.15	4.00± 1.00	1.20± 0.50	3.33 ± 1.62
		-0.05	17.0 ± 2.00	15.0 ± 1.80	1.13 ± 0.19
		0.05	30.5 ± 3.00	38.2 ± 2.80	0.80 ± 0.10
		0.15	51.5 ± 3.50	48.5 ± 3.20	1.06 ± 0.10
		0.25	83.0 ± 4.50	66.2 ± 3.70	1.25 ± 0.10
		0.35	103.0 ± 5.00	63.4 ± 3.60	1.62 ± 0.12
		0.45	120.0 ± 5.50	83.2 ± 4.10	1.44 ± 0.10
		0.55	123.5 ± 5.50	79.7 ± 4.00	1.55 ± 0.10
		0.65	135.5 ± 6.00	81.1 ± 4.00	1.67 ± 0.11
		0.75	123.5 ± 5.50	68.7 ± 3.70	1.80 ± 0.13
		0.85	124.0 ± 5.50	65.9 ± 3.60	1.88 ± 0.13
		0.95	126.5 ± 6.00	55.1 ± 3.30	2.30 ± 0.18
0.55	0.3025	-0.05	1.50± 0.50	0.80± 0.40	1.87 ± 1.13
		0.05	10.0 ± 1.50	6.40± 1.20	1.56 ± 0.38
		0.15	16.5 ± 2.00	15.8 ± 1.80	1.04 ± 0.17
		0.25	30.0 ± 3.00	29.3 ± 2.50	1.02 ± 0.13
		0.35	42.5 ± 3.00	33.8 ± 2.60	1.26 ± 0.13
		0.45	55.0 ± 4.0	36.6 ± 2.7	1.50 ± 0.16
		0.55	59.0 ± 4.00	42.4 ± 2.90	1.39 ± 0.13
		0.65	75.5 ± 4.50	39.6 ± 2.80	1.91 ± 0.18
		0.75	67.0 ± 4.00	42.8 ± 2.90	1.57 ± 0.14
		0.85	64.5 ± 4.00	39.7 ± 2.80	1.62 ± 0.15

Table IV.1 (continued)

$p_\perp$ (GeV/c)	$p_\perp^2$ $(GeV/c)^2$	$p_{\parallel}$ (GeV/c)	$d^2\sigma/dp_\perp dp_{\parallel}$ μb/0.01(GeV/c)^2 P_{beam}=13 to 28.5 GeV/c	P_{beam}=6.6 GeV/c	Cross Section Ratio Smith/this expt.
		0.95	65.5 ± 4.00	38.0 ± 2.80	1.72 ± 0.16
		0.05	63.5 ± 4.00	40.5 ± 2.80	1.57 ± 0.15
		1.15	61.5 ± 4.00	32.3 ± 2.50	1.90 ± 0.19
		1.25	61.0 ± 4.00	27.7 ± 2.40	2.20 ± 0.24
		1.35	56.5 ± 4.00	23.7 ± 2.20	2.38 ± 0.28
		1.45	52.5 ± 4.00	23.2 ± 2.20	2.26 ± 0.28
0.065	0.4225	0.05	1.50± 0.50	0.60± 0.40	2.50 ± 1.86
		0.15	4.50± 1.00	2.90± 0.80	1.55 ± 0.55
		0.25	11.5 ± 1.50	7.10± 1.20	1.62 ± 0.35
		0.35	15.0 ± 2.00	9.80± 1.40	1.53 ± 0.30
		0.45	20.5 ± 2.00	17.5 ± 1.90	1.17 ± 0.17
		0.55	23.5 ± 2.50	18.4 ± 1.90	1.28 ± 0.19
		0.65	30.0 ± 3.00	20.1 ± 2.00	1.49 ± 0.21
		0.75	32.0 ± 3.00	20.6 ± 2.00	1.55 ± 0.21
		0.85	36.0 ± 3.00	19.3 ± 2.00	1.87 ± 0.25
		0.95	39.5 ± 3.00	18.5 ± 1.90	2.14 ± 0.27
		1.05	35.0 ± 3.00	15.2 ± 1.80	2.30 ± 0.34
		1.15	34.5 ± 3.00	17.5 ± 1.90	1.97 ± 0.27
		1.25	33.0 ± 3.00	17.4 ± 1.90	1.90 ± 0.27
		1.35	35.0 ± 3.00	13.8 ± 1.70	2.54 ± 0.38
		1.45	35.5 ± 3.00	12.8 ± 1.60	2.77 ± 0.42

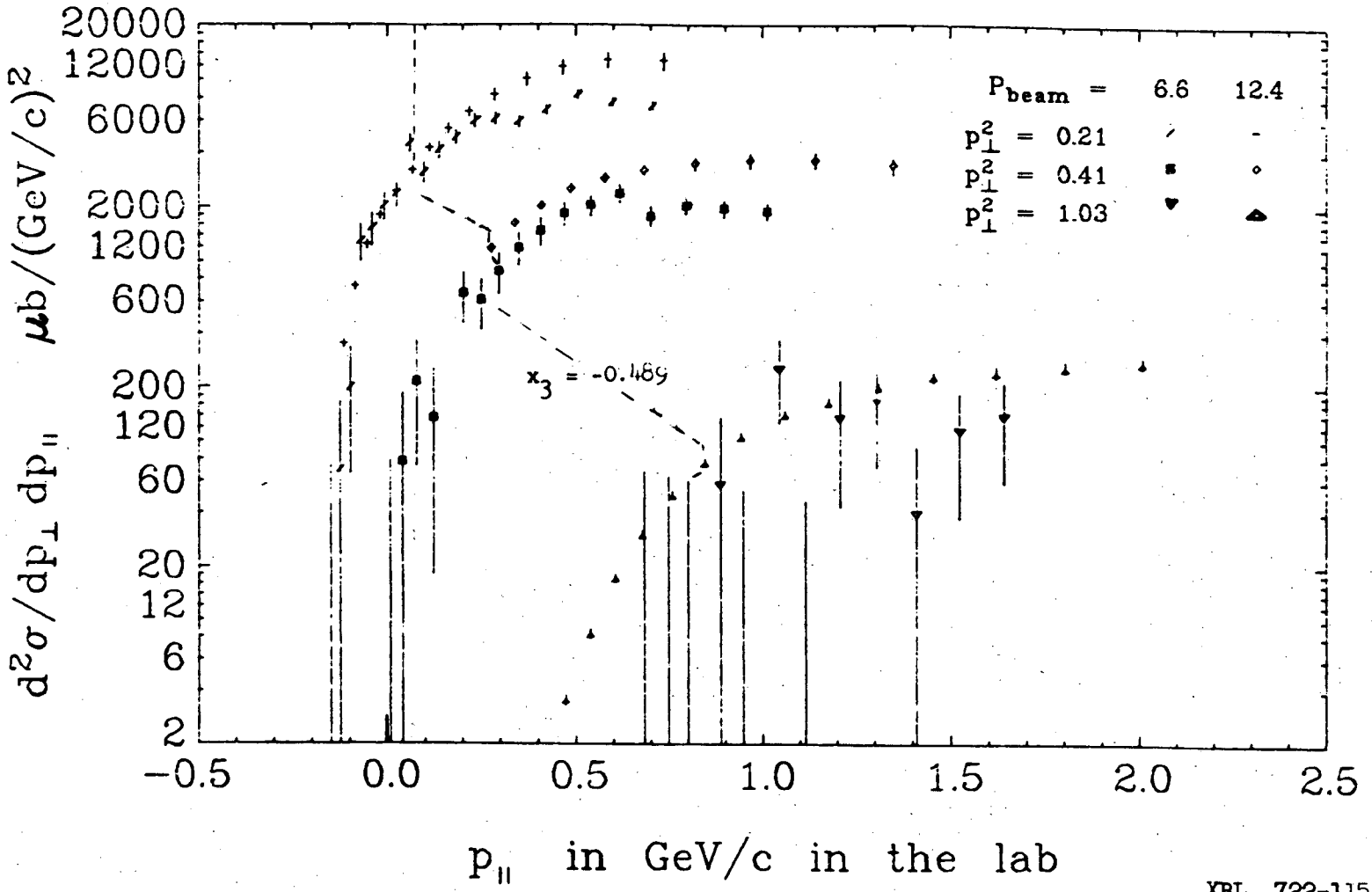

Fig. IV.2 $d^2\sigma/dp_\perp dp_\parallel$ vs. $p_\parallel$(lab) for $p_\perp^2$ = 0.21, 0.41, and 1.03 (GeV/c) for $pp \rightarrow \pi^-$ + anything. A comparison of this experiment (6.6 GeV/c) with Akerlof et al. (12.4 GeV/c - ref. Ak-1). A broken line joins points having x_3 = 0.489. This graph is obtained by transforming the points of fig. 3. Please note: The data point is at the apex of the triangle symbols, viz. ▲ and ▼. It is at the center of all other symbols, viz. ■, ◆, etc.

We observe that for $x_3 \lesssim -0.4$, our data is in good agreement with D. Smith's, except for our highest $p_\perp$ interval (for which $p_\perp = \frac{1}{2}p_{\perp,max}$; $p_{\perp,max} = 1.35$ GeV/c). However, our data falls below Smith's for $x_3 \gtrsim -0.4$. There is also some disagreement at the very lowest $p_{||}$, where the differential cross section for our energy is always less than for higher energy.†

A similar comparison is made with the 12.4 GeV/c counter data of Akerlof et al. (Ak-1) in fig. 2. The upper two curves ($p_\perp^2 = 0.21$ (GeV/c)^2, corresponding to fig. 1e) show agreement at small values of $p_{||}$(lab), while the next two curves ($p_\perp^2 = 0.41$(GeV/c)^2, corresponding to fig. 1g) do not quite agree, even for small $p_{||}$; the 6.6 curve is always below the 12.4 curve. The comparison with Akerlof et al. and the comparison with D. Smith are therefore in agreement.

We notice that Akerlof et al.'s points are not uniformly spaced in $p_{||}$(lab). Therefore, in order to make a bin-by-bin comparison with their points in the lab, as we did for D. Smith's points, we would have to accumulate a histogram for our 6.6 data with a non-uniform bin width. This is rather awkward. This is the only reason that we do not present a tabular form of fig. 2.

---

† We do note, however, that the π^- can have more backward momentum for higher energy reactions. Also, we have not corrected for the fact that our most backward bin in $p_{||}$ is partly below the kinematic limit, while that for the higher energy experiment is not.

B. Comparison with Higher Energy in the Central Region

Next, we investigate the properties of the central region, i.e. the region of small $|x|$. Because the value of $p_{||}(\text{lab})$ for $x = 0$ depends strongly on s, the lab. system is not appropriate for the study of this region, and we therefore compare data in the C.M. system, chosing Feynman's-x and $p_\perp$ as our variable (Fe-1). Because the data tabulated by D. Smith is averaged over a variety of energies, it is not possible, strictly speaking, to transform it to the C.M. system, and we therefore confine our attention to the 12.4 GeV/c counter data.

Fig. 3 displays ρ vs x_3 for three different values of $p_\perp$, for both our data and Akerlof et al.'s. (also see table IV.2.) . We bin our 6.6 GeV/c data so that the center of each of our bins is equal in both x_3 and $p_\perp^2$ to one of Akerlof's points. (The effect of our having to take a larger bin in $p_\perp$ than does Akerlof is not crucial.) Clearly, there is no agreement for $x \approx 0$ where $\rho(12.4) \approx 2\rho(6.6)$. We also note that the ratio $\rho(12.4)/\rho(6.6)$ increases with increasing $p_\perp^2$.

Because the one particle distribution for points should be fairly smooth, the single high 6.6 GeV/c data point at $x_3 = 0.54$ and $p_\perp^2 = 0.21$ $(\text{Gev/c})^2$ is believed to be a statistical fluctuation.

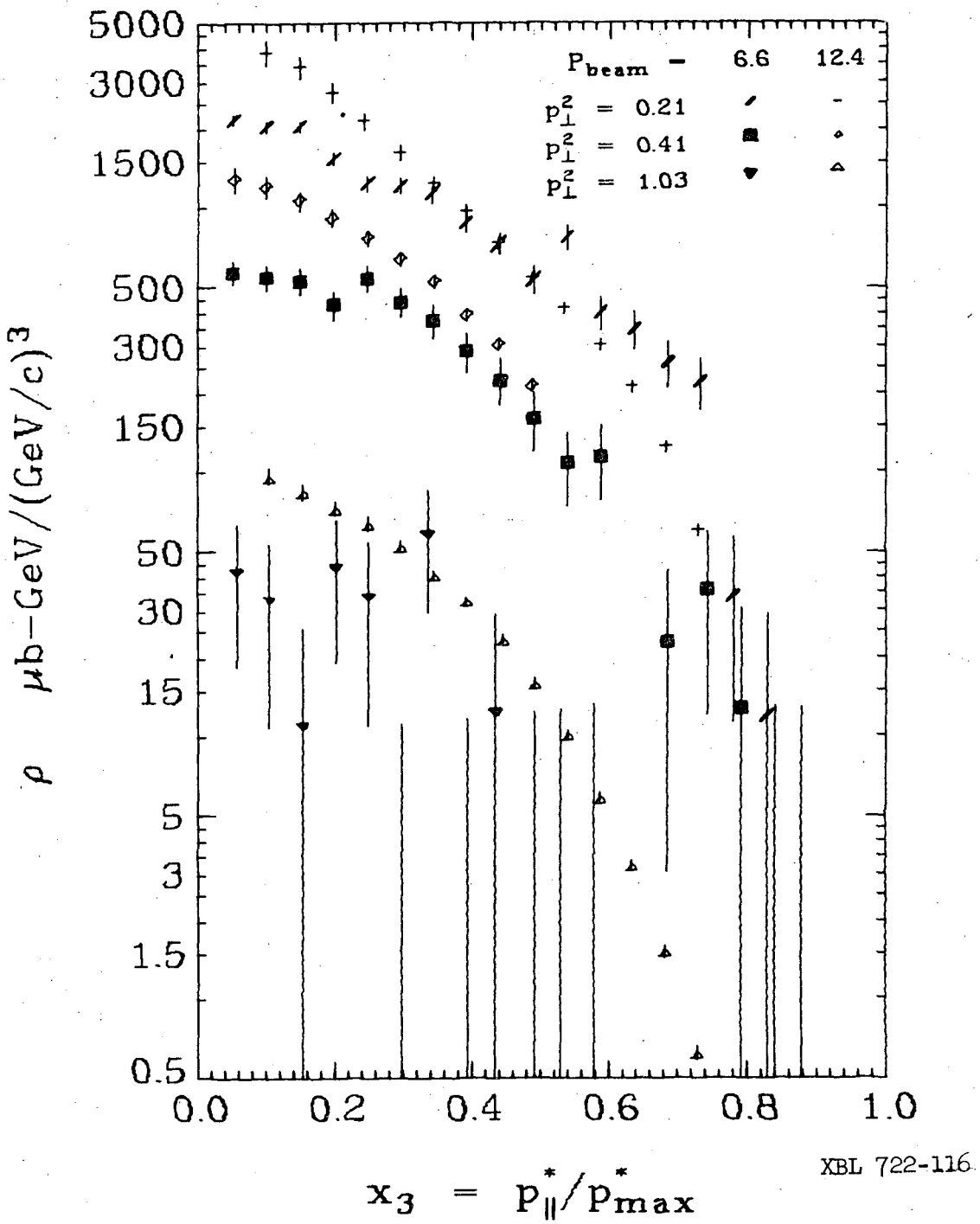

Fig. IV.3 ρ vs. x_3 for $p_\perp^2$ = 0.21, 0.41, and 1.03 (GeV/c)^2 for $pp \to \pi^-$ + anything. A comparison of this experiment (6.6 GeV/c) and Akerlof et al. (12.4 GeV/c - ref. Ak-1). Our points are averaged over bins centered on Akerlof's points, with bin widths Δx = Akerlof's spacing in x_3, and $\Delta p_\perp^2$ = 0.1 (GeV/c)^2. Please note: The data point is at the apex of the triangle symbols, viz. △ and ▽.

Table IV.2. A comparison of this experiment (6.6 GeV/c) with Akerlof et al. (12.4 GeV/c - ref. Ak-1 for the reaction $pp \to \pi^- +$ anything: ρ vs. x_3 for three values of $p_\perp^2$. [tabulation of the data in fig. 3]

		$\rho = Ed^3\sigma/dp^3$ ($\mu b\text{-}c^3/GeV^2$)		Ratio
$p_\perp^2$	x_3	$P_{beam} = 12.4$	$P_{beam} = 6.6$	$\rho_{12.4} / \rho_{6.6}$
0.21	0.052		2170 ± 100	1.91 ± 0.23
	0.100	3910 ± 430	2050 ± 99	1.67 ± 0.19
	0.149	3390 ± 340	2030 ± 101	1.78 ± 0.19
	0.197	2740 ± 250	1536 ± 91	1.74 ± 0.18
	0.246	2140 ± 170	1233 ± 83	1.34 ± 0.13
	0.295	1620 ± 110	1214 ± 86	1.11 ± 0.11
	0.343	1247 ± 75	1124 ± 86	1.10 ± 0.11
	0.392	968 ± 58	882 ± 79	1.01 ± 0.11
	0.440	734 ± 37	730 ± 75	1.02 ± 0.14
	0.489	544 ± 27	536 ± 66	0.54 ± 0.06
	0.538	415 ± 21	772 ± 82	0.75 ± 0.12
	0.586	303 ± 15	402 ± 62	0.61 ± 0.11
	0.635	210 ± 11	345 ± 59	0.48 ± 0.10
	0.683	124.4 ± 6.2	260 ± 53	0.27 ± 0.06
	0.732	60.3 ± 3.0	219 ± 50	
	0.781		34 ± 23	
	0.829		12^{+17}_{-12}	
	0.878		≤ 13	
	0.926		≤ 14	
	0.975		0	

Table IV.2 (continued)

$p_\perp^2$	x_3	$\rho = Ed^3\sigma/dp^3$ ($\mu b\text{-}c^3/GeV^2$) $P_{beam}=12.4$	$P_{beam}=6.6$	Ratio $\rho_{12.4}/\rho_{6.6}$
0.41	0.052	1280 ± 140	573 ± 61	2.24 ± 0.34
	0.100	1210 ± 120	547 ± 60	2.20 ± 0.33
	0.149	1066 ± 96	530 ± 60	2.01 ± 0.29
	0.197	919 ± 73	431 ± 55	2.13 ± 0.32
	0.246	768 ± 54	544 ± 63	1.41 ± 0.19
	0.295	641 ± 38	441 ± 58	1.45 ± 0.21
	0.343	525 ± 32	376 ± 56	1.40 ± 0.22
	0.392	395 ± 20	286 ± 50	1.38 ± 0.25
	0.440	302 ± 15	222 ± 45	1.36 ± 0.29
	0.489	211 ± 11	159 ± 40	1.33 ± 0.34
	0.538		108 ± 34	
	0.586		115 ± 36	
	0.683		23 ± 30	
	0.732		36 ± 24	
	0.781		13 ± 18	
	0.829		13	
	0.878		14[a]	
	0.926		0	
1.03	0.057		41 ± 23	
	0.105	97.2± 6.8	32 ± 21	3.0 ± 2.0
	0.153	84.6± 5.9	11 ± 15	8 ±11
	0.201	73.4± 5.1	43 ± 24	1.7 ± 1.0
	0.250	64.3± 3.9	33 ± 22	2.0 ± 1.3
	0.298	52.7± 2.6	≤11	4.6
	0.346	40.9± 2.0	57 ± 28	0.71 ± 0.35
	0.394	32.7± 1.6	≤12	2.6

Table IV.2 (continued)

$p_\perp^2$	x_3	$\rho = Ed^3\sigma/dp^3$ ($\mu b\text{-}c^3/GeV^2$) $P_{beam}=12.4$	$P_{beam}=6.6$	Ratio $\rho_{12.4}/\rho_{6.6}$
1.03	0.442	23.4 ± 1.2	12 ± 17	2.0 ± 2.8
	0.491	15.98 ± 0.80	<12	>1.3
	0.539	10.12 ± 0.51	<13	>0.74
	0.587	5.89 ± 0.29	<13	>0.43
	0.635	3.23 ± 0.16	<14[a]	>0.22
	0.683	1.53 ± 0.09	<14[a]	>0.10
	0.732	0.628 ± 0.044	0	

a. This data point is not plotted on fig. 3 in order to avoid a confused figure. This upper limit represents a single data point at the center of the bin. Also, part of the bin is beyond the kinematic limit.

We also compare our data with the 12 and 24 GeV/c bubble chamber experiment of Mück et al. (Mu-1, 3). To investigate the s dependence of the structure function ρ, we plot ρ against $s^{-1/4}$, as suggested by Abarbanel (Ab-1), for fixed values of $p_\perp$ and x. In fig. 4 we take $x \approx 0$, and plot the distribution for fixed $p_\perp$ values. (Also see table 3.) In fig. 5, we take $p_\perp = 0.2$ GeV/c, and plot the distribution for fixed x_1 values. In both cases we see that the data are consistent with an $s^{-1/4}$ dependence, although it can be fit by other s dependences as well. (The straight lines are drawn to guide the eye.) Finally, fig. 6 is Ferbel's graph (Fe-2) with our points added to it. [Here ρ has been integrated over $p_\perp^2$ at $x = 0$, and the result multiplied by $\pi/\sigma_{T\infty}$ where $\sigma_{T\infty}$ is the pp cross section at infinite energy.]

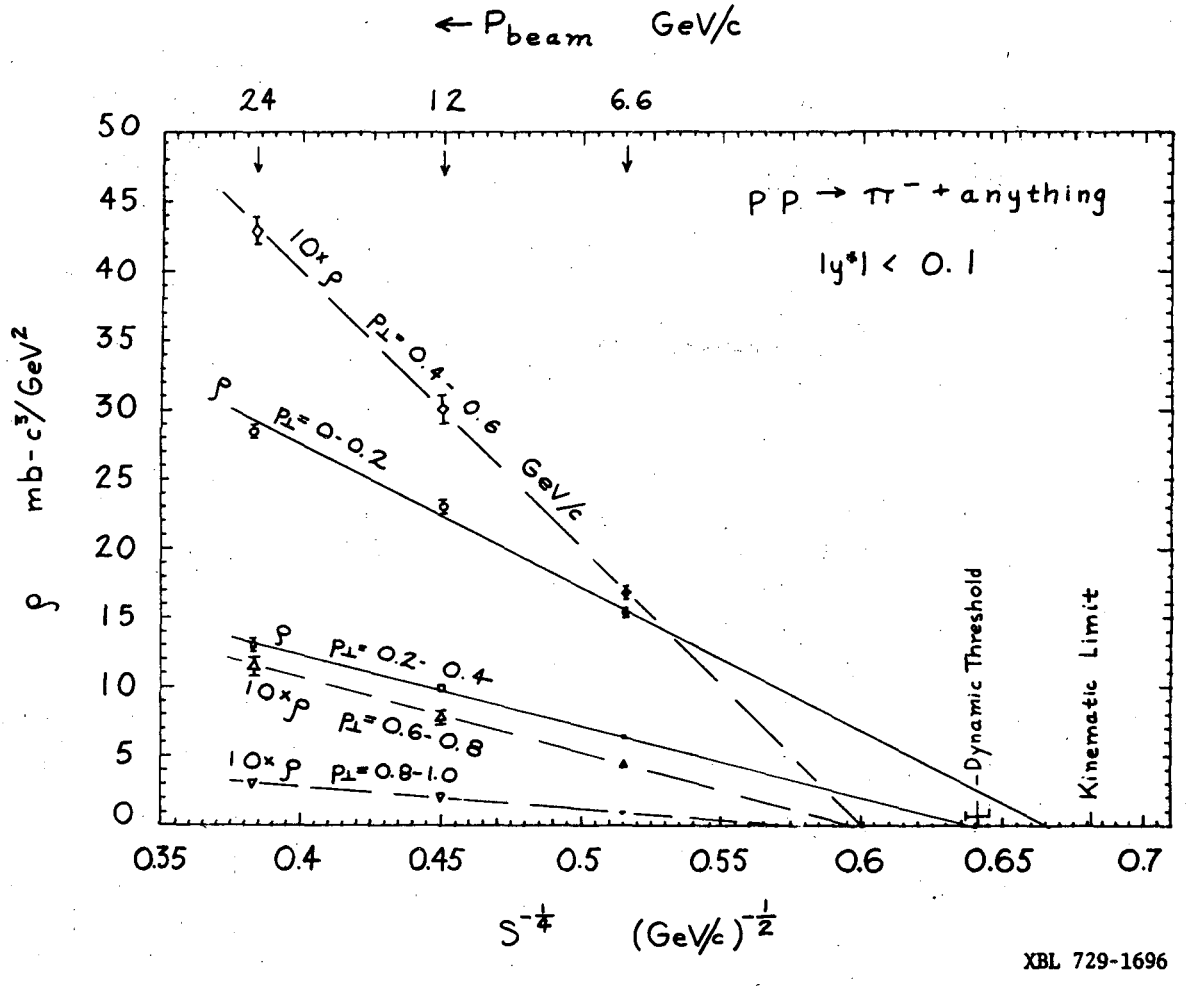

Fig. IV.4 $\rho = Ed^3\sigma/dp^3$ vs. $s^{-\frac{1}{4}}$ for $pp \rightarrow \pi^-$ + anything for 5 intervals in $p_\perp$ and $|y^*| < 0.1$ (see eqn. II.B.7 for def. of y^*). The data are from this experiment (6.6 GeV/c) and Muck et al. (12 and 24 GeV/c - ref. Mu-1). Please note: We plot $10 \times \rho$ rather than ρ for $p_\perp \gtrsim 0.4$ GeV/c.

Table IV.3. A comparison of this experiment (6.6 GeV/c) and Mück et al. (12 and 24 GeV/c - ref. Mu-1) for the reaction $pp \rightarrow \pi^- +$ anything for $|y^*| \leq 0.1$ [tabulation of data in fig. 4]

$\rho = Ed^3\sigma/dp^3$ ($\mu b - c^3/GeV^2$) for $|y^*| \leq 0.1$

$p_\perp$ (GeV/c)	p_{beam}=24 GeV/c	p_{beam}=12 GeV/c	p_{beam}=6.6 GeV/c	Ratio ρ_{24}/ρ_{12}	Ratio $\rho_{12}/\rho_{6.6}$
0 - 0.2	28100 ± 1200	22930 ± 760	15170 ± 480	1.225 ± 0.067	1.511 ± 0.064
0.2 - 0.4	13060 ± 470	10040 ± 300	6220 ± 180	1.301 ± 0.061	1.614 ± 0.067
0.4 - 0.6	4260 ± 190	2970 ± 110	1645 ± 72	1.434 ± 0.083	1.81 ± 0.10
0.6 - 0.8	1128 ± 84	780 ± 55	449 ± 32	1.45 ± 0.15	1.74 ± 0.17
0.8 - 1.0	303 ± 31	202 ± 19	90 ± 13	1.5 ± 0.26	2.24 ± 0.39

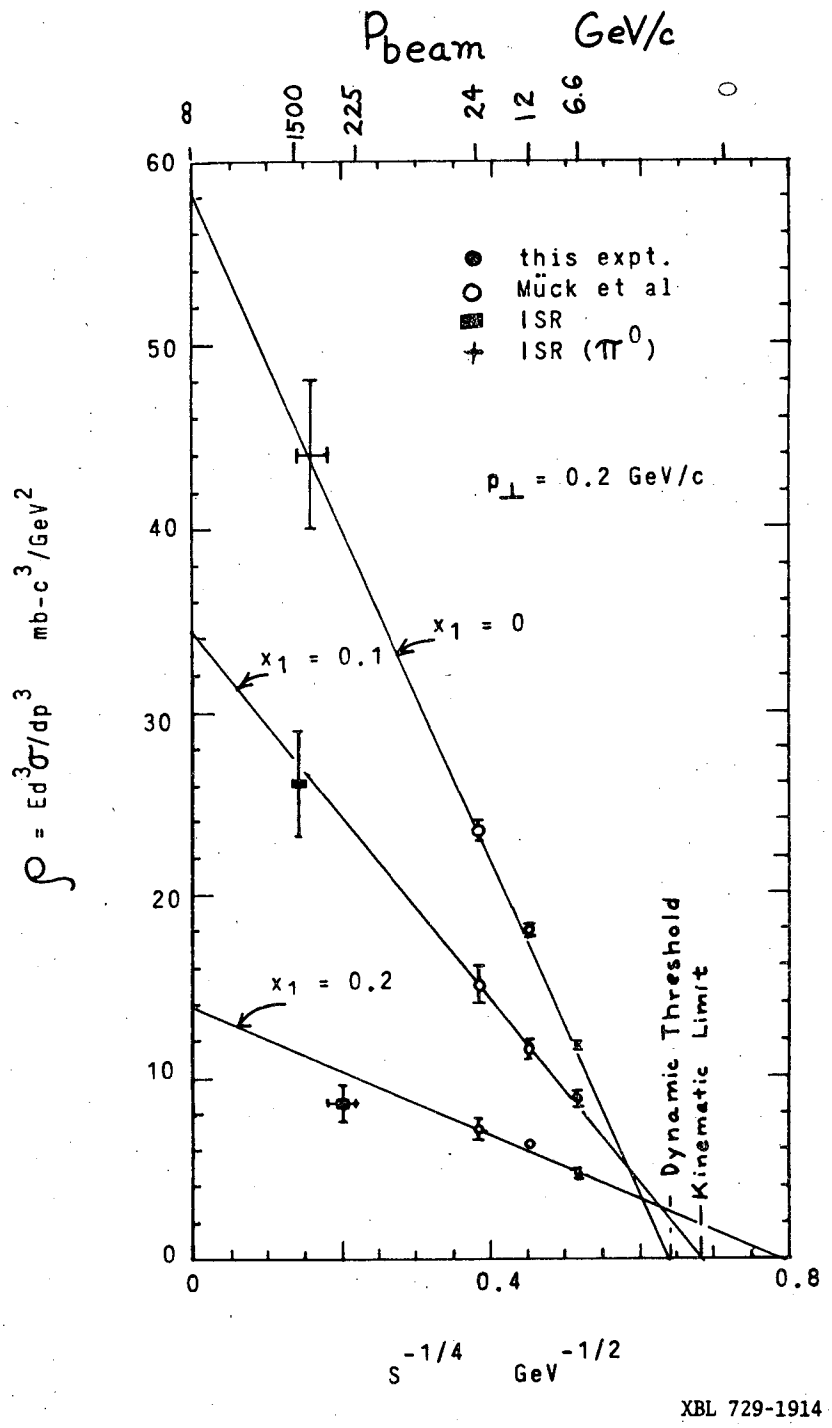

Fig. IV.5 ρ vs. $s^{-1/4}$ for $pp \rightarrow \pi^-$ + anything for x_1 =,0, 0.1, and 0.2, and $p_\perp$ = 0.2 GeV/c. The data are from this expt. (6.6 GeV/c), Mück et al. (12.& 24 GeV/c - ref. Mu-1), an ISR expt. (225 to 1500 GeV/c - ref. Be-6), and a value calculated from π^0 production at the ISR (as plotted by Mück et al.). The straight lines are drawn through the points by eye.

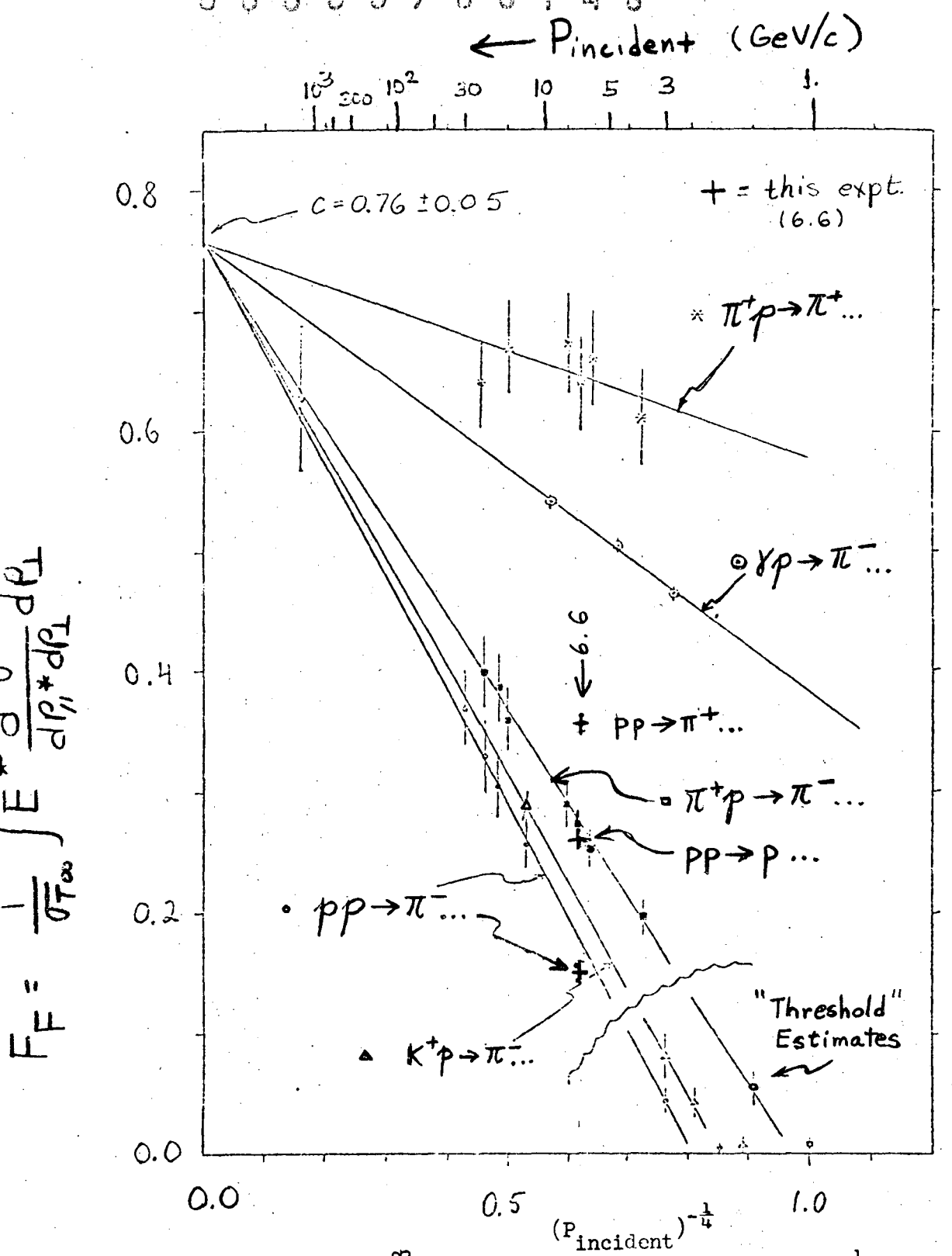

Fig. IV.6 $F_F(0) = \frac{1}{\sigma_{T\infty}} \int_0^\infty E^*(d^2\sigma/dp_{||}^* dp_\perp) dp_\perp \Big|_{p_{||}^*=0}$ vs. $P_{incident}^{-\frac{1}{4}}$ for the reactions xp → y + anything, where x = p, K^+, π^+, or γ and y = $\pi^\pm$ or p. This is Ferbel's plot (ref. Fe-2) with the π^- point for this experiment replotted correctly and the π^+ and proton points added (see section V).

C. Comparison with Higher Energy Using the Rapidity

Still a third variable that is sometimes advocated in comparing inclusive data is the lab. rapidity variable, $y = \tanh^{-1}\left[p_{\parallel}(\text{lab})/E(\text{lab})\right]$. In fig. 7 we compare our data with Akerlof et al.'s in this variable. The exact same set of points are plotted as in fig. 2 Because we are still in the lab., the curves will agree and disagree for exactly the same points as on fig. 2. To make a plot of f vs. $y-y_{min}$, we would shift each set of points rigidly to the right, but Akerlof et al.'s points would be shifted further right than ours, because y_{min} is less for their points. We indicate the relative shift of their points by attaching a rightward pointing arrow to some of them. For the lowest $p_{\perp}$, the curves would have a crossover point.

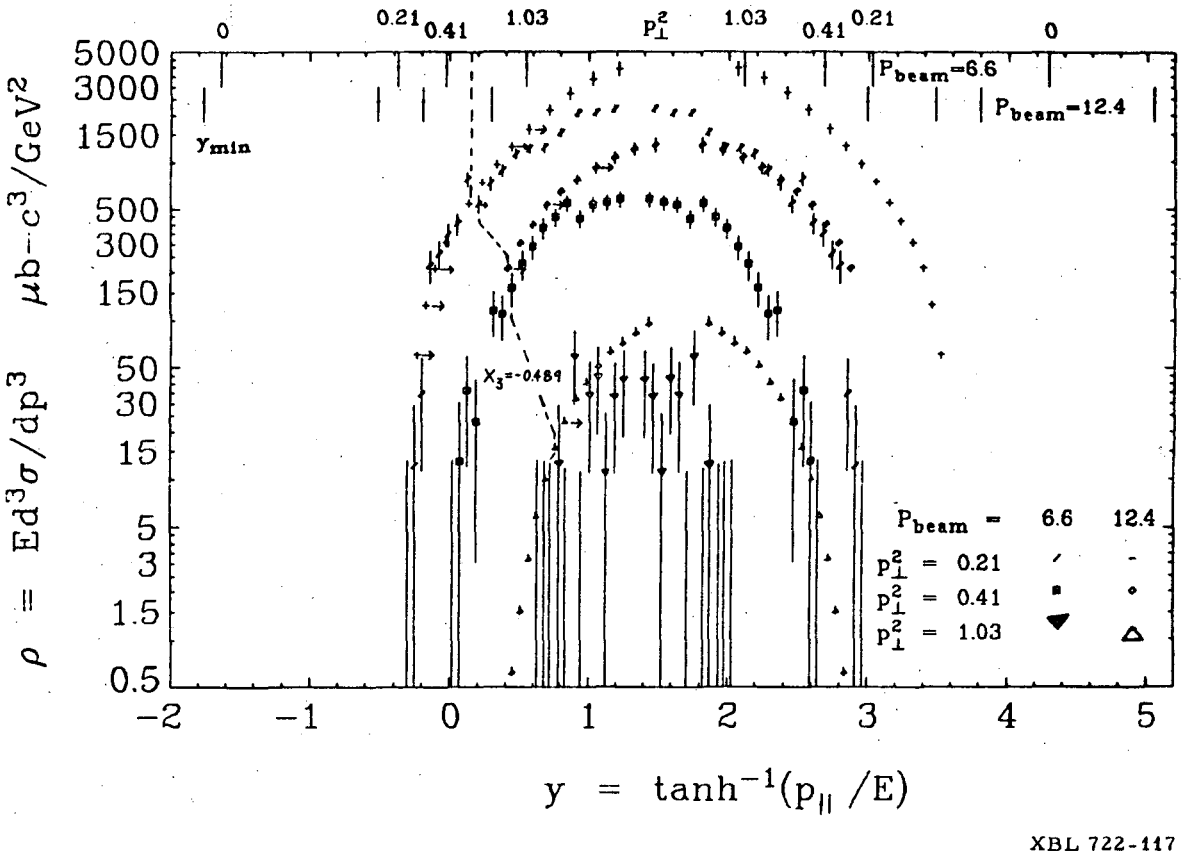

XBL 722-117

Fig. IV.7 ρ vs. y for $p_\perp^2$ = 0.21, 0.41, and 1.03 $(GeV/c)^2$ for $pp \to \pi^-$ + anything. A comparison of this experiment (6.6 GeV/c) with Akerlof et al. (12.4 GeV/c - ref. Ak-1). A broken line joins points having $|x_3|$ = 0.489. This graph is obtained by transforming the points of fig. 3. Please note: the data point is at the apex of the triangle symbols, viz. △ and ▽. It is at the center of all other symbols.

D. One Dimensional Distributions for This Experiment

1. Longitudinal and transverse Distributions: 4-prongs, 6-prongs, and Combined Data

Various longitudinal distributions for the 4-prongs, 6-prongs, and combined 4 and 6-prong sample are presented. First we plot (fig. 8a) the integrated structure function F_F vs. x_2, where

$$F_F(x_2,s) = \frac{1}{\sigma_{T\infty}} \int_0^{p_{\perp,max}^2} E(d^2\sigma/dp_{||}^* dp_\perp) dp_\perp . \qquad \text{IV.D.1}$$

The 6-prongs contribute only to the center of the plot. The error bars attached to the data points represent the statistical errors only. We also plot the laboratory differential cross section (fig. 8b), and the integrated structure function B(y,s) (eqn. II.C.10) vs. the laboratory rapidity, y (fig. 8c). The error bar at a in fig. 8c is the 6-prong normalization error, and the error bar at b (which is smaller than the symbol to which it is attached) is the maximum contribution that this error can make to the error of the combined sample.

We also plot the transverse distribution $G_2(p_\perp,s)$ vs. $p_\perp^2$, where G_2 is given by eqn. II.C.14 (fig. 8d). We draw 2 exponentials (straight lines on the semi-log plot) through the "all-prong" data points. They seem to represent the data fairly well. The "break-point" between the steep and less-steep exponential seems to be at about $p_\perp^2 = 0.24$ $(GeV/c)^2$. (The three points nearest the "break-point" are 20 to 30 °/o too high, but all the remaining points are within 10 °/o of one of the curves.) This "double-exponential" fall-off with $p_\perp^2$ is well known.

Not surprisingly, the 6-prongs have a steeper decrease with $p_\perp^2$ than the 4-prongs.

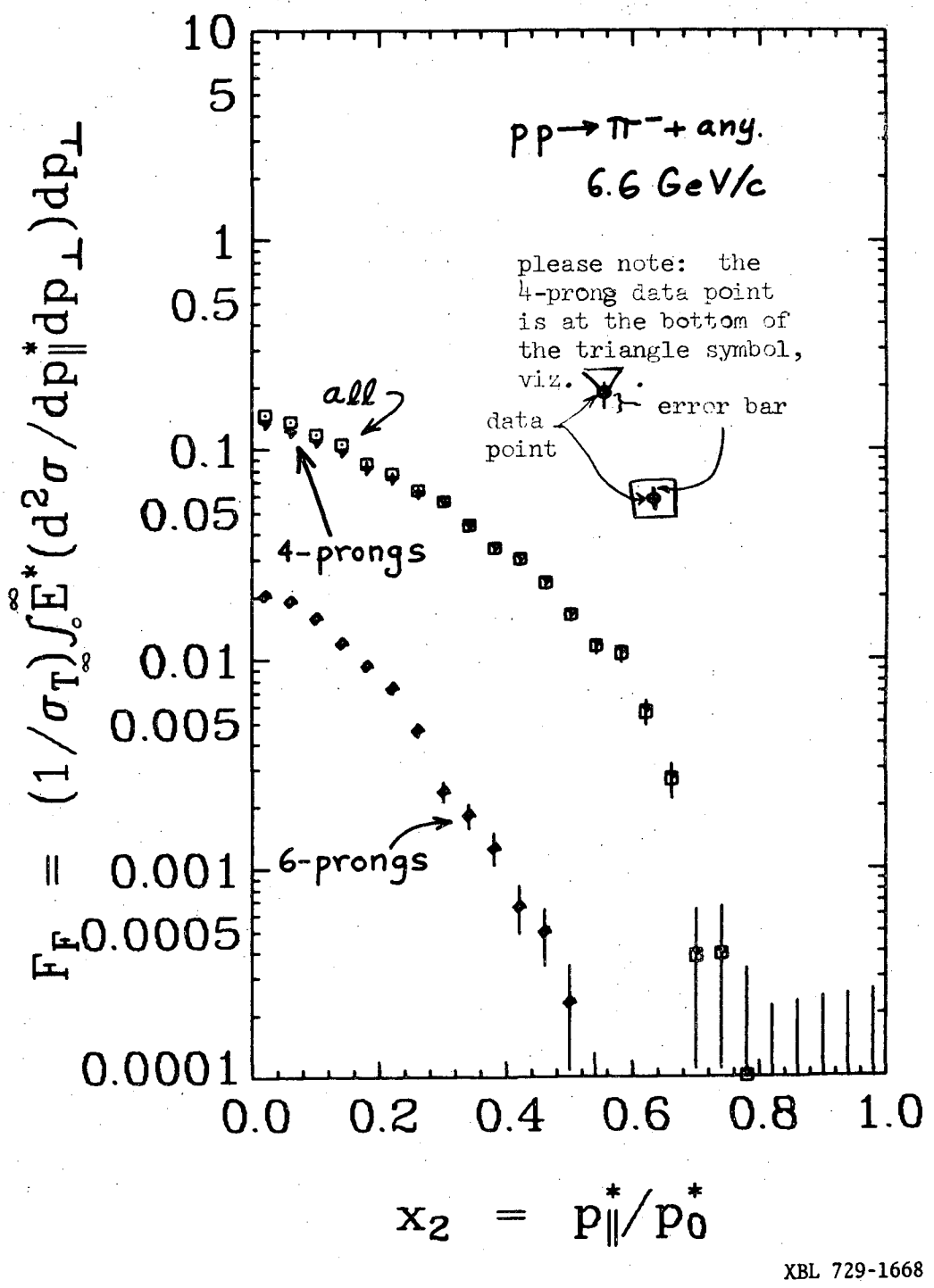

XBL 729-1668

Fig. IV.8 Longitudinal and transverse distributions for π^-'s from pp → π^- + anything at 6.6 GeV/c. The upper curve of each plot (□) is the combined 4 and 6-prong sample, wheras the lower two curves of each plot are the individual 4 and 6-prong samples, respectively. The error bars for the combined data do not include the effect of the ±12% uncertainty in the cross-section ratio σ_6/σ_4, which causes a maximum error of ± 2 % in the combined data. The overall normalization error of ± 5 % is not shown.

a. F_F vs. x_2 (using $\sigma_{T\infty}$ = 39.5 mb)

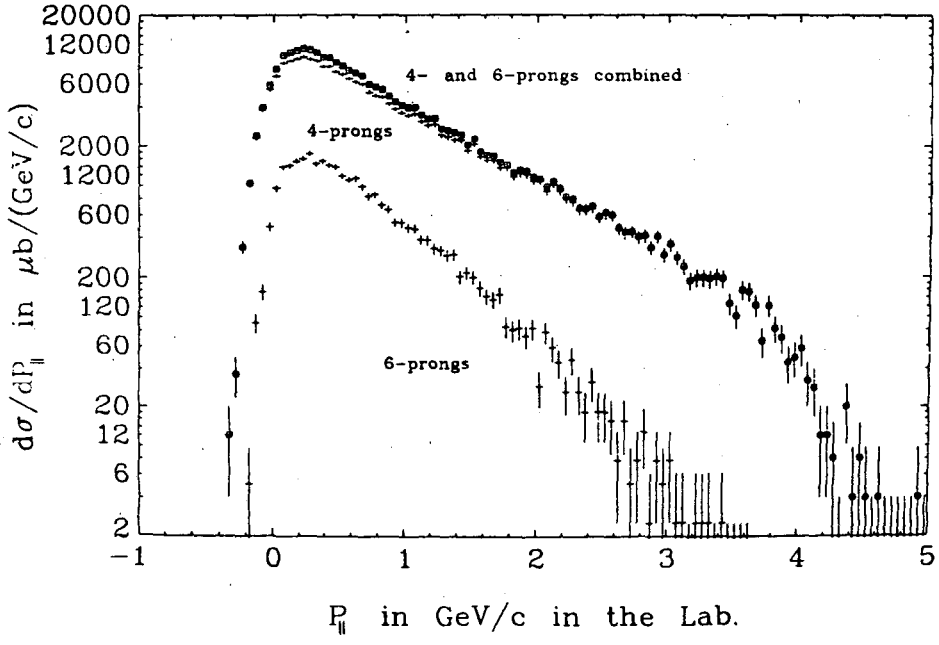

IV.8b. $d\sigma/dp_{\parallel}$ vs. $p_{\parallel}$(lab)

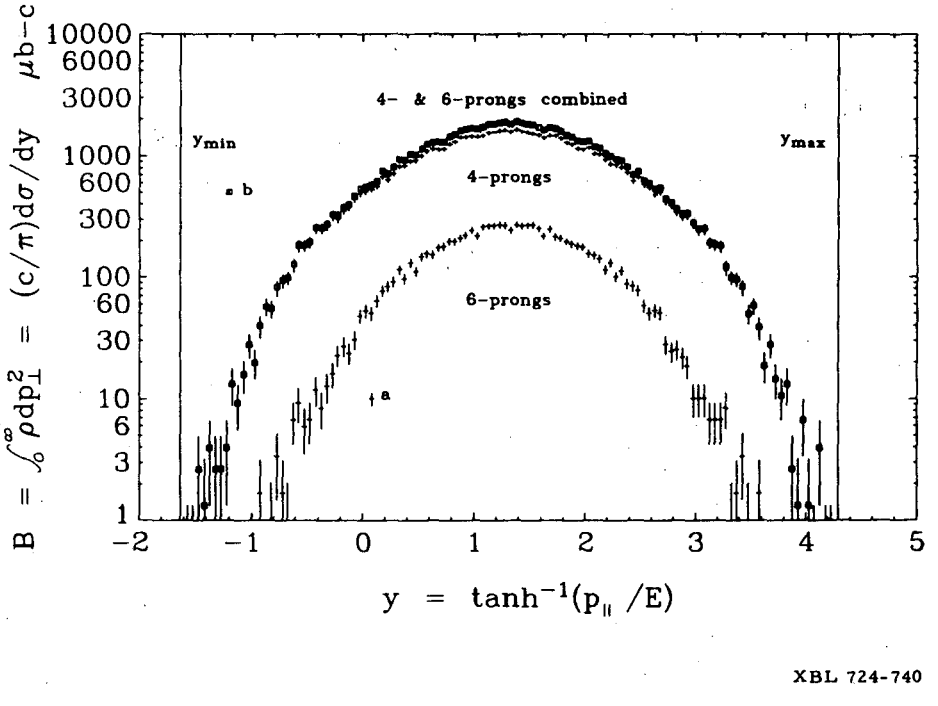

XBL 724-740

IV.8c. B(y,s) vs. y, where y is the rapidity
(Point a is a typical 6-prong data point with a ± 12% error, and point b is a typical combined data point with a ± 2% error.)

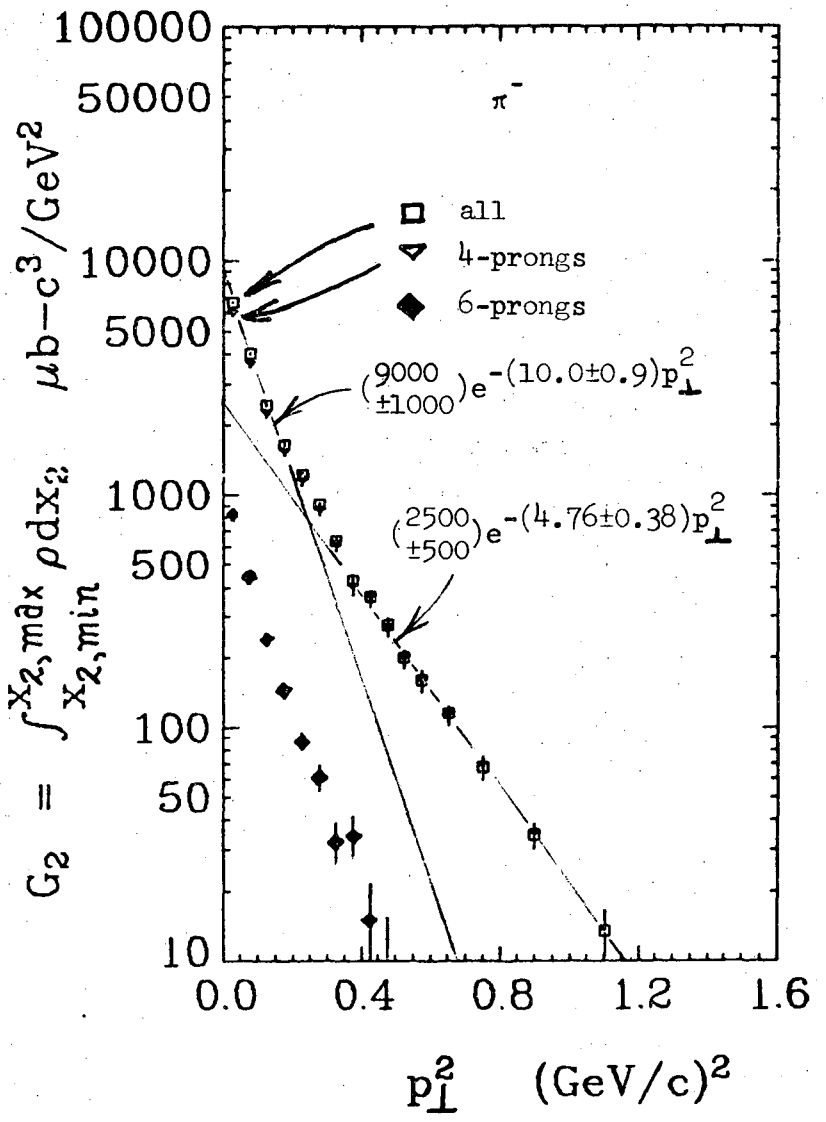

IV.8d G_2 vs. $p_\perp^2$. The 2 straight lines are fit to the "all-prong" data points by eye.

Please note: the 4-prong data point is at the bottom of the triangle symbol.

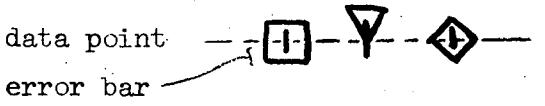

2. Longitudinal and Transverse Distributions According to the Number of π's in the Final State and Combined Data.

We plot π^- distributions both according to the number of produced pions (including neutrals) and for the total sample. In fig. 9 we plot F vs x_3, where F is defined by equation II.C.8; and G_3 vs. p^2, where G_3 is defined by equation II.C.14. The various reactions giving different numbers of pions are listed in Table 4. Table 4 also gives the cross sections for these different reactions.

In order to more easily see the fraction of F and G contributed by each of the various final states, we also plot F/F_{total} and G/G_{total} (fig. 10). Figures 10a and 10d show that the two 3π final states are similar in shape and magnitude, except for small x or small $p_\perp^2$, where the final state containing the neutron is larger.

Table IV.4 π^- production cross sections according to the number of π's in the final state for $pp \to \pi^-$ + anything at 6.6 GeV/c

	Reaction	π^- Production Cross Section[a]
2π's	$pp \to pp\pi^+\pi^-$	2.90 ± 0.12 mb[b]
3π's	$pp \to pp\pi^+\pi^-\pi^o$	2.29 ± 0.09 mb[b]
	$pn\pi^+\pi^+\pi^-$	2.77 ± 0.11 mb[b]
4π's	$pp \to pp\pi^+\pi^-$ mm (mm $\geq 2\pi^o$'s)	
	$p\pi^+\pi^+\pi^-$ mm (mm $\geq$ n + π^o)	2.36 ± 0.10 mb[b,c]
	$\pi^+\pi^+\pi^+\pi^-$ mm (mm $\geq$ 2n's)	
	all 6-prongs	1.45 ± 0.19 mb

a. See text for a definition of the production cross section.

b. Statistical error and normalization error only - does not include systematic errors of up to 10% from wrong fits.

c. We have neglected the small amount of $d\pi^+\pi^+\pi^-$ final states in our plots of the 3π sample. The total 4-prong cross section includes deuteron final states.

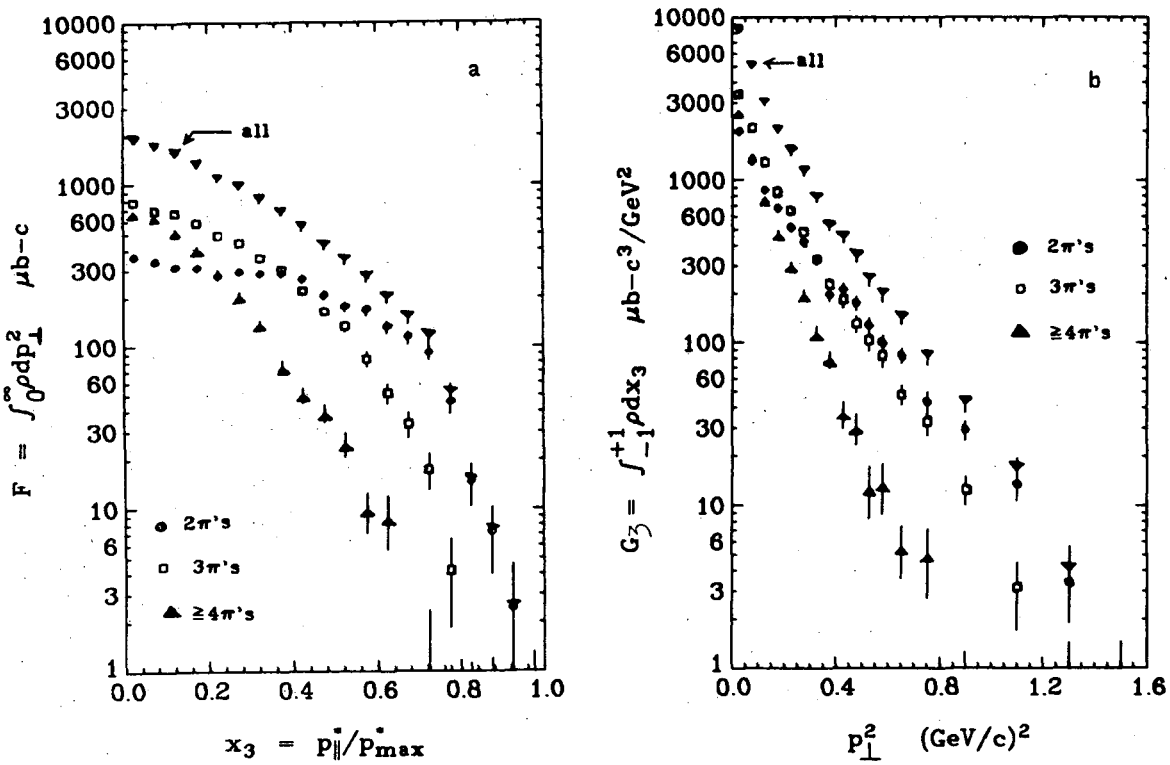

Fig. IV.9 Spectra for 2π, 3π, and $\geq 4\pi$ final states (as well as the combined data for all final states) for $pp \rightarrow \pi^- +$ anything at 6.6 GeV/c.

a. F vs. x_3

b. G_3 vs. $p_\perp^2$

Please note: the data point is at the apex of the triangle symbols, viz. △ and ▽.

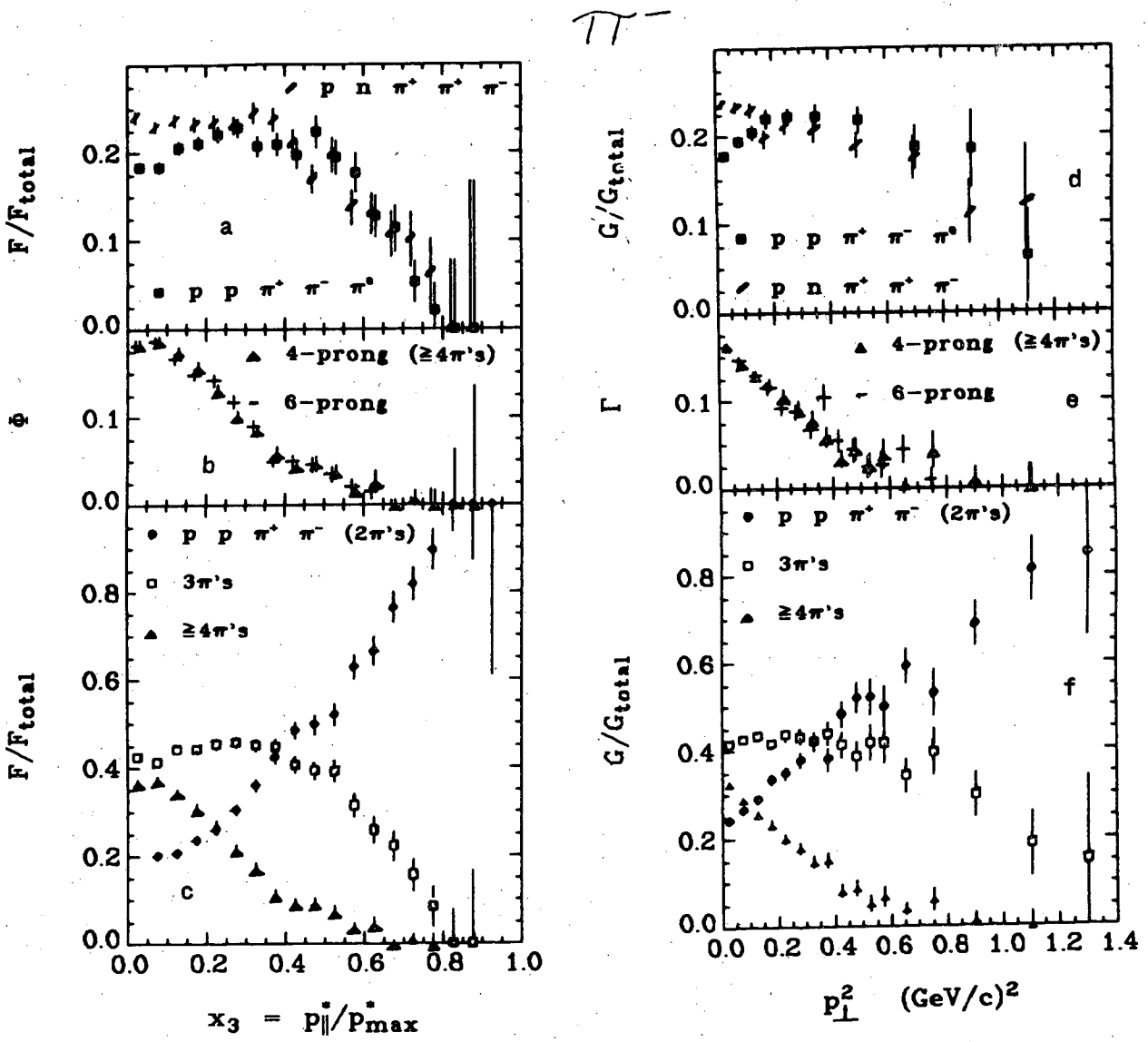

Fig. IV.10 Fractional contributions of various final states to $\underline{F}$ and $\underline{G}$ (see fig. caption for definitions of $\underline{F}$ and $\underline{G}$.) for $pp \to \pi^- +$ anything at 6.6 GeV/c.

a. F/F_{total} vs. x_3 for the two 3π final states: $pp\pi^+\pi^-\pi^o$ and $pn\pi^+\pi^+\pi^-$.

b. Φ vs. x_3 for the two contributions to 4π final states: 4-prongs ($\geq 4\pi$ only) and 6-prongs (all are $\geq 4\pi$). (See text for details.)

c. F/F_{total} vs. x_3 for 2π, 3π, and $\geq 4\pi$ final states.

d. G/G_{total} vs. $p_\perp^2$ for the two 3π final states; $pp\pi^+\pi^-\pi^o$ and $pn\pi^+\pi^+\pi^-$.

e. Γ vs. $p_\perp^2$ for the two contributions to $\geq 4\pi$ final states: 4-prongs ($\geq 4\pi$ only) and 6-prongs (all are $\geq 4\pi$) (see text).

f. G/G_{total} vs. $p_\perp^2$ for 2π, 3π, and $\geq 4\pi$ final states.

(Please note: the data point is at the apex of the triangle symbols, viz. Δ and ∇.)

Next, we investigate the different reactions having four or more π's in the final state. Aside from a small number of deuteron events, the 4-prong final states in this class all produce unconstrained fits. We do not attempt the difficult task of separating these unconstrained fits. Instead, we compare the 6-prongs with all those 4-prongs having four or more π's in the final state (Of course, all the 6-prongs are produced with four or more π's.). The cross sections for these two processes are quite different (table 4). Despite this, the shapes of the $\underline{F}$ and $\underline{G}$ distributions for both of these processes are in very good agreement. In order to see this, for each process we normalize $\underline{F}$ and $\underline{G}$ to the π^- production-cross-section for that process.

Let $\underline{a}$ represent the 4π 4-prongs and $\underline{b}$ represent the 6-prongs. The most obvious way to normalize F_a is to define

$$\varphi_a = F_a/\sigma_a \qquad \text{IV.D.3}$$

We could then compare φ_a and φ_b. We can equally well multiply φ_a and φ_b by some function of $p_\perp$ and $\underline{x}$, and then make the same comparison. In fact, for convenience, we do just that. We define

$$\Phi_a = \left[\tfrac{1}{2}\left(\frac{\sigma_a + \sigma_b}{F_{total}}\right)\right]\frac{F_a}{\sigma_a} \qquad \text{IV.D.4}$$

and

$$\Gamma_a = \left[\tfrac{1}{2}\left(\frac{\sigma_a + \sigma_b}{G_{total}}\right)\right]\frac{G_a}{\sigma_a} \qquad \text{IV.D.5}$$

(F_{total} is the $\underline{F}$ for π^- independent of the number of π's produced.) Then, in figure 10b and 10e, we plot Φ vs x_3 and Γ vs. $p_\perp^2$. As previously mentioned, the shapes of these two distributions are in very good agreement.

{The term in brackets is adopted as a matter of convenience only. If F_a/σ_a and F_b/σ_b are equal, then $\sigma_a + \sigma_b = (F_a + F_b)/F_{total}$, and similarly for $\underline{G}$. This makes it easier to compare these two plots with the previous two plots.}

E. Two Dimensional Distributions for this Experiment

We now plot ρ for five equal intervals in $p_\perp$ from 0 to 1 GeV/c, against both x_3 and the rapidity, y (fig. 11). Fig 11 shows that ρ falls off more rapidly as x_3 increases. Also, it appears that the initial fall-off of ρ with x_3 is less rapid at higher values of $p_\perp$. In order to more clearly see any such differences in the shape of the ρ vs. x_3 curves for different $p_\perp$, we plot R vs. $p_\perp$ for six intervals in x_3 (fig. 11b), where R is defined by:†

$$R(x,p_\perp,s) = \rho(x,p_\perp,s)/\rho(0,p_\perp,s). \qquad \text{IV.E.1}$$

The first two data points in $p_\perp$, for all x_3, show a definite rise in R with $p_\perp$, a rise which generally becomes steeper with increasing $p_\perp$. The three curves representing the smallest x continue to rise, gradually flattening out, whereas the higher-x curves show a definite turnover before $p_\perp$ reaches its maximum value. The curves certainly are not flat. However, suppose that ρ could be factorized, i.e. suppose that we could write:

$$\rho(x,p_\perp,s) = g(x,s)h(p_\perp,s).$$

According to our definition of R, (eqn. 1) we would then have:

$$R(x,p_\perp,s) = g(x,s)/g(0,s) = R(x,s).$$

Therefore, the observed dependence of R upon $p_\perp$ means that ρ is not factorizable for this data.

---

†To be precise, R is the ratio of $\langle\rho\rangle_{av}$ for a bin in $p_\perp$ and x, as defined above, divided by $\langle\rho\rangle_{av}$ for a bin with the same $p_\perp$ boundaries and x_3 running from 0.0 to 0.1.

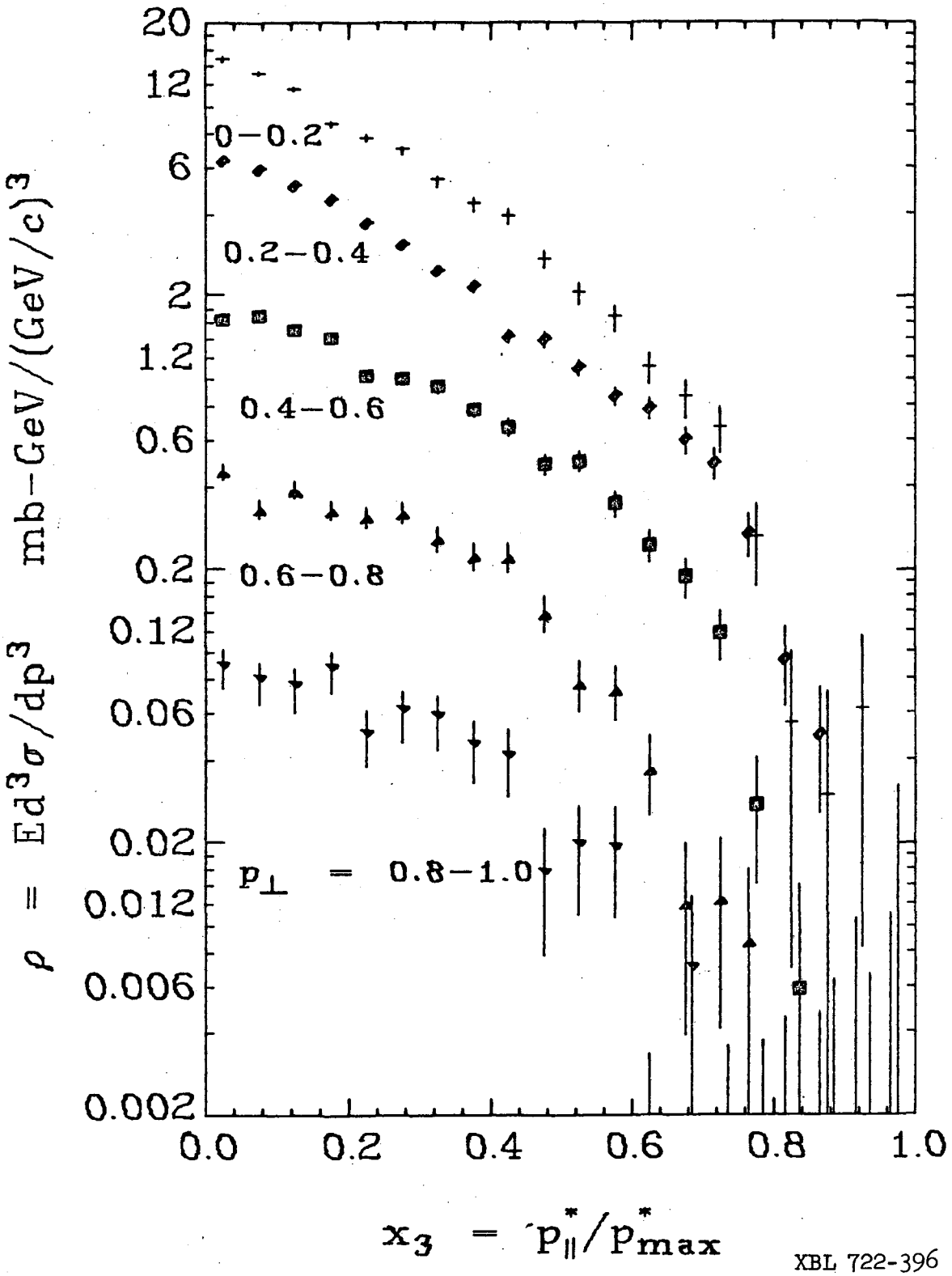

Fig. IV.11 Two dimensional spectra for $pp \rightarrow \pi^-$ + anything at 6.6 GeV/c
(please note: the data point is at the apex of the triangle symbols, viz. Δ and ∇ .)

a. ρ vs. x_3 for 5 intervals in $p_\perp$.

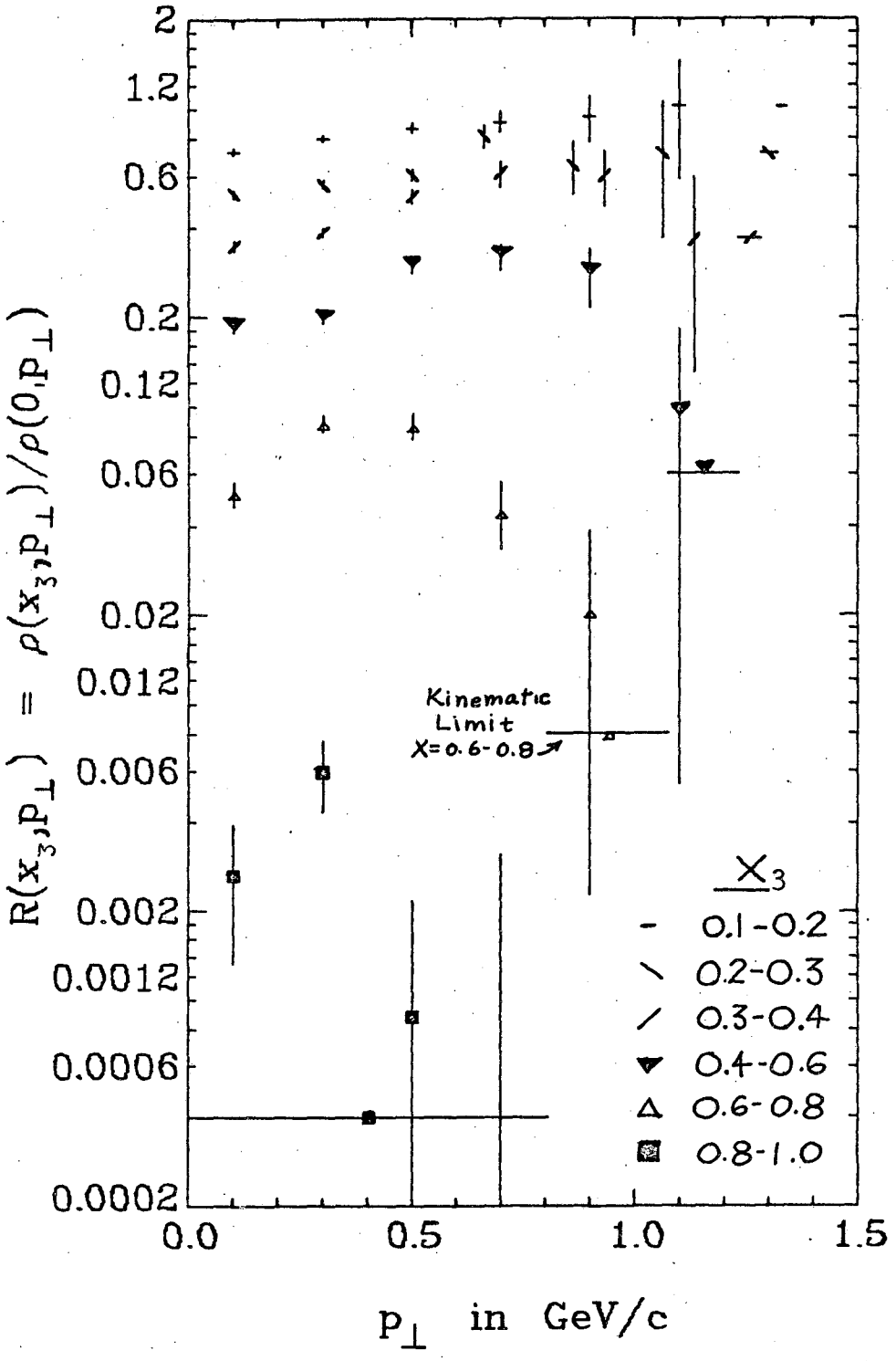

XBL 722-384

Fig. IV.11 Two dimensional spectra for $pp \rightarrow \pi^-$ + anything at 6.6 GeV/c...

b. $R(x_3,p_\perp,s)$ vs. $p_\perp$ for 6 intervals in x_3, where $R(x_3,p_\perp,s) = \rho(x_3,p_\perp,s)/\rho(0,p_\perp,s)$. For $\rho(x_3 = 0)$ we actually use $\langle\rho(x_3 = 0 - 0.1)\rangle_{av}$. The symbols with horizontal error bars are not data points, but represent $p_{\perp,max}$ for each x_3-interval. The low end of each error bar is $p_{\perp,max}$ for the highest x_3 in the x_3-interval.

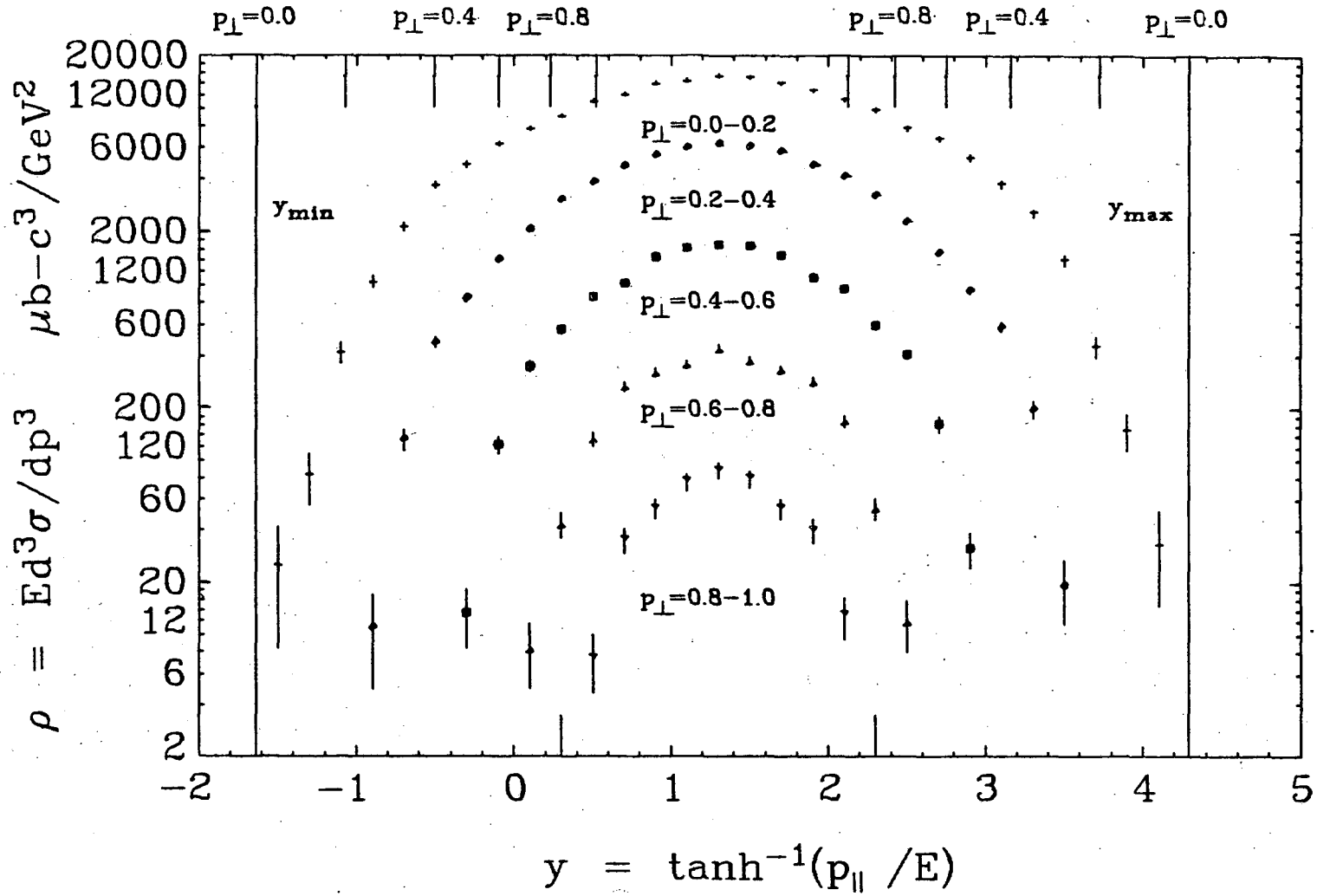

XBL 722-386

Fig. IV.11 Two dimensional spectra for $pp \rightarrow \pi^-$ + anything at 6.6 GeV/c ...

c. ρ vs. y for 5 intervals in $p_\perp$ (the lab. rapidity $y = \tanh^{-1}(p_{||}/E)$.)

F. Average Transverse Momentum

In this section we present the average transverse π^- momentum, for all events, and for the 4 and 6-prong samples separately (Table 5). We observe that $\langle p_\perp \rangle_{av}$ is smaller for 6-prongs than for 4-prongs. This agrees with the previously mentioned fact that ρ falls off more steeply with $p_\perp^2$ if there are more π's in the final state (figs. 10b and 11b).

We also observe that $\langle p_\perp \rangle_{av}$ is increasing with increasing energy, although very slowly (Table 5). From 6.6 to 28.5 GeV/c incident momentum, $\langle p_\perp \rangle_{av}$ increases only about 17 °/o.

Previously we have observed that the ratio $\rho(12.4)/\rho(6.6)$ increases fairly rapidly with increasing $p_\perp$ (sections IV.A and IV.B). At first glance this might seem inconsistent with the slow increase of $\langle p_\perp \rangle_{av}$ with increasing energy. However, this is not so. Because ρ falls off exponentially with $p_\perp^2$ (fig. IV.9b), the ratio $\rho(12.4)/\rho(6.6)$ can increase rapidly with $p_\perp^2$, if $p_\perp^2$ is large, even though $\langle p_{av} \rangle_\perp$ is almost energy independent.

Table IV.5. Average π^- transverse momentum for $pp \rightarrow \pi^-$ + anything for incident momenta from 6.6 to 28.5 GeV/c

	P_{beam}					
	6.6	13[a]	18[a]	21[a]	24[a]	28.5[a]
$\langle p_\perp \rangle_{av}$ of π^-	0.272[b]	0.294	0.308	0.309	0.314	0.318
(GeV/c)	±0.004[c]	±0.006	±0.005	±0.005	±0.006	±0.006

a. From ref. Sm-1.

b. See table V.3 for a list of $\langle p_\perp \rangle_{av}$ according to the number of of prongs, for all 3 outgoing particles: π^-'s, π^+'s, and protons.

c. The quoted error for 6.6 GeV/c is the estimated measurement uncertainty. The statistical error and the uncertainty in the ratio $\sigma_{6\text{-prong}} / \sigma_{4\text{-prong}}$ yield a much smaller error, ± 0.0012 GeV/c.

A. Comparison with Higher Energies in the Laboratory System for π^+ Production

Dennis Smith (Sm-1) has not reported his π^+ distributions, so we cannot compare with him as we did for the π^-. There is, however, some data available from a 28.5 GeV/c bubble chamber experiment that was conducted at Brookhaven (Si-1, Pa-3). For three values of $p_\perp$, we plot $d^2\sigma/dp_\perp dp_{||}$ vs. $p_{||}$ (lab) for both the Brookhaven data and our own data (fig. 1). It is apparent that our cross section exceeds Brookhaven's cross section. In particular consider the interval $p_\perp = 0.2$ GeV/c and $-0.2 < p_{||} < 0.0$ GeV/c. Despite the poor statistics, it is obvious that our experiment has a larger differential cross section here than the higher energy experiment does. This is also true for the interval $p_\perp = 0.4$ GeV/c and $0 < p_{||} < 0.1$ GeV/c. This is very different from the situation for the π^- data, for which the differential cross section is energy independent in this region (for the π^- data look back at fig. IV.1e and f for the first interval and fig. IV.1c and d for the second interval).

A similar comparison is made with the 12.4 GeV/c counter data of Akerlof et al. (fig.2). For small or negative $p_{||}$, our cross section exceeds the higher energy cross section, in agreement with our comparison with the Brookhaven experiment.

We shall discuss possible reasons for this behavior in the next section, after first describing the behavior of φ near $x = 0$.

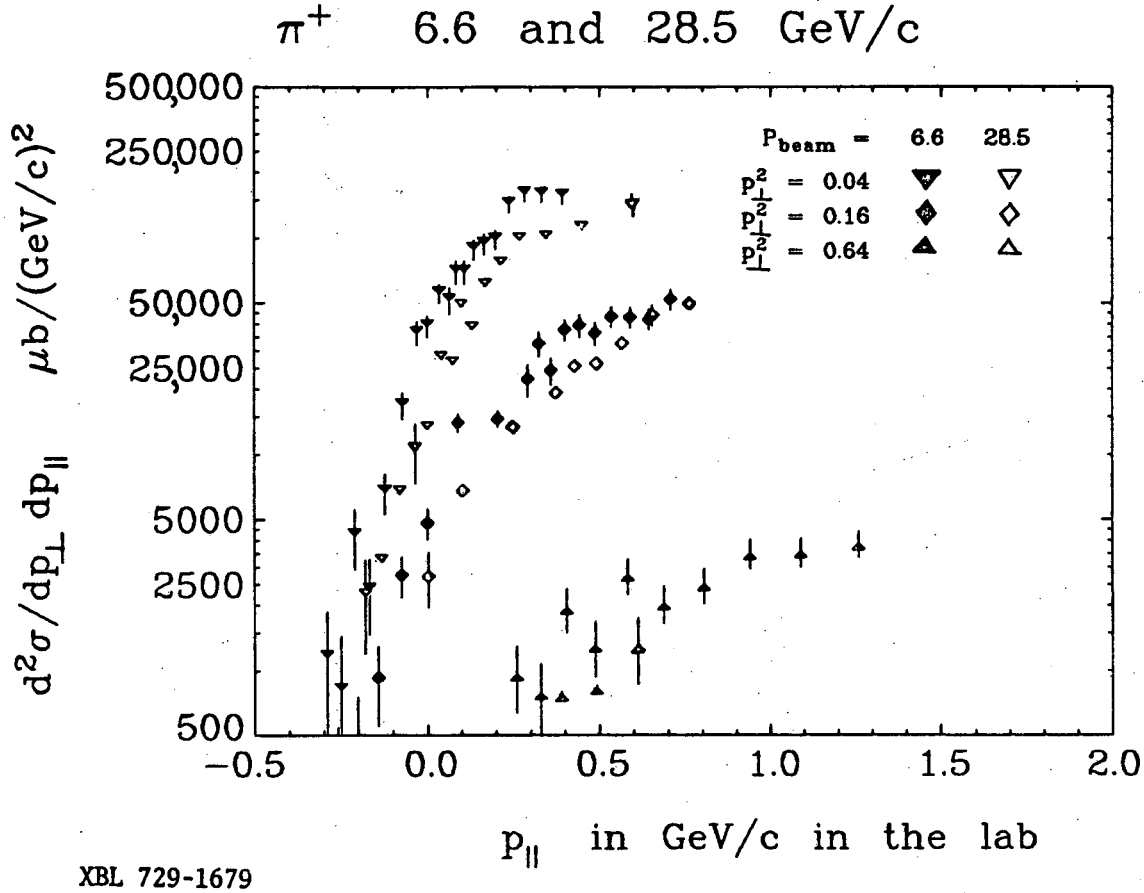

Fig. V.1 A comparison of this experiment (6.6 GeV/c) with Sims et al. (28.5 GeV/c - ref. Si-1) for $pp \rightarrow \pi^+ +$ anything: $d^2\sigma/dp_\perp dp_\parallel$ vs. $p_\parallel$(lab) for $p_\perp^2 = 0.04$, 0.16, and 0.64 $(GeV/c)^2$. [This graph is made by transforming the points of fig. 3.]

Please note: (1) The errors are not shown for most of Sims' data points because they are not shown in ref. Si-1.

(2) The data point is at the apex of the triangle symbols, viz. △ and ▽. It is at the center of the diamond: ◈.

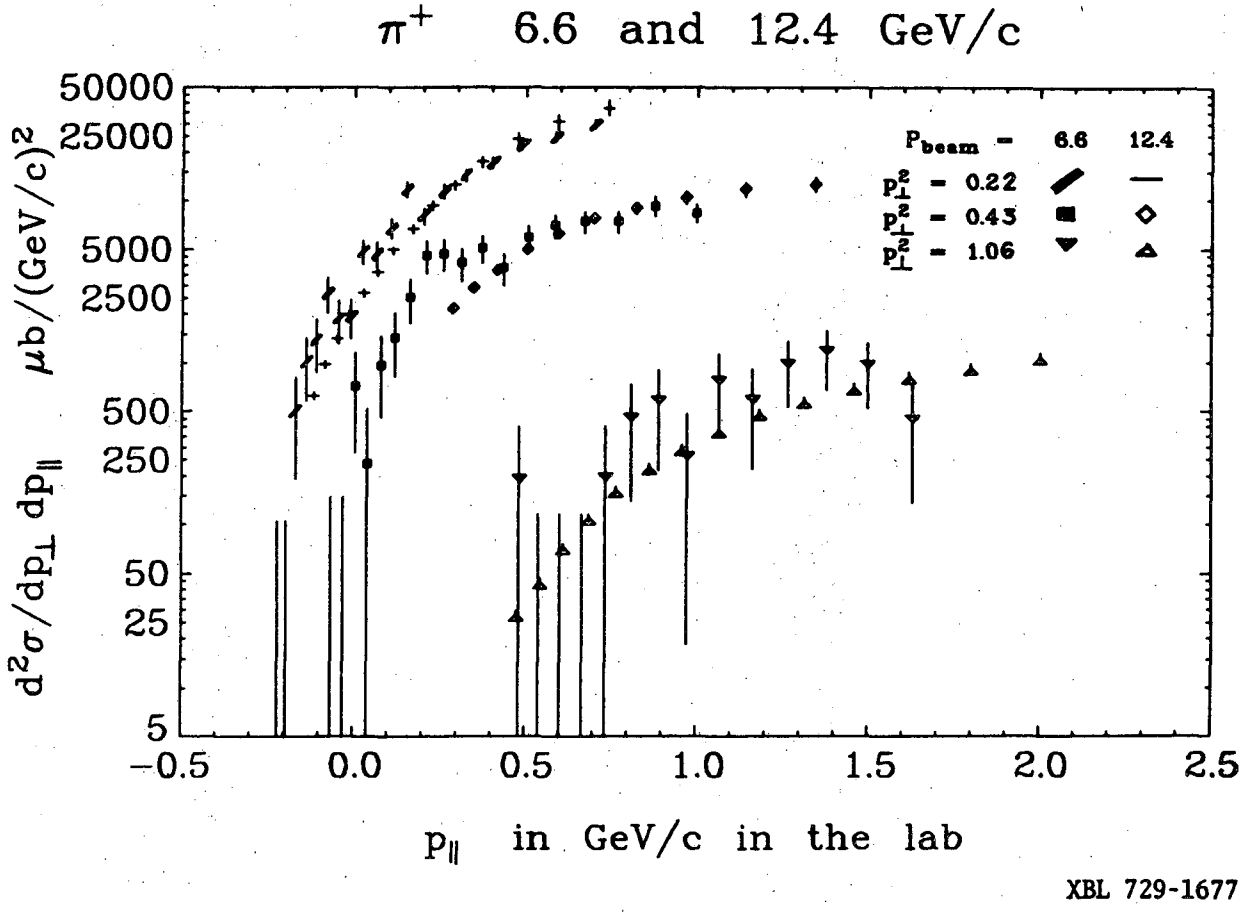

Fig. V.2 A comparison of this experiment (6.6 GeV/c) with Akerlof et al. (12.4 GeV/c - ref. Ak-1) for $pp \rightarrow \pi^+ +$ anything: $d^2\sigma/dp_\perp dp_\parallel$ vs. $p_\parallel$(lab) for $p_\perp^2 = 0.22$, 0.43, and 1.06 $(GeV/c)^2$. [This graph is made by transforming the points of fig. 5.]

Please note: the data point is at the apex of the triangle symbols, viz. △ and ▽.

B. Comparison with Higher Energies in the Central Region for π^+ Production

As previously mentioned, Feynman's x or the rapidity are the best variables for studying the central region ($p^*_{\parallel} \approx 0$). Therefore, we compare our data with the Brookhaven data at 28.5 GeV/c by making a graph and table of ρ vs. x_2 (fig. 3 and table 1).

For $p_\perp = 0.2$ GeV/c and $|x_2| < 0.2$, the average value of the ratio $\rho(28.5) / \rho(6.6)$ is 1.06 ± 0.06. The data points for the two energies are in agreement!

By way of comparison, for the π^- data, the average value of $\rho(28.5) / \rho(6.6)$ is 1.8 for this same interval. [The values of this ratio for the π^- are:

x_1	Ratio †
0	2.07 ± 0.06
0.1	1.81 ± 0.15
0.2	1.61 ± 0.15]

† The value of $\rho(28.5)$ used in calculating this ratio is determined by drawing a straight line through $\rho(24)$ and $\rho(6.6)$ on fig. IV.5.

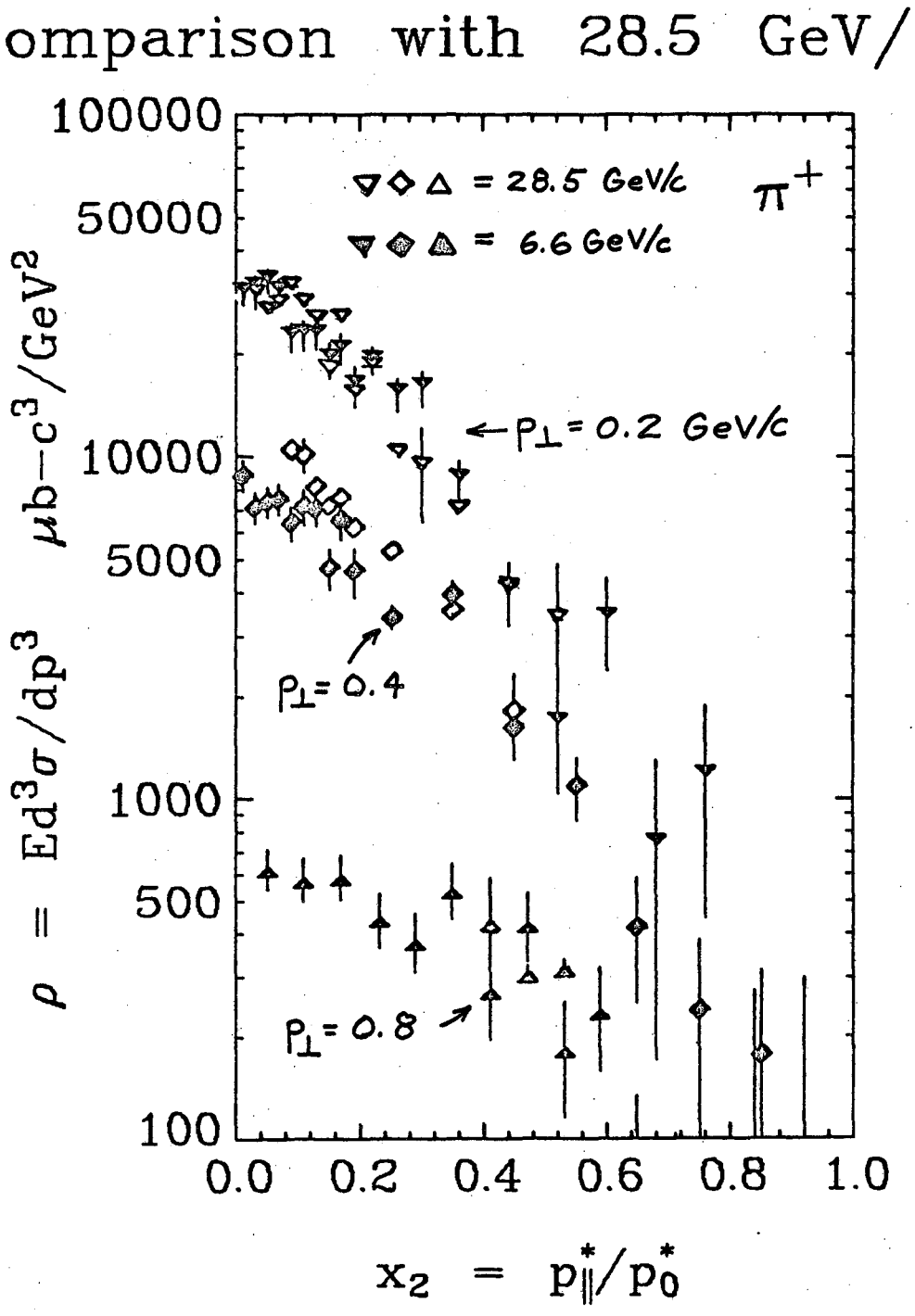

Fig. V.3 A comparison of this experiment (6.6 GeV/c) with Sims et al. (28.5 GeV/c - ref. Si-1 and Ha-2) for $pp \rightarrow \pi^+ +$ anything. ρ vs. x_2 for 3 values of $p_\perp^2$: 0.04 (▼ &▽), 0.16 (◆, ◇), and 0.64 (▲ & △) $(GeV/c)^2$. [The bins in x_2 and $p_\perp^2$ are the same for both experiments ($p_\perp^2$ = 0.035 to 0.045, 0.14 to 0.18, and 0.54 to 0.74 (GeV/c) respectively .]

XBL 729-1673

Table V.1. A comparison of this experiment (6.6 GeV/c) with Sims et al. (28.5 GeV/c - ref. Si-1 and Ha-2) for $pp \to \pi^+ + \text{anything}$: ρ vs. x_2 for three values of $p_\perp^2$. [Tabulation of the data in fig 3]

$p_\perp$ (GeV/c)	$p_\perp^2$ (GeV/c)	x_2	$\rho = Ed^3\sigma/dp^3$ ($mb\text{-}c^3/GeV^2$) [a] P_{beam} = 28.5 (GeV/c)	P_{beam} = 6.6 (GeV/c)	Ratio $\rho(28.5)/\rho(6.6)$
0.2	0.04	0.01	29.9 ± 2.9 [b]	30.1 ± 2.3	0.96 ± 0.12
		0.03	26.5 ± 2.9	31.3 ± 2.4	0.81 ± 0.11
		0.05	27.9 ± 2.9	32.7 ± 2.6	0.91 ± 0.12
		0.07	31.5 ± 2.9	30.5 ± 2.5	1.42 ± 0.19
		0.09	27.9 ± 2.9	22.2 ± 2.2	1.23 ± 0.18
		0.11	25.2 ± 2.9	22.6 ± 2.3	1.11 ± 0.17
		0.13	17.9 ± 2.9	22.7 ± 2.3	0.93 ± 0.19
		0.15	25.2 ± 2.9	19.2 ± 2.3	1.23 ± 0.20
		0.17	15.1 ± 2.9	20.5 ± 2.4	0.93 ± 0.22
		0.19	18.2 ± 2.9	16.2 ± 2.2	0.95 ± 0.18
		0.22	10.1 ± 2.9	19.1 ± 1.8	0.66 ± 0.20
		0.26	9.3 ± 2.9	15.2 ± 1.7	0.58 ± 0.20
		0.30	6.9 ± 2.4	15.9 ± 1.9	0.80 ± 0.30
		0.36	4.1 ± 1.8	8.6 ± 1.2	1.00 ± 0.49
		0.44	3.3 ± 1.5	4.1 ± 0.9	1.9 ± 1.1
		0.52		1.7 ± 0.6	
		0.60		3.4 ± 1.0	
		0.68		0.74 ± 0.57	
		0.76		1.2 ± 0.72	
		0.84		0 ± 0.27	

Table V.1. (continued)

$p_\perp$ (GeV/c)	$p_\perp^2$ (GeV/c)	x_2	$\rho = Ed^3\sigma/dp^3$ (mb-c^3/GeV^2) P_{beam}=28.5 (GeV/c)	P_{beam}= 6.6 (GeV/c)	Ratio $\rho(28.5)/(\rho(6.6)$
0.4	0.16	0.01		8.78 ± 0.91	
		0.03		7.13 ± 0.74	
		0.05		7.36 ± 0.78	
		0.07		7.53 ± 0.81	
		0.09	10.5 ± 1.1	6.45 ± 0.75	1.63 ± 0.25
		0.11	10.1 ± 1.1	7.18 ± 0.84	1.41 ± 0.22
		0.13	8.2 ± 1.1	7.07 ± 0.79	1.16 ± 0.20
		0.15	7.2 ± 1.0	4.74 ± 0.66	1.52 ± 0.30
		0.17	7.6 ± 1.0	6.53 ± 0.84	1.16 ± 0.21
		0.19	6.2 ± 1.0	4.65 ± 0.76	1.33 ± 0.31
		0.25	5.3 ± 0.9	3.42 ± 0.28	1.55 ± 0.29
		0.35	3.57 ± 0.69	3.98 ± 0.38	0.90 ± 0.33
		0.45	1.82 ± 0.52	1.63 ± 0.26	1.17 ± 0.37
		0.55		1.10 ± 0.24	
		0.65		0.42 ± 0.17	
		0.75		0.24 ± 0.15	
		0.85		0.18 ± 0.14	
		0.95		0. ± 0.06	
0.8		0.05		0.63 ± 0.09	
		0.11		0.54 ± 0.09	
		0.17		0.60 ± 0.09	
		0.23		0.45 ± 0.08	
		0.29		0.38 ± 0.07	
		0.35		0.55 ± 0.10	
		0.41	0.44 ± 0.15	0.27 ± 0.08	1.63 ± 0.74
		0.47	0.31 ± 0.15	0.43 ± 0.10	0.72 ± 0.38
		0.53	0.32 ± 0.15	0.19 ± 0.07	1.7 ± 1.0
		0.59		0.24 ± 0.08	
		0.65		0.084 ± 0.052	
		0.71		0.059 ± 0.045	
		0.77		0. ± 0.020	

Table V.1 (continued)

a. From fig. 3c of ref. Si-1. The quantity that Sims et al. call $|x|$, is what we call $|x_2|$ (eqn.II.B.2) according to T. Hanlon (Ha-2).

There is some question as to whether or not Sims et al. have actually plotted ρ or a quantity which is 0.953 x ρ at their energies. This is because, according to their figure caption they actually plot.

$$\frac{1}{|\alpha-\beta|}\int_{\alpha}^{\beta}\frac{\pi}{\sqrt{s}/2}E^{*}\frac{d^{2}\sigma}{dp_{\perp}^{2}dx}dp_{\perp}^{2}$$

where α and β are the limits of $p_{\perp}^{2}$ for the bin in question. If the x in this equation is x_1 (eqn.II.B.1) the quantity which they plotted was indeed ρ, but if they meant x_2 for x here too, their results must be mutiplied by 1.049 before being compared with ours. Because this is uncertain (Ha-2), we just used the quantity that Sims et al. plotted, with no correction factors applied.

b. Only these errors are actually given in Si-1. All the other errors for the 28.5 GeV/c data are interpolated from these errors.

We do note, however, that for this same transverse momentum and for x_2 between 0.05 and 0.08, ρ increases by 50°/o when we go from Brookhaven to ISR energies (fig. 4).

Also, at higher transverse momentum, ρ does increase with increasing energy, even at ordinary accelerator energies. However, this increase is at a much slower rate than for the π^- spectra. A comparison of our data with that of Akerlof et al., for both signs of the pion charge, confirms this fact (figs. V.5 and IV.3).

We do not believe that we have reached true scaling in the central region for the reaction $pp \rightarrow \pi^+ +$ anything, since the ISR point is 50 % higher, and since we have not even reached scaling in the target fragmentation region.

The difference in behavior between the π^+ and π^- spectra is not so hard to understand. The final state for pp interactions has charge +2 and baryon number 2. If both outgoing baryons are protons there will be equally many negative and positive pions (we neglect the small amount of strange particle production). On the other hand, some of the baryons may be neutrons, in which case there will be an excess of positive pions. Obviously, the ratio $\sigma_{\pi^+}/\sigma_{\pi^-}$ decreases with increasing prong number. For 2-prongs only positive pions can be produced, whereas for 20-prongs an excess of one or two π^+'s can have little effect on $\sigma_{\pi^+}/\sigma_{\pi^-}$. Therefore this ratio, which is 2.67 at our energy, tends toward one at high energies. This explains why ρ increases more slowly for π^+'s than for π^-'s.

At acclerator energies ρ is not only not increasing rapidly, it is flat (near x = 0) or falling with energy, for the π^+. This may be because there is a large Δ^{++} contribution to the π^+ production cross section at our energy; probably about 1/3 of our π^+'s come from Δ^{++}. The Δ^{++} production-cross-section is probably decreasing with increasing energy. We base this assertion on the fact that the total cross section is observed to be almost energy independent above our energy. Therefore, neglecting baryon anti-baryon pairs, the baryon production cross section must also be flat. Because more and more baryon resonance channels open up as the energy increases, it is likely that the fraction of baryons produced from the decay of the Δ^{++} decreases, and therefore the Δ^{++} cross section decreases.

The Δ^{++}'s are produced fairly peripherally. This means that the π^+'s resulting from Δ^{++} decay will be in the proton fragmentation region. Because Δ^{++} production probably decreases with increasing energy, the π^+'s resulting from its decay also decrease. For this reason the structure function should decrease with increasing energy, in the fragmentation region, as we observe.

It turns out that at our fairly low energy, many of the π^+'s from Δ^{++} decay reach the central region. This implies, for the reason previously stated, that ρ decreases with increasing energy in this region also. However, at higher energies the contribution of the Δ^{++} to the central region becomes less important, and ρ is expected to increase because of the increasing pion multiplicity. This is consistant with our observation of a flat region at acclerator energies, followed by a rising ρ from acclerator to ISR energies.

Perhaps it is interesting to note that near $x = 0$, ρ increases slowly with energy for pions produced in the non-exotic reactions $\pi^+ p \to \pi^+ +$ anything, $\pi^- p \to \pi^- +$ anything and $p \to \pi^- +$ anything (Ga-1; Be-3; Cr-1; Sh-1; Mo-1). We emphasize that these reactions are similar only in that, near $\underline{x} = 0$, ρ increases slowly with energy at accelerator energies, and in that for the proton breakup region (slow or backward lab. momenta), the lower energy differential cross section exceeds the higher energy cross section: the absolute values of the normalized structure functions are quite different for these different reactions at accelerator energies (fig. IV.6).

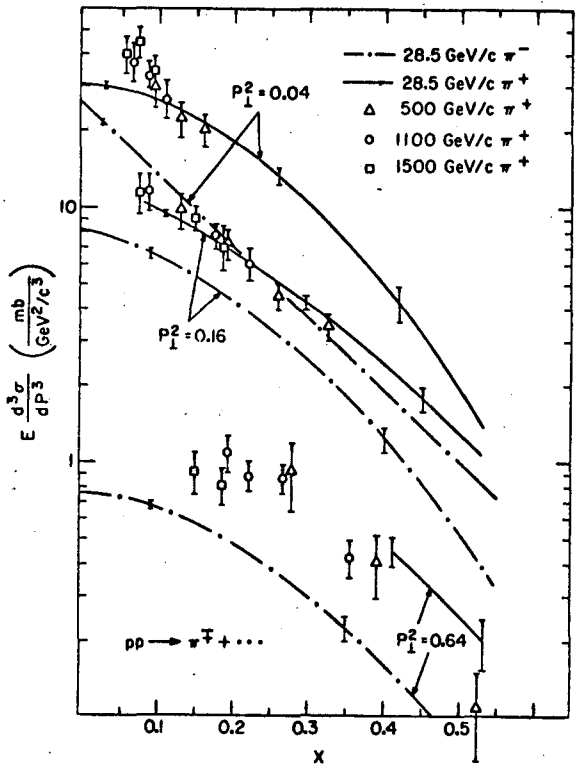

Fig. V.4. "Invariant single-particle inclusive spectra (p + p $\rightarrow \pi^{\pm}$ + ...) plotted as a function of x at the indicated $p_{\perp}^2$-values from ISR data" (ref. Ra-2) " and from 28.5 GeV/c bubble chamber data." [Figure and caption copied from ref. Pa-3. The variable x is what we call x_2.]

N.B. The data point is at the center of the triangle for this plot.

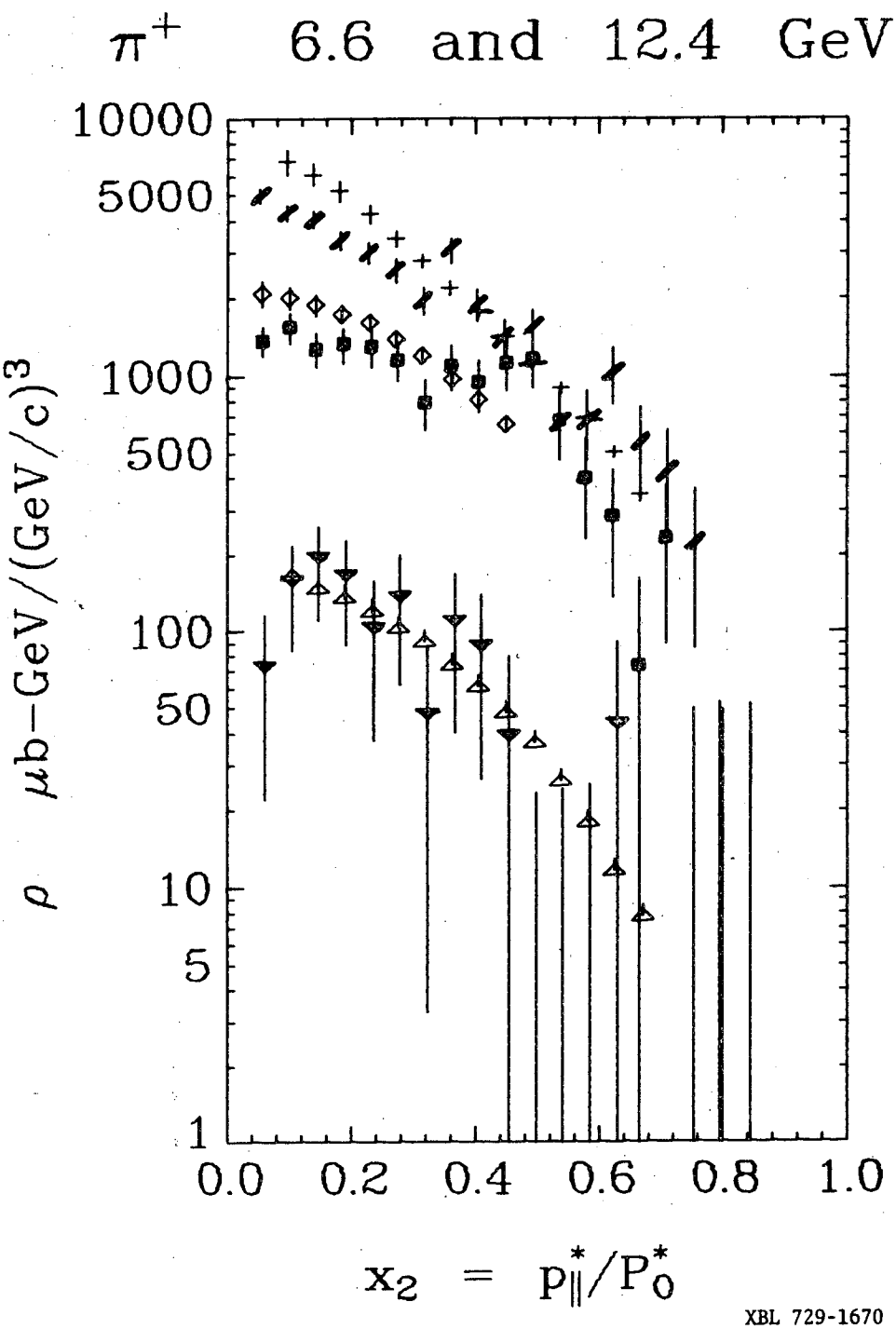

Fig. V.5 A comparison of this experiment (6.6 GeV/c) with Akerlof et al. (12.4 GeV/c - ref. Ak-1) for $pp \rightarrow \pi^+ +$ anything; ρ vs. x_2 for 3 values of $p_\perp^2$: 0.22(◢ & —), 0.43(■ & ◇), and 1.06 (▼ & △) $(GeV/c)^2$. The first symbol of each pair above is for our data, and the second is for Akerlof's. The x_2 bin width of our points is equal to their separation, and the $p_\perp^2$ bin width is 0.1 $(GeV/c)^2$ for the 2 smallest $p_\perp^2$ values, and 0.2 $(GeV/c)^2$ for $p_\perp^2$ = 1.06 $(GeV/c)^2$.

Please note: the data point is at the apex of the triangle, viz. ◬ and ▽.

C. Comparison with Higher Energies for Proton Production

Proton-proton elastic scattering has been extensively studied (see pp 25 et seq. of ref. Be-13 for a data compilation and list of references). These studies show that the differential cross section $d\sigma/dt$ is almost energy independent when plotted against the appropiate variable. In fact, Krisch showed that $d\sigma^+/dt$ depends only on $\beta^* p_\perp$ for pp reactions from 5 to 32 GeV/c, where β^* is the C.M. proton velocity (Kr-1). [The term $d\sigma^+/dt$ is introduced by Krisch to take account of the symmetry of the initial state in pp interactions. It is defined by

$$(d\sigma/dt)_{observed} = (d\sigma^+/dt)_{forward} + (d\sigma^+/dt)_{backward}.$$

Clearly it is only near 90°, where the forward and backward cross-sections are of comparable magnitude, that $(d\sigma/dt)_{observed}$ and $d\sigma^+/dt$ are very different.]

Consider the plot of $d\sigma^+/dt$ vs. $\beta^{*2}p_\perp^2$. It is energy independent and decreases rapidly with $\beta^{*2}p_\perp^2$. Now suppose that we want to plot $d\sigma^+/dt$ against $p_\perp^2$ instead of $\beta^{*2}p_\perp^2$. Each point $\beta^{*2}p_\perp^2 = a_i$ is mapped onto a point $p_\perp^2 = a_i/\beta^{*2}$, i.e. the entire curve is stretched by a factor $1/\beta^{*2}$ ($\beta^{*2} < 1$). The larger β^* is, the smaller that the stretching will be. Alternatively, we may first look at $d\sigma^+/dt$ vs. $p_\perp^2$ for small β^* (very stretched). As β^* increases, the curve will shrink (become less stretched). The effect is illustrated below.

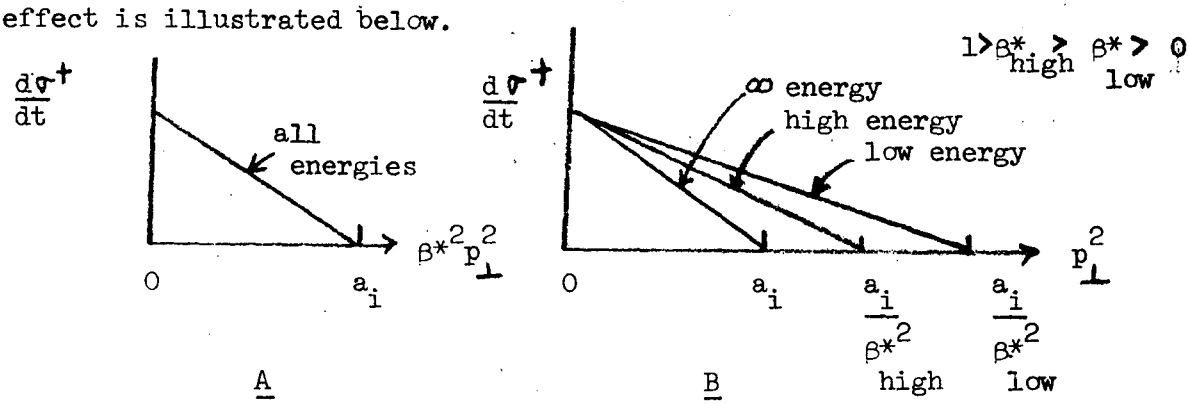

We emphasize that if $d\sigma^+/dt$ vs. $\beta^{*2}p_\perp^2$ is energy independent (which it appears to be) then $d\sigma^+/dt$ vs. $p_\perp^2$ must shrink. The percent of shrinkage is given by

$$\delta = 100 \times \left\{ \frac{1/\beta^{*2}_{low} - 1/\beta^{*2}_{high}}{1/\beta^{*2}_{low}} \right\} = 100 \times \left\{ 1 - (\beta^{*2}_{low}/\beta^{*2}_{high}) \right\}.$$

Therefore the percent shrinkage from 6.6 GeV/c to infinite energies is

$$\delta = 100 \times (1 - 0.87^2) = 26\ \%.$$

Because so much work has already been done on elastic scattering, and because of the difficulty in determining our elastic cross-section (see section III.D), we feel that there is no point in comparing our differential elastic cross sections with higher energies. Therefore, in comparing with higher energies, we omit the region of high x where elastic scattering is dominant.

Allaby et al. have presented a graph of ρ vs. x_2 for proton production in the region 6.6 to 24 GeV/c. They obtain the 6.6 data points, for $p_\perp = 0.65$ GeV/c only, from our earlier paper (Ab-2). We add to this graph our data points at $p_\perp = 0.15$ and 0.35 GeV/c. [We also replot our $p_\perp = 0.65$ GeV/c data points using the same bins that we use for the lower two momenta, for convenience.] The result is figure 6. For most points error bars are not shown because the point-to-point error is less than the size of the point. There is also a $\pm 5\ \%$ normalization error for our data, and systematic errors of up to $\pm 15\ \%$ for the other experiments. These errors are not shown on the plot.

It is evident that for the lowest two momentum intervals of fig. 6b, our data exceed the higher energy data. For $x_2 > 0.2$, we exceed

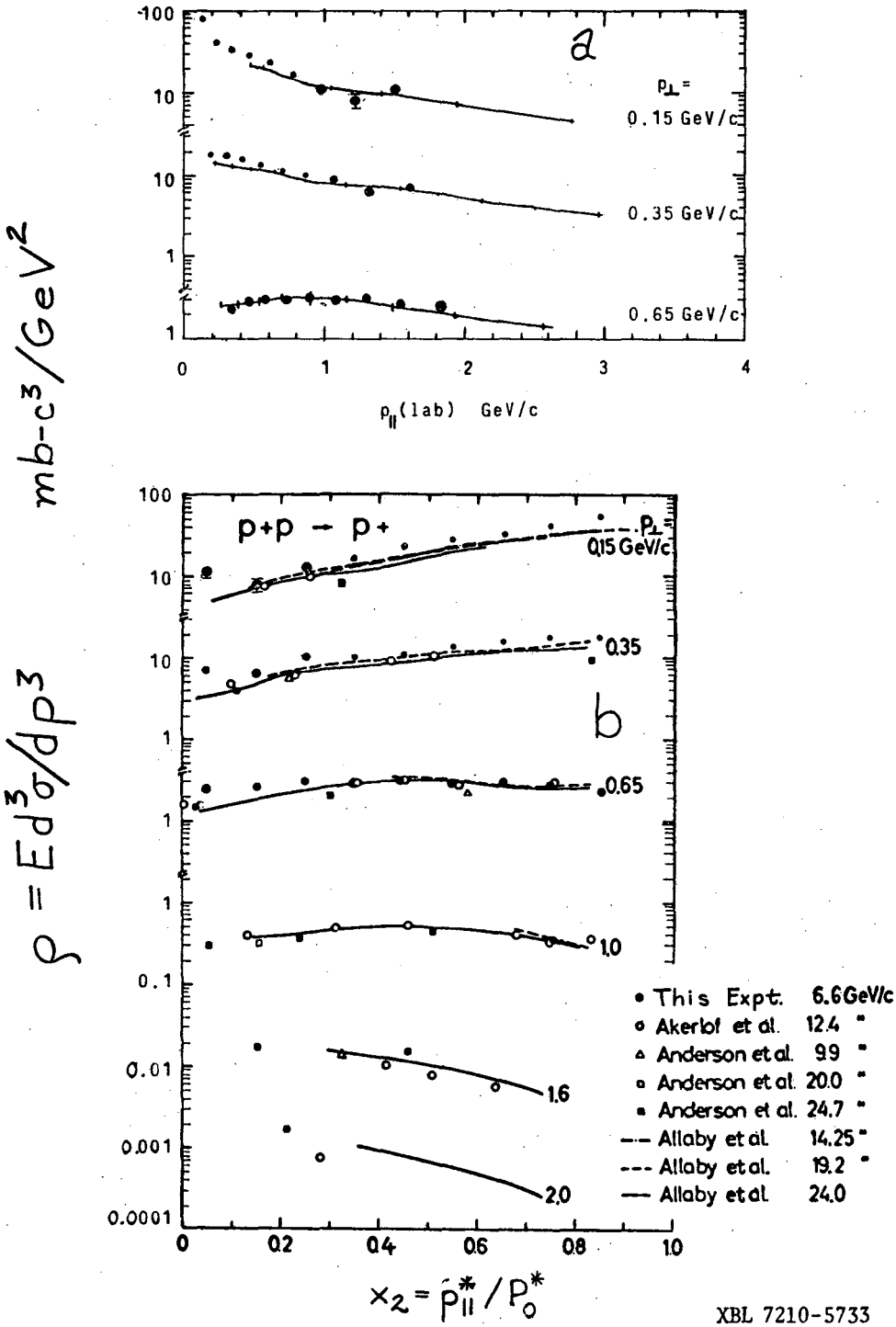

Fig. V.6 A comparison of this experiment (6.6 GeV/c) with higher acclerator energies (from fig. 9f of ref. Al-4, also presented on pp 239 of ref. La-1) for pp → p + anything. For this expt. $\Delta p_\perp = \pm 0.05$ GeV/c. For most points error bars are not shown because the error is smaller than the size of the point.

a. (upper fig.) ρ vs. $p_{||}$(lab)

b. (lower fig.) ρ vs. x_2

Allaby's 24.0 GeV/c data by 50 $^{0}/0$ for $p_\perp$ = 0.15 GeV/c, and by 30 $^{0}/0$ for $p_\perp$ = 0.35 GeV/c. For $p_\perp$ = 0.65 GeV/c we are in agreement with Allaby.

For $x_2 < 0.1$ we exceed the higher energy data by an even greater amount: the value of ρ at 6.6 GeV/c is 2 to $2\frac{1}{2}$ times as large as at 24.0 GeV/c.

That $\rho(6.6)/\rho(24)$ decreases with increasing $p_\perp$ is not at all surprising. This is just a consequence of the fact that $\langle p_\perp \rangle_{av}$ is still increasing with energy. We have noted similar behavior for the π^+ and π^-.

The decrease of ρ with energy at accelerator energies is also expected. There are very few baryon anti-baryon pairs produced at these energies. Therefore, unless there is an increase in the proton to neutron ratio, the fact that the total pp cross section is almost energy independent above 6.6 GeV/c means that the structure function must decrease with energy. This can readily be seen by considering the behavior of B(y,s) with increasing energy, where

$$B(y,s) = \int_0^\infty \rho(y,p_\perp,s)dp_\perp^2 = (c/\pi)d\sigma/dy \qquad \text{II.C.10 and 13}$$

It is well known that if $\rho(x,p_\perp,s)$ is energy independent above some value of s (scaling has occurred), increasing the energy only increases the length of the central plateau of a B vs. y plot (y is the rapidity defined by eqn.s II.B.7). Now y^*_{max} increases from 1.32 at 6.6 GeV/c to 1.97 at 24 GeV/c, a 48 $^{0}/0$ increase. This means that if B(y,s) vs. y had a rectangular shape at 6.6 GeV/c, the total number of protons produced must increase by 48 $^{0}/0$ if scaling has occurred. Because B actually is larger at large y* (see fig. 10c) even for inelastic events, the

increase will be somewhat less than this. The effect is illustrated in fig. 7.

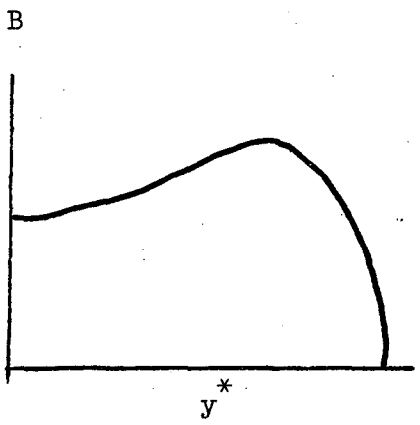

Fig. V.7a Inelastic rapidity distribution at 6.6 GeV/c

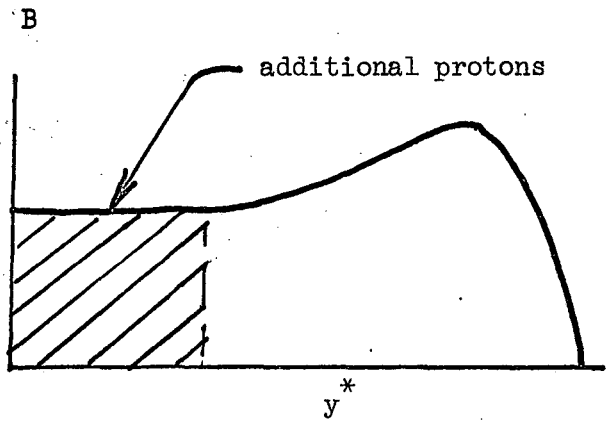

Fig. V.7b Inelastic rapidity distribution at 24 GeV/c assuming that scaling has already set in at 6.6 GeV/c.

However, as previously mentioned, the total cross section does not increase with energy (and the inelastic cross section increases very slowly, if at all). Therefore the structure function must decrease with energy. Since the structure function at small $p_\perp$ contributes most strongly to B, it must therefore decrease by about 48 $^0/0$ on the average. This is indeed what we observe.

Furthermore, as we increase the beam momentum, the "leading proton" makes a smaller and smaller contribution near x = 0. Since baryon anti-baryon pair production is not important even near x = 0 at 24 GeV/c, the structure function should fall more rapidly with increasing energy near x = 0 than elsewhere, as we observe.

Our high point at $x_2 = 0.85$ and $p_\perp = 0.15$ may be due to Δ^{++} decay, as explained in the previous section. For a peripheral Δ^{++}, kinematics requires the proton to be fast and forward too.

The better agreement in the lab. frame for small $|x|$ is probably fortuitous (fig. 6a).

We compare our results with the ISR results of Ratner et al. (Ra-2). We observe a similar effect with respect to the ISR points (fig. 8). There appears to be a 60 ^{0}/0 decrease from 6.6 GeV/c to ISR energies (1100 GeV) for $p_\perp = 0.4$ GeV/c, greater than the approximately 30 ^{0}/0 decrease from 6.6 to Allaby et al.'s 24.0 GeV/c data, i.e. ρ seems to still be decreasing from 24 GeV/c to ISR energies.

According to J. C. Sens (Se-1), the ratio $\bar{p}/p$ is 0.55 ± 0.10 at ISR energies and $x = 0$. Recently the British-Scandinavian Collaboration has reported the ratio $p/\bar{p}$ integrated over the outgoing proton momentum range $0.3 < p < 1.2$ GeV/c (in the ISR lab., ie. almost in the C.M.), for 5 C.M. angles from 90° to 29° for 1500 GeV equivalent incident energy. (table 4 of ref. A1-5). If we average their reported values, we obtain $p/\bar{p} = 1.86 \pm 0.11$ (or $\bar{p}/p = 0.53 \pm 0.03$). It therefore appears that scaling has not been reached even at ISR energies. Whether ρ will continue to fall at these energies depends on whether or not the contribution from "leading protons" is falling faster than the contribution from baryon anti-baryon pairs is increasing.

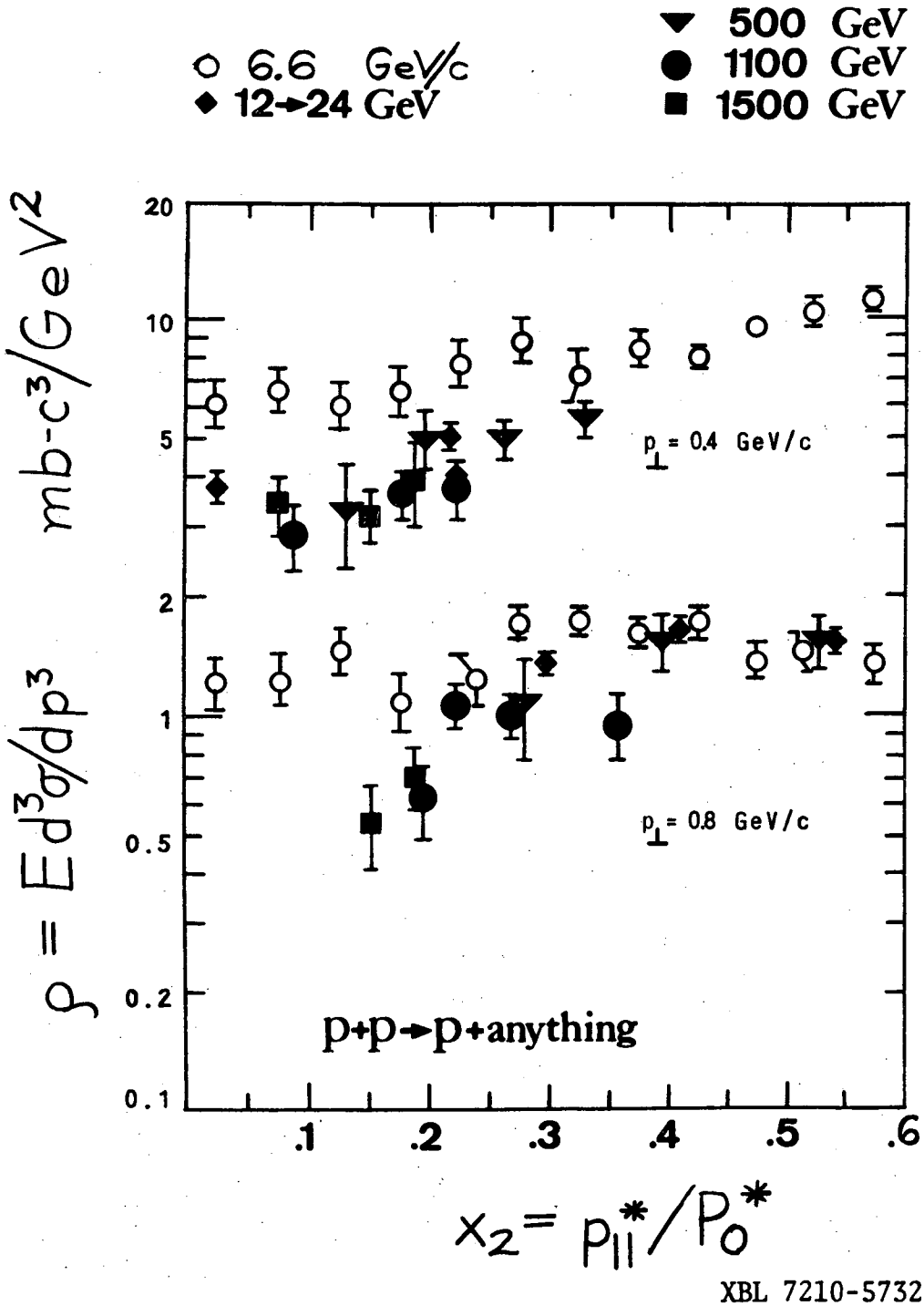

XBL 7210-5732

Fig. V.8 A comparison of this experiment (6.6 GeV/c) with ISR energies and higher acclerator energies (from fig. 1 of ref. Ra-2, also presented as fig. 11a of ref. Al-4 and pp 301 of ref. La-1) for pp → p + anything: ρ vs. x_2 for $p_\perp$ = 0.4 and 0.8 GeV/c. ($p_\perp$ = 0.35 to 0.45 and 0.7 to 0.9 GeV/c for the 6.6 GeV/c data). [The 12 to 24 GeV/c points were calculated by Ratner et al. by interpolating previously published experimental results to these values of $p_\perp$.]

D. One Dimensional Distributions for this Experiment

We plot for the positive outgoing particles (the π^+ and proton), the same quantities that we plotted for the π^- in section IV.D.1, i.e. various longitudinal distributions for the elastic, 2-prong inelastic, 4-prong, 6-prong and combined samples (figs. 9 and 10). We notice the well known clustering at $p^*_{||} \approx 0$ for those events with a large number of particles in the final state. We also notice that whereas the π distributions fall off fairly rapidly with increasing x_2 (figs. IV.8a and V.9a), the proton distribution increases with increasing x_2, even when we exclude the elastic events (fig. 10a).

It should be pointed out that plots of $F(x_2)$ vs. x_2 (see eqn. II.C.8) are rather different than plots of the ordinary cross section, $d\sigma/dx_2$ vs. x_2 (not shown). Not only does the energy factor multiplying the ordinary cross section (eqn. II.C.8) make the distribution fall more slowly with increasing x_2, but it greatly changes the behavior of different mass distributions near $p^*_{||} = 0$. For example, even though there are twice as many π^-'s as protons near $p^*_{||} = 0$, the structure function for π^-'s is only half that for protons in this region. (table V.2). Clearly, this is because near $p^*_{||} = 0$, the proton rest mass is a major contributor to the proton energy, so that it has a much higher value of energy than does the lighter pion.

We note that the total π^+ distribution decreases less rapidly than does the π^- distribution, at large x_2. Just the opposite is true of the pions from 4-prongs alone: the π^+ distribution decreases more rapidly for them. The difference is due to the fact that the π^+'s are also produced in 2-prongs, whereas π^-'s are not. As previously mentioned, for fewer prongs there is a less rapid decrease of ρ with x_2.

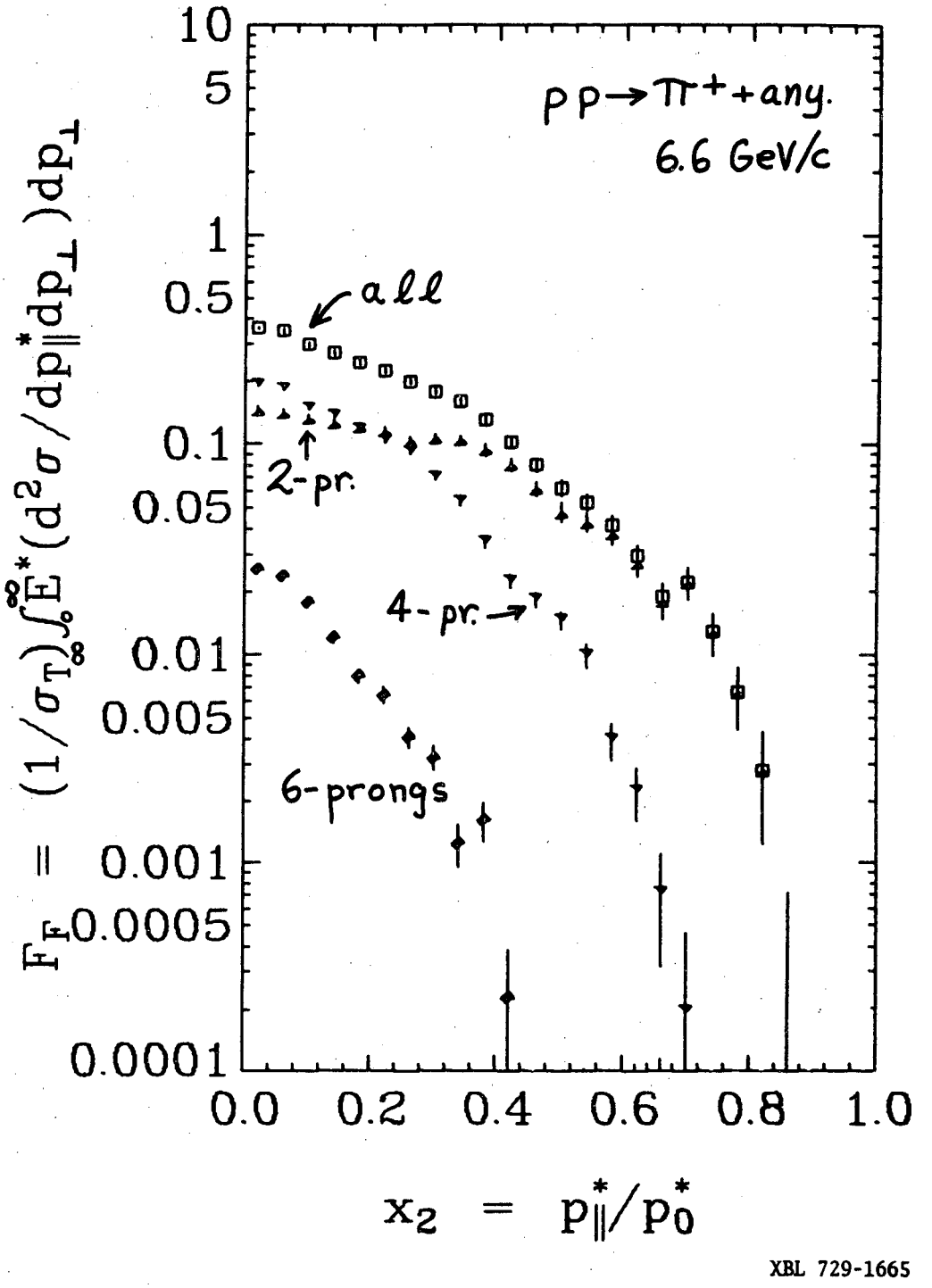

XBL 729-1665

Fig. V.9 Longitudinal and transverse distributions for π^+'s from $pp \rightarrow \pi^+$ + anything at 6.6 GeV/c. The upper curve of each plot (□) is the combined 2, 4, and 6-prong samples, whereas the lower three curves on each plot are the 2(▲), 4(▽), and 6-prong(◆) samples respectively. The error bars represent statistical errors only. N.B. The data point is at the apex of the 2 and 4-prong symbols: →▲ and ▽←. (see also fig. IV.8 and its caption)

a. F_F vs. x_2 (using $\sigma_{T\infty}$ = 39.5 mb).

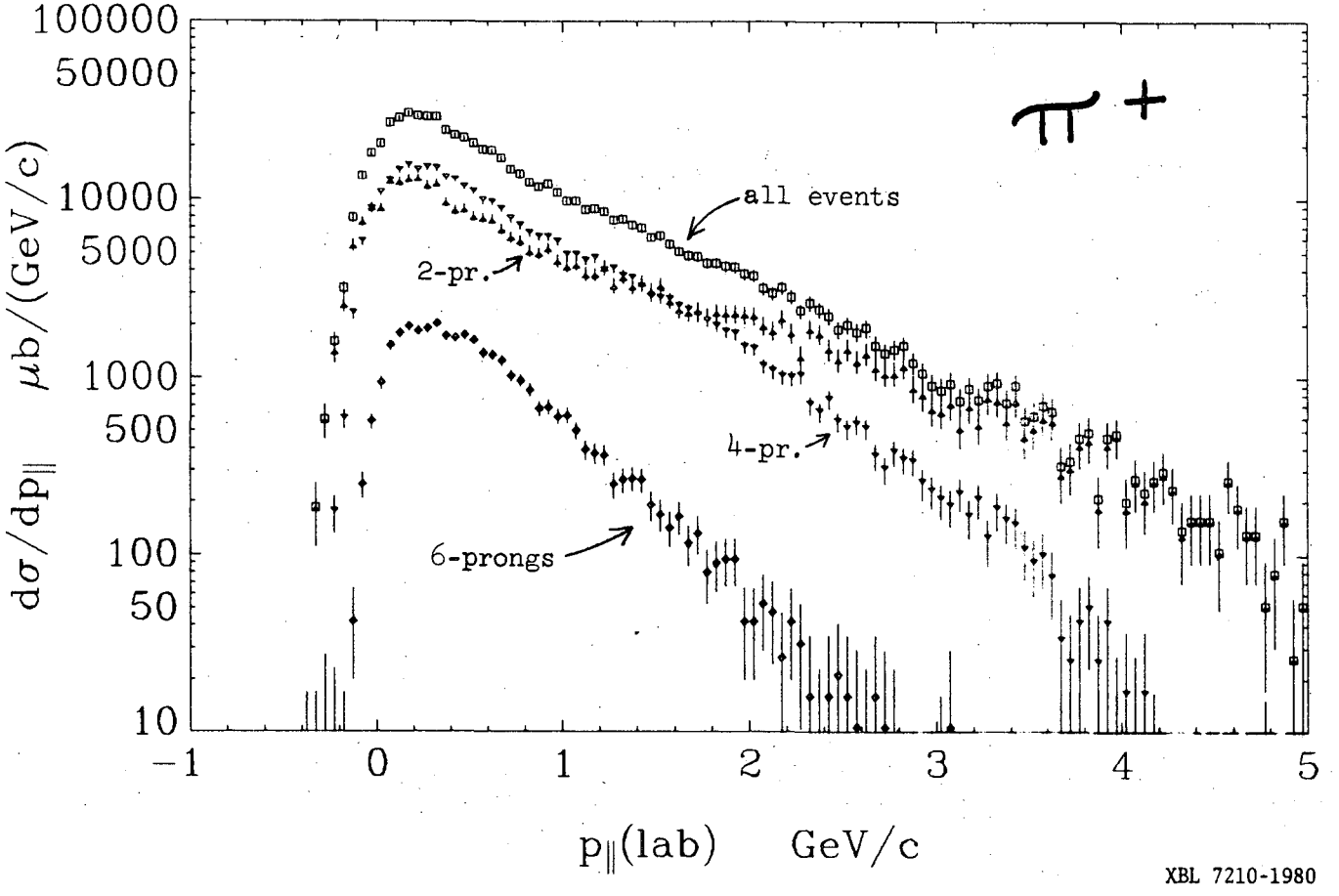

Fig. V.9 Longitudinal and transverse distributions for π^+'s from $pp \rightarrow \pi^+ +$ anything at 6.6 GeV/c ...

b. $d\sigma/dp_{\parallel}$ vs. $p_{\parallel}$(lab)

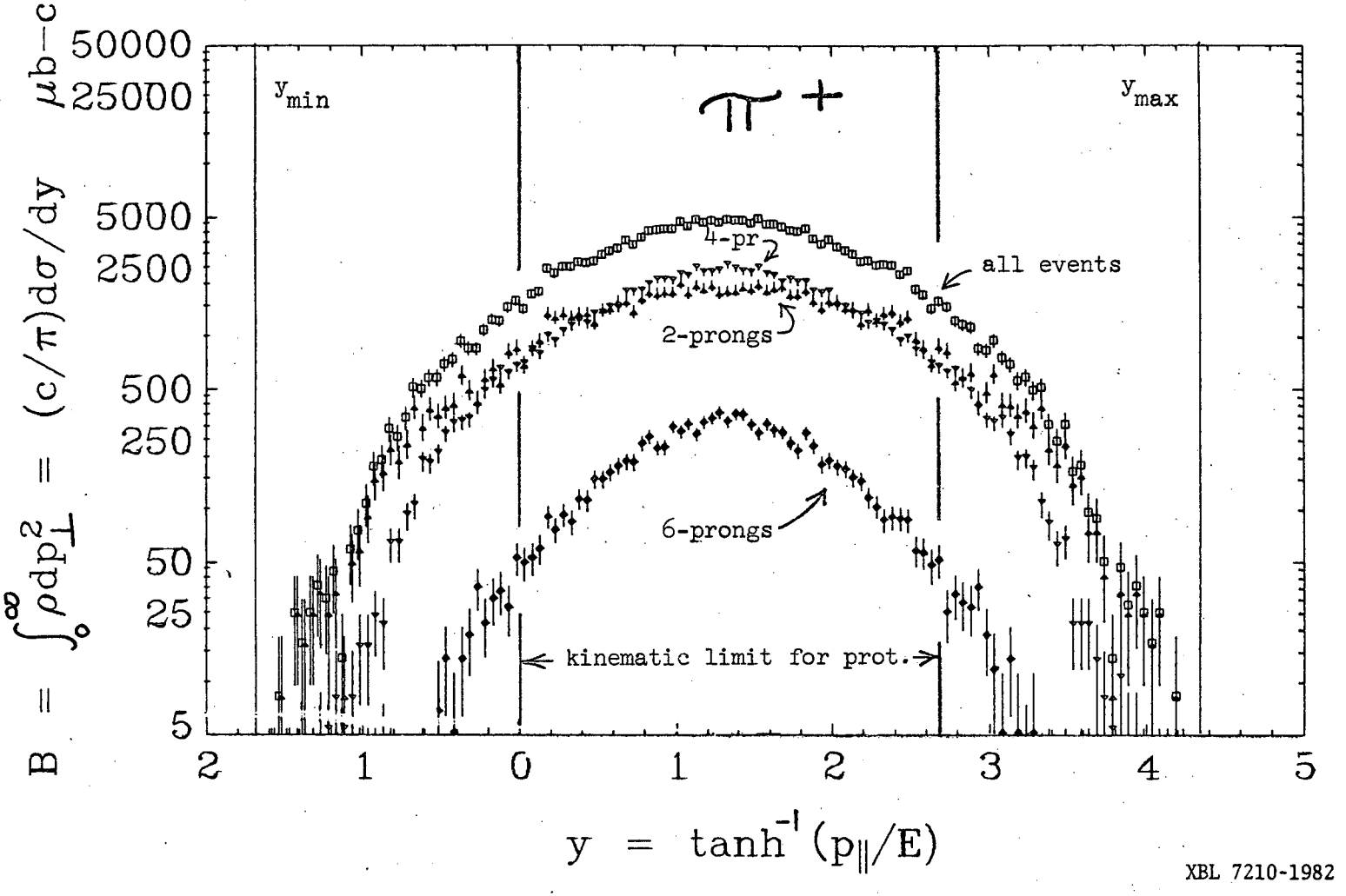

Fig. V.9 Longitudinal and transverse distributions for π^+'s from $pp \rightarrow \pi^+ +$ anything at 6.6 GeV/c ...

c. B(y,s) vs. y.

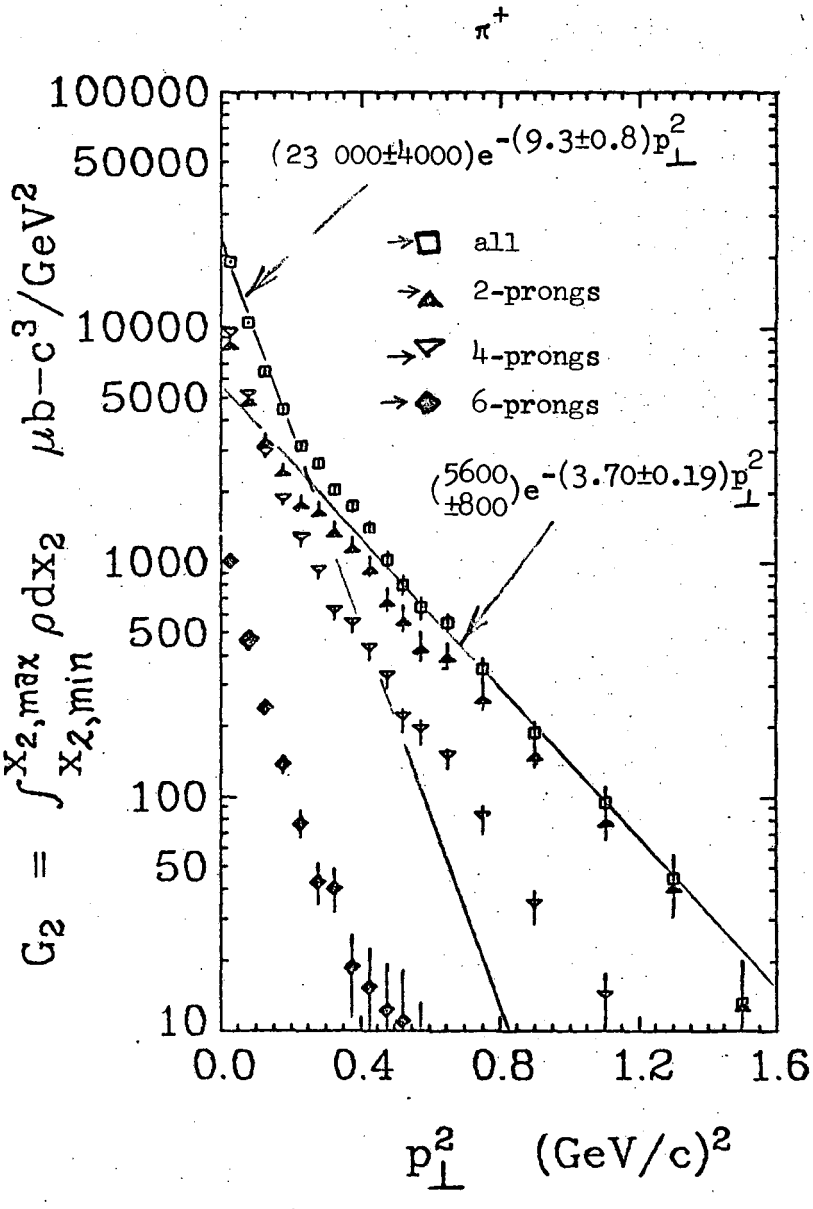

Fig. V.9 Longitudinal and transverse distributions for π^+'s from pp π^+ + anything at 6.6 GeV/c ...

d. $G_2(p_\perp, s)$ vs. $p_\perp^2$. The two straight lines are fit to the "all-prong" data points by eye.

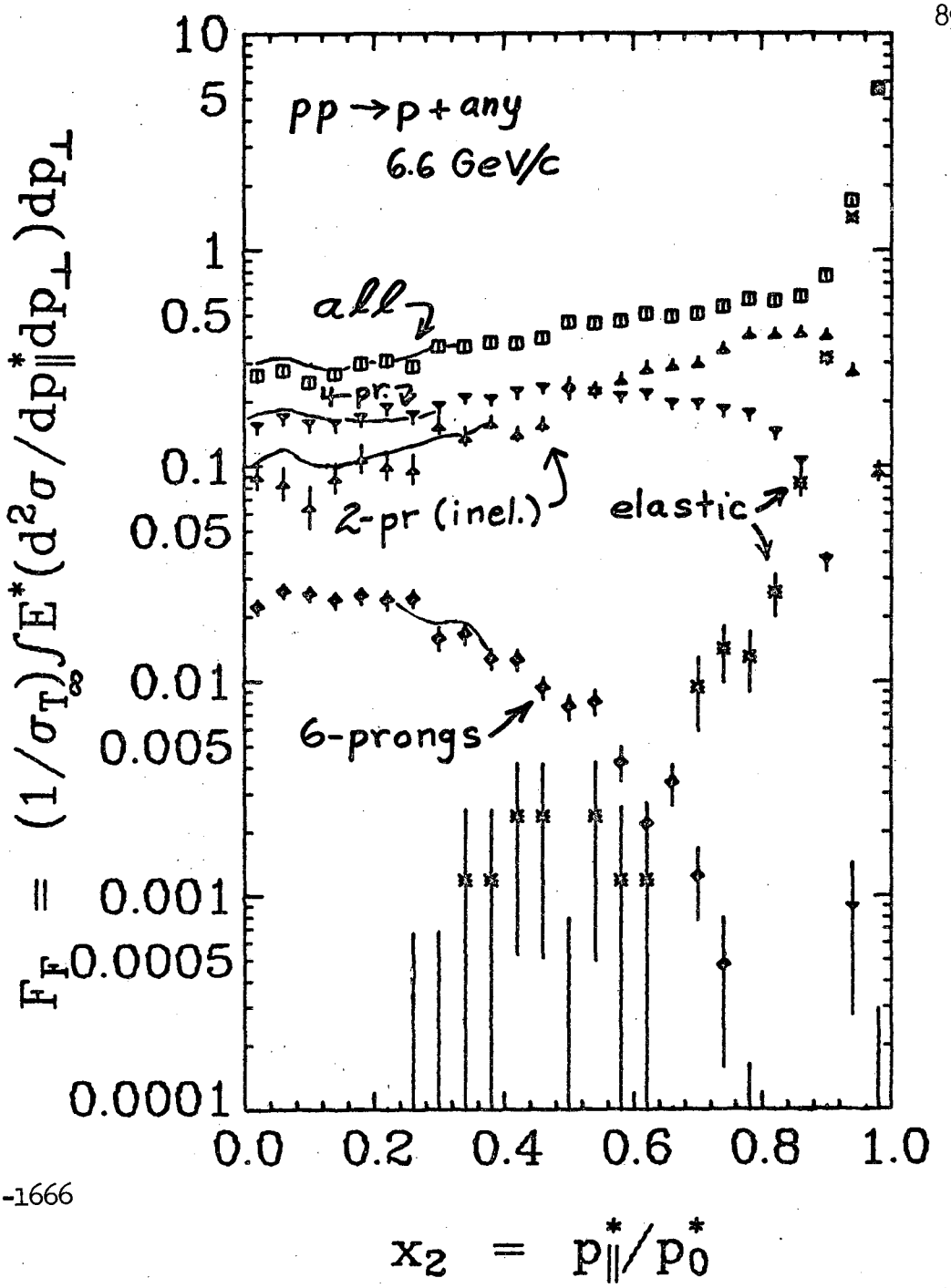

XBL 729-1666

Fig. V.10 Longitudinal and transverse distributions for protons from pp → p + anything at 6.6 GeV/c. The upper curve of each plot (□) is the combined elastic, 2-prong inelastic, 4-prong, and 6-prong sample, whereas the lower 4 curves are each of these 4 samples (*, ▲, ▽, ◇). The error bars represent statistical errors only. N.B. the data point is at the apex of the 2-prong and 4-prong symbols: ▲ and ▽.

a. F_F vs. x_2 [(1) The solid curves are explained in the text.
(2) The elastic points are normalized to 10.16 mb. and probably should be multiplied by 1.160 in order to agree with Foley's value of the elastic cross-section, 11.79 mb. (see section III.D). This will also increase F_F for "all-prongs" near $x_2 = 1$.]

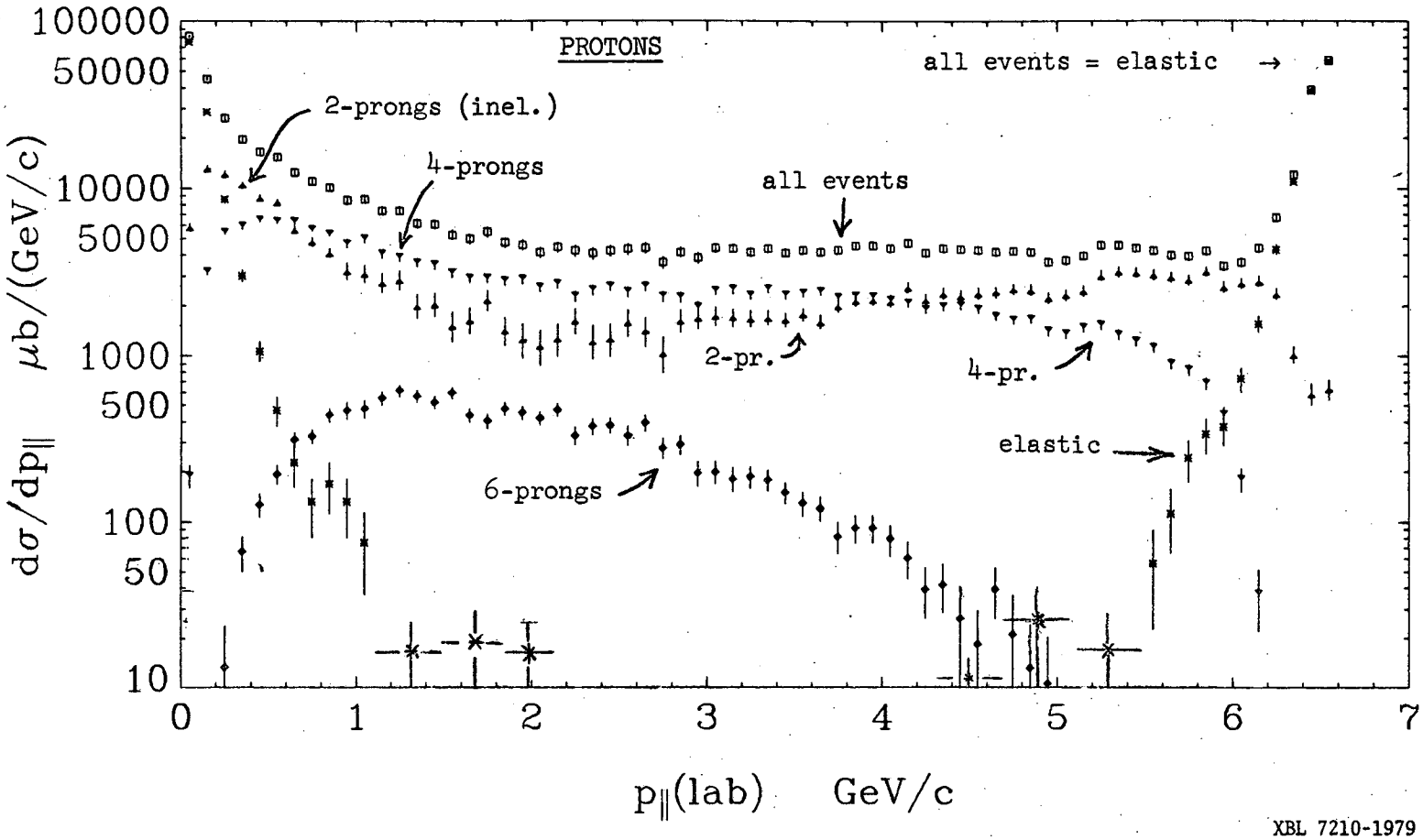

Fig. V.10 Longitudinal and transverse distributions for protons from pp → p + anything at 6.6 GeV/c ...

b. $d\sigma/dp_{\perp}$ vs. $p_{\parallel}$(lab) [The elastic events are normalized to Foley's value of 11.79 mb (see section III.D)]

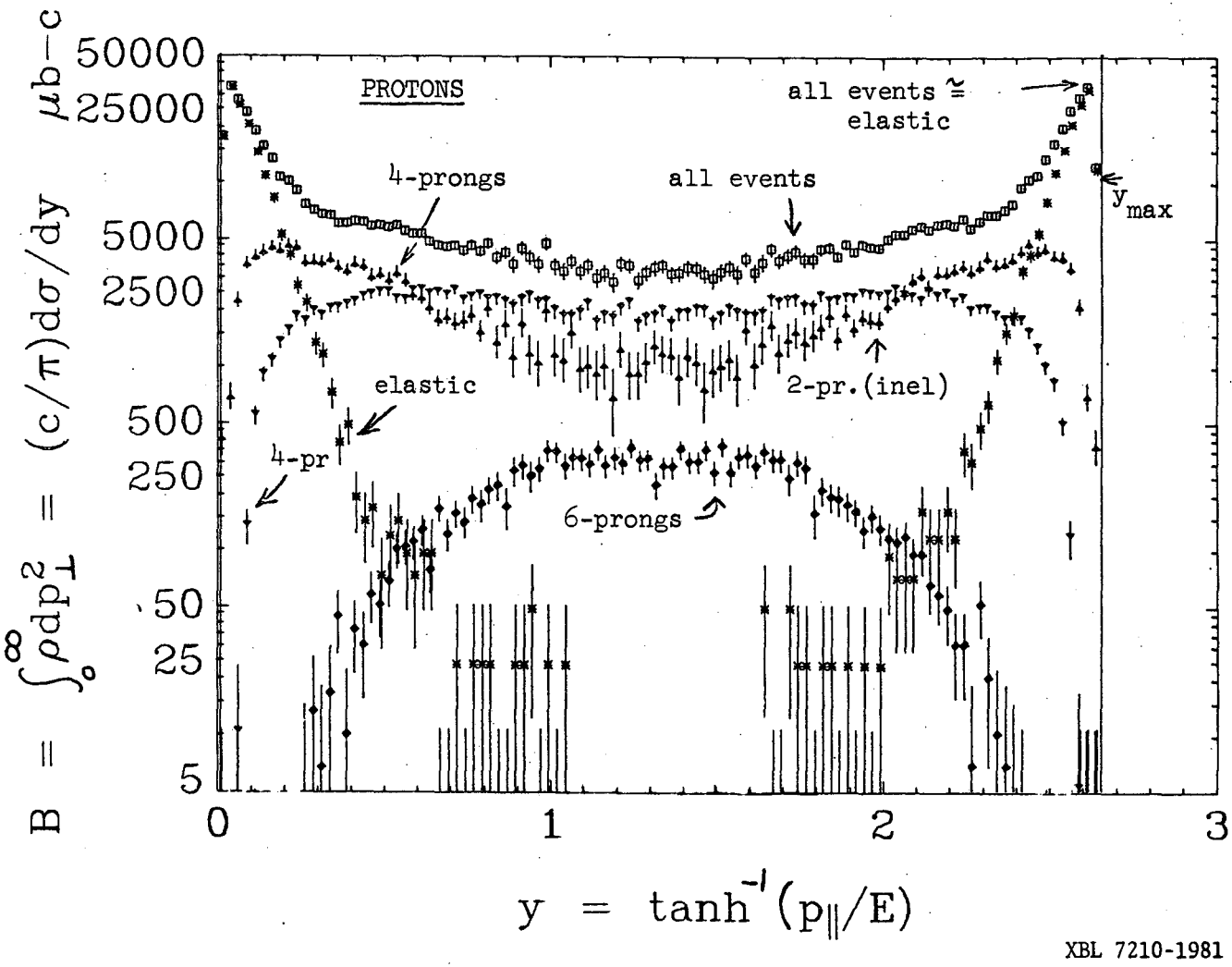

Fig. V.10 Longitudinal and transverse distributions for protons from pp → p + anything at 6.6 GeV/c ...

c. B(y,s) vs. y [The elastic events are normalized to Foley's value of 11.79 mb (see section III.D of text).]

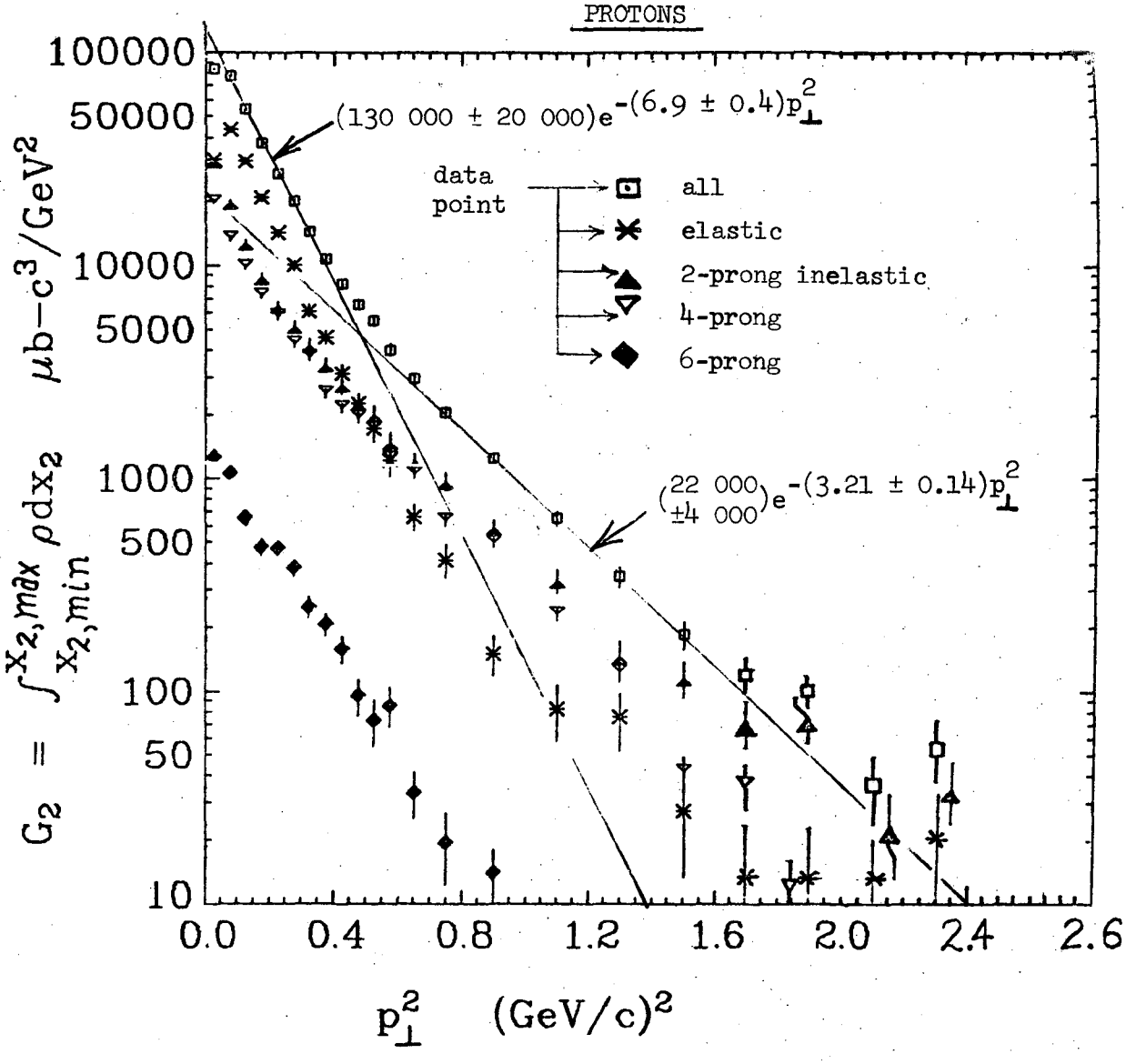

Fig. V.10 Longitudinal and transverse distributions for protons from $pp \rightarrow p$ + anything at 6.6 GeV/c ...

d. $G_2(p_\perp, s)$ vs $p_\perp^2$. The two straight lines are fit to the "all-prong" data points by eye.

[The elastic events are normalized to Foley's value of 11.79 mb (see section III.D of the text).]

Table V.2. Comparison of pion and proton distributions at $x = 0$.

	Ratios	
	π^+/proton	π^-/proton
Particle ratios[a]	5.5	2.1
structure function ratios[b]	1.4	0.53

a. from plots of $d\sigma/dx_2$ (not shown)

b. from figs. IV.8a and V.9a and 10a. We tabulate $F(\pi)/F(\text{proton})$ for $x = 0$, where F is defined by equation II.C.8.

The completely different nature of the proton and π^+ distributions is also evident in plots of the laboratory differential cross - section vs $p_{||}$ (lab) (fig. 9b and 10b) and the integrated structure function vs. the laboratory rapidity, y (fig. 9c and 10c). Only the protons have appreciable cross sections at large laboratory momentum.

The proton rapidity plot is plotted against an expanded rapidity scale. This is done because the kinematic limit in rapidity for the heavy proton is less than for the light pion. We observe that most of the pions lie within the kinematic limits for protons.

Finally, we plot the transverse distributions $G_2(p_\perp,s)$ vs. $p_\perp^2$, where G_2 is given by eqn. II.C.14 (figs. 9d and 10d). We draw two exponentials through the "all-prong" data points by eye, just as we did for the π^- distribution (section IV.D, page 60). The π^+ data are represented fairly well by these two curves, with the "break-point" occurring at about $p_\perp^2 = 0.25$ (GeV/c)^2. In fitting the proton data, we ignore the two bins for which $p_\perp^2 < 0.1$ (GeV/c)^2. Backward elastic protons in this region have laboratory momentum not much larger than $p_\perp$, and are therefore often not seen (see section III.D). Two curves, with a "break-point" at about $p_\perp^2 = 0.47$ (GeV/c)^2, represent the remaining points fairly well out to about $p_\perp^2 = 1.8$ (GeV/c)^2. It then appears that another even-less-steep exponential is needed.

If we compare all the transverse distributions (figs. IV.8d, V.9d, and V.10d), it is evident that the π^+ has a gentler slope than the π^- at large $p_\perp^2$, and that the proton has a gentler slope than either pion for all $p_\perp^2$. The fact that protons have a gentler slope than pions is, of course, well known. This same behavior can be seen in a table of the average transverse momentum (table 3). Also, we note that $\langle p_\perp \rangle_{av}$ is smaller for the π^+ than for the π^- for both 4 and 6-prongs. However the large value of $\langle p_\perp \rangle_{av}$ for 2-prongs (which only contribute to the π^+ sample, of course) more than compensates for this. The result is that for "all-prongs" $\langle p_\perp \rangle_{av}$ is larger for π^+ than for π^-.

One last remark: the solid curves on fig. 10a are the results that we obtain if we do not use the subtraction method to calculate the proton spectra (see section III.E), but instead assume that all

Table V.3 Average transverse momentum for $pp \rightarrow X$ + anything for an incident momentum of 6.6 GeV/c, where X = π^-, π^+, or p.[a]

	$\langle p_\perp \rangle_{av}$ (MeV/c)		
topology	π^-	π^+	proton
all events	272 ± 1	288 ± 1	378 ± 1[b]
elastic	------	------	371 ± 2[b]
2-prong (inel.)	-----	325 ± 3	387 ± 2
4-prong	278 ± 1	259 ± 1	375 ± 1
6-prong	228 ± 2	217 ± 2	343 ± 3

a. Please Note: The errors quoted in this table are statistical errors only, and are useful only for comparing different values in this table with each other. To compare these results with other experiments an estimated measurement uncertainty of about ±4 MeV/c must be added to this error.

b. $\langle p_\perp \rangle_{av}$ is too large because elastic events with small $p_\perp$ (and therefore small $p_{||}$(lab) half the time) were lost - see section III.D.

the tracks called protons on the basis of bubble density and kinematic fits, and for which $p^*_{||} \lesssim 0$, are indeed protons. If we do not use the subtraction method, our results will be about 30 °/o too high for the 2-prongs and 15 °/o too high for the 4-prongs near $x = 0$. This is because there are many π^+s in this region of laboratory momentum, so that if one cannot cleanly separate these two particles, there will be serious π^+ contamination in the proton sample.

Finally, we mention that some proton distributions for this experiment have been presented in an earlier paper (Ab-1). While we do not plot these distributions again in this paper we should point out that if an error in the axes labeling is corrected in this other paper ($d\sigma/dp_{\parallel}$ should read $d\sigma/d|p_{\parallel}|$), the distributions plotted there are 10 to 15 °/o higher for small $\underline{x}$ than those we calculate using the subtraction procedure employed in this paper, even though the 6-prongs were not included in that earlier paper. However, in this other paper, the method of subtracted distributions was not used, except for some missing mass reactions, and both forward and backward protons were included, at least for some final states.

E. Two Dimensional Distributions for this Experiment

For both outgoing π^+'s and protons, we now plot ρ vs. x_2, for five equal intervals in $p_\perp$ from 0 to 1 GeV/c (figs. 11 and 12).

Although the structure function is much larger for π^+ than for π^-, the shapes of both pion distributions seem somewhat similar (figs. V.11 and IV.11a): there appears to be a somewhat more pronounced shoulder for the π^+ events at $x_2 = 0.2$ and $p_\perp = 0.1$ GeV/c. For both plots, ρ falls off less steeply with $\underline{x}$ for higher transverse momentum. On the other hand, the proton distribution rises with $\underline{x}$ for low $\underline{p_\perp}$, and is fairly flat for large $\underline{p_\perp}$.

We can summarize the above paragraph by saying that the structure function cannot be factorized into functions of longitudinal and transverse momentum at 6.6 GeV/c.

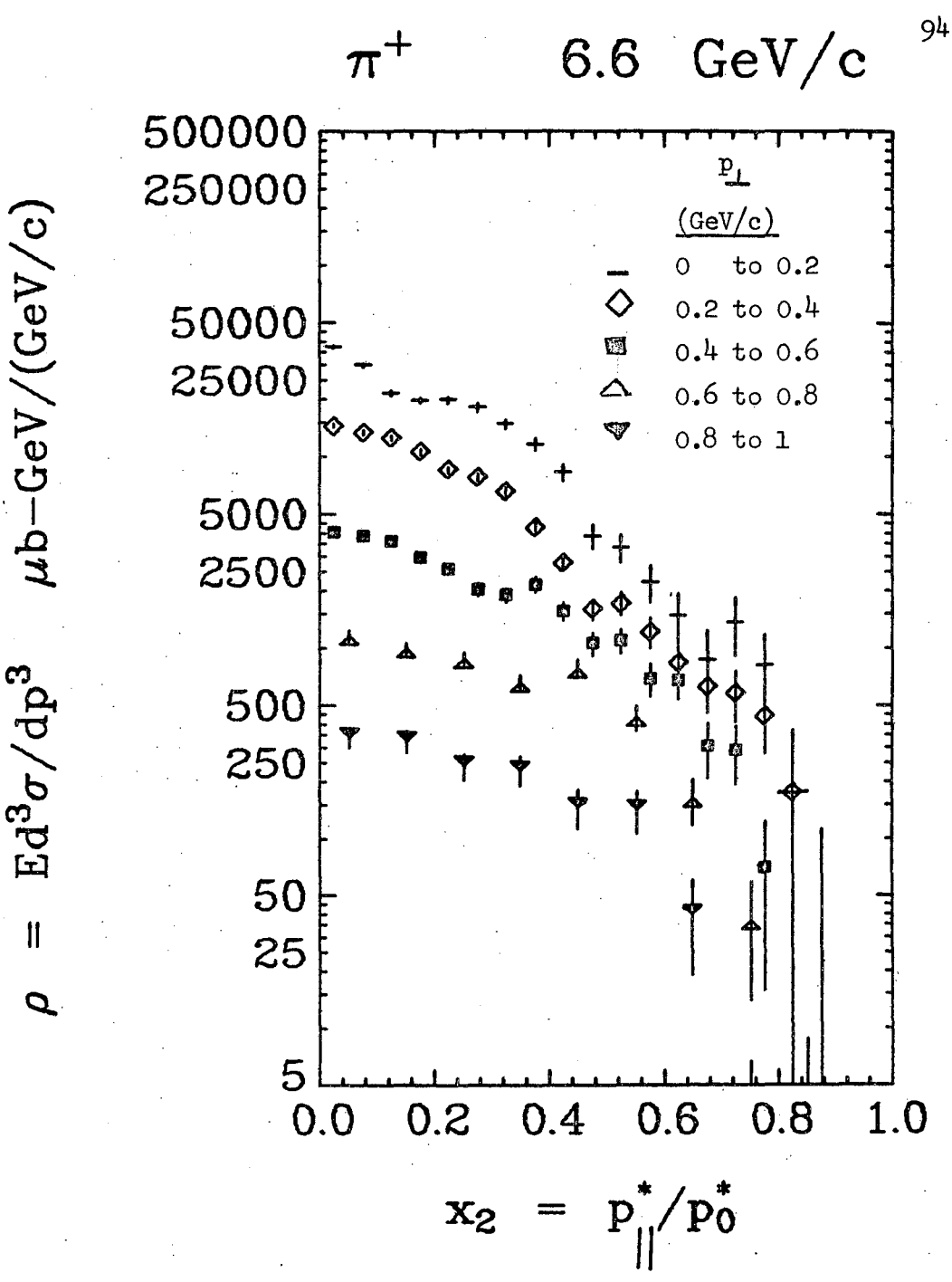

Fig. V.11 ρ vs. x_2 for 5 equal intervals in $p_\perp$ for the reaction $pp \rightarrow \pi^+ +$ anything at 6.6 GeV/c.

Please note: The data point is at the apex of the triangle symbols, viz. ▲ and ▼. It is at the center of all other symbols.

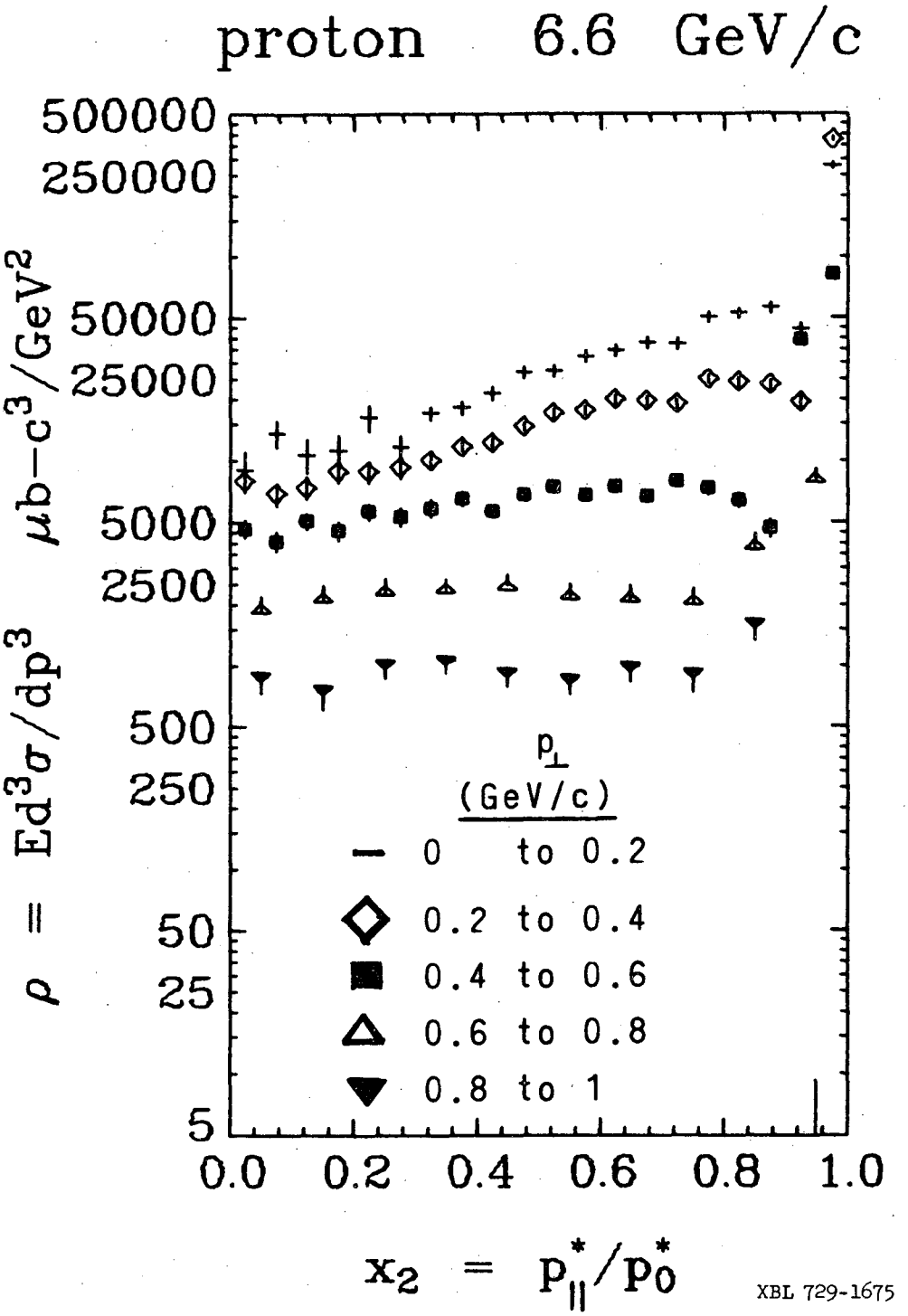

Fig. V.12 vs. x_2 for 5 equal intervals in $p_\perp$ for the reaction $pp \rightarrow p$ + anything at 6.6 GeV/c. [The elastic events are normalized to Foley's value of 11.79 mb (see section section III.D of text). Also note: the data point is at the apex of the triangle symbols, viz. △ and ▼.]

VI. SUMMARY AND CONCLUSIONS

We have shown that, for the reaction $pp \rightarrow \pi^- +$ anything, scaling occurs in the limiting fragmentation region for incident beam momenta as low as 6.6 GeV/c, i.e. the laboratory differential-cross-section $d^2\sigma/dp_\perp dp_\parallel$ is energy independent for $p_\perp \lesssim 0.6$ GeV/c and Feynman's $x \lesssim -0.4$. Scaling has not yet occurred in the central region ($p^*_\parallel \approx 0$), but the non-scaling term is not in disagreement with the $s^{-\frac{1}{4}}$ dependence derived from Mueller's optical theorem.

The reaction $pp \rightarrow \pi^+ +$ anything has been shown to behave quite differently. There is no scaling in the limiting fragmentation region: the laboratory differential cross section at 6.6 exceeds that at 28.5 GeV/c. In the central region scaling appears to have occurred for small transverse momentum, that is the structure function seems to be energy independent between 6.6 and 28.5 GeV/c. This may be fortuitous because the structure function then increases by about 50% from 28.5 to 1300 GeV/c.

For the reaction $pp \rightarrow p +$ anything, the structure function decreases in both the limiting fragmentation and central regions, with the greatest decline occurring in the central region. As we explained in section V.C, from a consideration of a $d\sigma/dy^*$ vs. y^* plot (where y^* is the C.M. rapidity), for ρ of a particle "x" to remain constant as the beam energy increases the number of particles of type "x" must increase with energy. However the total pp cross section remains constant, so that additional protons must come from nucleon anti-nucleon pairs. These are difficult to produce, and therefore ρ decreases with energy. Furthermore, as the energy increases fewer and fewer of those protons not coming from nucleon anti-nucleon pairs contribute near $x = 0$. This explains why ρ declines most rapidly near $x = 0$.

There are no such restrictions on pion production, so that pions are produced much more copiously, and therefore ρ does not decrease with energy for pions (except for π^+'s in the fragmentation region and acclerator energy region, as noted above).

ACKNOWLEDGMENTS

My parents have encouraged me throughout my education.

I wish to thank Professor Gerald A. Smith, now of Michigan State University, who origionally proposed the P65 experiment, and who provided guidance during the earlier part of my work. Thanks are also due to Professor William Chinowsky, who designed and built the proton beam used in our experiment, and also to Dr. A. B. Wicklund (now of Argonne National Laboratory), who along with Professor Smith, modified and improved the P65 beam. I also wish to thank Dr. Robert Jerome Manning, who began the analysis of the six-prong events reported on in this paper. In addition to Professor Smith and Drs. Wicklund and Manning, I wish to thank all the other participants in this experiment: William M. Dunwoodie (now of CERN TC Division), Eugene Paul Colton (now of the Lawrence Berkeley Laboratory), Peter Schlein, and Harold K. Ticho, all from UCLA; and Stanley Wojcicki (now of SLAC).

I deeply appreciate the very helpful discussions with Clifford Risk on the subject of inclusive reactions, including his suggestions for some of the plots contained herein. Margaret Garnjost suggested numerous improvements in this thesis. The guidance of Harry H. Bingham and Arthur H. Rosenfeld, during the later stages of this experiment, is acknowledged.

I thank Dr. Alan Rittenberg for his expert programming ability and willingness to help me.

Thanks are also due to the 72-inch bubble chamber and Bevatron operating crews, and to the many scanners who participated in this experiment. I also wish to thank our librarians and experiment coordinators: Peter Wohlmut, L. Reginald Paradis, Ruth Good, and Ellen Epstein.

I thank Professor Luis Alvarez for his support of this experiment.

I thank Idola Mc Cray and Caryl Schrock for typing this thesis.

This work has been supported, in part, by the United States Atomic Energy Commission.

APPENDICES

A. Dalitz-Pair Production

It is well known that 1.16 °/o of the time the π^0 decays into $e^+e^-\gamma$ instead of $\gamma\gamma$(Pa-1). The possibility exists that electrons may be confused with charged pions. We therefore estimate the cross section for Dalitz-pair production in our experiment.

If we ignore the deuteron and kaon, there are in general four reactions for each topology which produce π^0's. One reaction, reaction number 2 (see table B.1 for a list of reactions), is a one constraint reaction that produces a single π^0. The other three reactions are missing mass reactions, so that the number of π^0's must be estimated. First, we calculate the average number of charged pions in all missing mass reactions, taken as a group, with the use of an approximate knowledge of their relative production rates (see table 1). These rates are taken from ref. Co-1 or are estimated by us. Then, we estimate the average number of pions produced in missing mass reactions. This is done by looking at the number of pions produced in higher topology reactions for which we know the number of produced pions. For example, table III.6 shows that while 2, 3, 4, and 5π final states are produced in reasonable numbers, final states with 6 or more π's are extremely rare. We therefore estimate that the 2-prong missing mass reactions have, on the average, 3.5 π's in them (this may be somewhat high, since the 5π cross section seems fairly low). To get the average number of π^0's, we subtract the average number of charged π's from this number. A similar procedure is followed for the 4-prongs, except that we now only consider final states with 4 or more π's ,

Table A.1 Average number of π^o's for missing mass reactions

Topology	React no.[a]	$\sum$ [No. of chgd. π's $\times$ Fraction of mm reacts]	= Avg. no. of chgd. π's	Est.[b] no. of all π's	No. of[c] π^o's (diff.)
2-prongs	3	0 0.18	1.03	3.5	2.47
	5	1 0.61			
	9	2 0.21			
4-prongs	3	2 0.28			
	5	3 0.61	2.83	4.5	1.7
	9	4 0.11			
6-prongs	3	4 0.38			
	5	5 0.60	4.64	6.1	1.46
	9	6 0.02			

a. See table 1 of appendix B for a list of missing mass reactions

b. see text

c. est. no. of all π's - avg. no. of charged π's

Table A. 2 Dalitz Pair Production

Process	React No.[a]	Avg. no. of π^o's	$\sigma_{(Reaction)}$ (mb)	$=\sigma_{(\pi^o)}$ (mb)	$\times$ Fraction[b] of π^o's decaying into Dalitz-pairs	$=\sigma$ (1 or 2 Dalitz-pairs) (mb)
2 prongs → pseudo 4-prongs	2	1	2.06	2.06		
	3,5,9	2.5	9.9	24.8		
				26.9	0.0116	.312
4 prongs → pseudo 6-prongs	2	1	2.3	2.3		
	3,5,9	1.7	2.4	4.1		
				6.4	0.0116	.074
6-prong → pseudo 8-prong	2	1	.207	.207		
	3,5,9	1.46	.047	.069		.0032
				.276	0.0116	
4-prong → pseudo 8 prong		(see above)		6.4	.000035	.00044
						.0036
8-prongs → pseudo 10 prong	all	1 (?)	.022	.022	.0116	.0002
6-prongs → pseudo 10-prong		(see above)		.276	.000035	.00002
						.0002

a See table 1 of appendix B for a list of reaction numbers.

b. from Pa-1

when we estimate the number of π^0's that are produced.

We now are in a position to calculate the π^0 production cross section for each topology. The results of this calculation are presented in table 2. Then, from the fraction of π^0's decaying into Dalitz pairs, we calculate the Dalitz-pair cross-section (table 2).

Sections IV and V show that pions like to cluster about $p^* = 0$. Therefore, let us consider the decay of a π^0 with $p^* = 0$. Although, from kinematics, the e^+e^- system can have a mass as high as the π^0-mass, in fact it usually has a very small mass (Sa-1). This is because the virtual γ prefers to be near its mass-shell value. Therefore, the e^+e^- system usually carries away about half the energy of the π^0-mass, in the π^0 rest frame (which we are assuming to also be the overall C.M. of the reaction). Let us consider the case in which this energy is equally divided between the electron and positron. The electron will therefore have an energy of about $\frac{1}{4}m_{\pi^0}$. The Lorentz transformation equation from the C.M. to the lab is

$$p_{\parallel}(\text{lab}) = \bar{\gamma} p^*_{\parallel} + \bar{\gamma} e^*. \qquad \text{A.1}$$

Consider an electron going directly forward. Because of the light mass of the electron, its energy and momentum are almost equal, and we can therefore write

$$p_{\parallel}(\text{lab}) \approx (\bar{\gamma} + \bar{\gamma})\times\tfrac{1}{4}m_{\pi^0} = (2.01 + 1.75)\times\tfrac{1}{4}m_{\pi^0} = 127\ \text{MeV/c}, \qquad \text{A.2}$$

where $\bar{\gamma}$ and $\bar{\gamma}$ refer to the velocity of the C.M. as seen in the laboratory, for pp interactions at 6.6 GeV/c. Similarly, if the electron comes directly backward, we write

$$p_{\parallel}(\text{lab}) = (-2.01 + 1.75)\times\tfrac{1}{4}m_{\pi^0} = -9\ \text{MeV/c}. \qquad \text{A.3}$$

We should point out that the e^+e^- mass is not small compared to the electron mass, so that one electron may carry away considerably more energy than the other. In fact, the energy partition is fairly uniform (fig. 8 of ref. Sa-1). Therefore, one electron may have a laboratory momentum up to 254 MeV/c. Of course, in this case the other electron would be practically at rest in the laboratory.

From the above considerations, we crudely assume a linear fall-off in the e^+ production-cross-section from 0 to 127 MeV/c. This means that 60 °/o of the time, either the electron or the positron will have a momentum of less than 50 MeV/c. Now, our scanning instructions state that a track is to be considered part of a Dalitz-pair if it curls up in the bubble chamber. This means that the maximum radius, for our approximately 40 cm wide chamber, is 10 cm. At 17 kilogauss, this is a momentum of 50 MeV/c. We therefore can reject 60 °/o of the Dalitz-pairs by just glancing at the scan table. In addition, practically all these electrons can be distinguished from pions by their bubble densities. This means that for the 4-prongs, where the bubble density was determined, there should be no Dalitz-pairs in our sample.

If no Dalitz-pairs were rejected, table 2 indicates that we would have a 0.074mb (10°/o)contamination of our 6-prong sample. Even this is not disasterous when compared to the 13 °/o error in the 6-prong cross section. However, for the reasons just stated, we only expect a 4 °/o contamination of our 6-prong sample. Similarly, we only expect a 6 °/o contamination of our 8-prong sample and a 0.8 °/o contamination of our 10-prong sample. These corrections are very much smaller than the statistical errors of the cross sections reported for these topologies.

Our 4-prong distributions should be similarly unaffected. If 60 °/o of the Dalitz-pairs are rejected by just glancing at the event on the scan table, there is only 1 °/o contamination.

We therefore conclude that Dalitz-pair production does not affect our results.

B. Reliability of 4-constraint Fits

It is well known that, for bubble chamber events, four constraint fits are quite reliable. This is illustrated by fig. 1. Most of the spurious 1 and 0 constraint fits are eliminated by the application of bubble density information, while the 4-constraint fits all survive.

For a system in which the beam and target are identical particles, the outgoing particles must have identical distributions with respect to the beam or target. This means symmetry about the 90° scattering angle in the overall C.M. system.

This symmetry is observed for the primary 4-constraint reaction, reaction number 1 (see table 1 for a list of reactions), but it is not observed the most important 1-constraint reactions. For example, the reactions $pp \rightarrow pp\,\pi^+\pi^-\pi^o$ and $pp \rightarrow p\,\pi^+\pi^+\pi^-n$ have about a 10 $^{o}/_{o}$ forward-backward assymetry (even after bubble density criteria are imposed).

Ambiguities among 4-C fits do occur (see table 2). The fact that there are many more K and deuteron 4-C fits ambiguous with $pp \rightarrow pp\,\pi^+\pi^-$, than there are unambiguous K and deuteron 4-C fits, coupled with the fact that the K and deuteron cross sections are believed to be small, leads us to conclude that most of these ambiguous K and d fits are spurious. Discarding these K and d fits, we are left with a 7 $^{o}/_{o}$ ambiguity level (and therefore a maximum error of $3\frac{1}{2}$ $^{o}/_{o}$) in the reaction $pp \rightarrow pp\pi^+\pi^-$. This is <u>before</u> bubble density criteria are imposed. Ambiguity levels among 1-constraint fits are much worse. (see table 3).

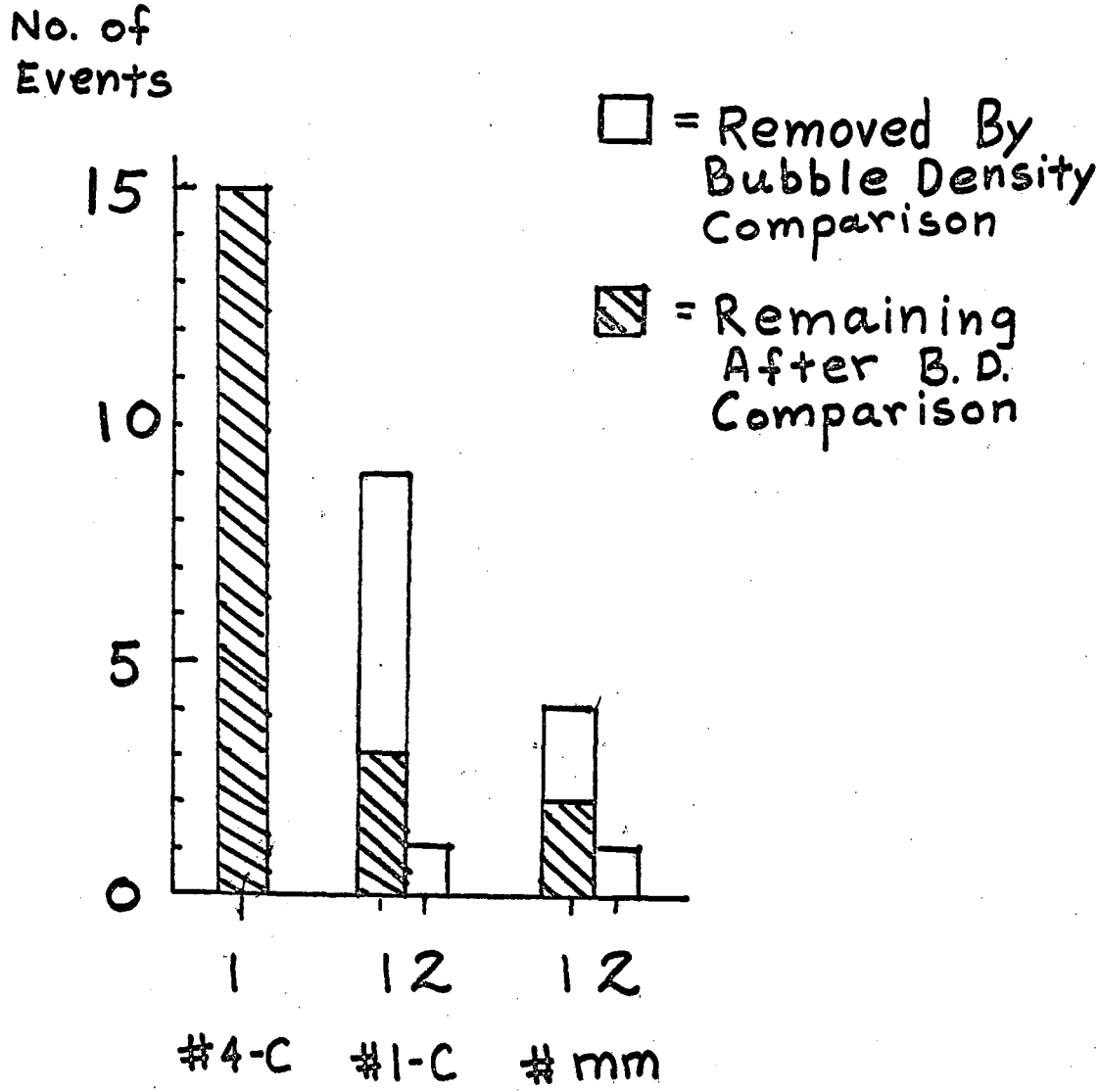

Fig. B.1 The effect of comparing actual and predicted bubble densities for a sample of 15 4-prong events having one and only one 4-constraint fit. The comparison is performed by looking at events on the scan table.

Table B.1 Reactions for which fits are attempted - 2, 4 and 6-prong non-strange topologies

Reaction No.	No. of Constraints[a]	2-prongs (event type 2)	4-prongs (event type 3)	6-prongs (event type 4)
1	4	$pp \rightarrow pp$	$pp\pi^+\pi^-$	$pp\pi^+\pi^+\pi^-\pi^-$
2	1	$pp\pi^o$ [b]	$pp\pi^+\pi^-\pi^o$	$pp\pi^+\pi^+\pi^-\pi^-\pi^o$
3	0	pp mm[c]	$pp\pi^+\pi^-$ mm[c]	$pp\pi^+\pi^+\pi^-\pi^-$ mm[c]
4	1	$p\pi^+$ n	$p\pi^+\pi^+\pi^-$ n	$p\pi^+\pi^+\pi^+\pi^-\pi^-$ n
5	0	$p\pi^+$ mm[d]	$p\pi^+\pi^+\pi^-$ mm[d]	$p\pi^+\pi^+\pi^+\pi^-\pi^-$ mm[d]
6	4	$d\pi^+$	$d\pi^+\pi^+\pi^-$	$d\pi^+\pi^+\pi^+\pi^-\pi^-$
7	1	$d\pi^+\pi^o$	$d\pi^+\pi^+\pi^-\pi^o$	$d\pi^+\pi^+\pi^+\pi^-\pi^-\pi^o$
8	0	$d\pi^+$ mm[e]	$d\pi^+\pi^+\pi^-$ mm[e]	$d\pi^+\pi^+\pi^+\pi^-\pi^-$ mm[e]
9	0	$\pi^+\pi^+$ mm[f]	$\pi^+\pi^+\pi^+\pi^-$ mm[f]	$\pi^+\pi^+\pi^+\pi^+\pi^-\pi^-$ mm[f]
10	4	———	ppK^+K^-	$ppK^+K^-\pi^+\pi^-$
11	1	———	$ppK^+K^-\pi^o$	$ppK^+K^-\pi^+\pi^-\pi o$
12	0	———	ppK^+K^- mm	$ppK^+K^-\pi^+\pi^-$ mm

a. from kinematic fitting

b. Therefore $pp \rightarrow pp\pi^o$ is also referred to as react. 2, E.T.2

c. mm mass ($2\pi^o$'s)

d. mm mass (nπ^o)

e. mm mass ($2\pi^o$'s)

f. mm mass (2n's

Table B.2 A sample of 4-prong events having at least one 4-constraint fit (before bubble density criteria imposed).

	Number of events	
Only one 4C fit		
react. 1(π)[a]	1185	
" 6(d)	11	
10(K)	7	
		1203
Two 4-C fits		
both are react. 1(π)	93	
reacts. 1 and 6 (π,d)	118	
reacts. 1 and 10(π,K)	30	
reacts. 6 and 10(d,K)	1	
		242
Three 4-C fits		15
More than three 4-C's		3
Total		1463[b]

a. see table 1 for a list of reactions by reaction no.

b. composed of 824 S.R. events and 639 F'stein events - a ratio not too different from the almost 50/50 ratio of the entire 4-prong sample. The S.R. events are somewhat more ambigious than the F'stein events.

Table B.3 A sample of 4-prong events having no 4-constraint fits and at least one 1-constraint fit. (before bubble density are criteria imposed).

	Number of events	
Only one 1-C fit		
react. 2 (π)[a]	455	
4 (n)	979	
7 (d)	154	
11 (K)	9	
		1597
Two 1-C fits		
two react. 2's (π)[a]	51	
reacts. 2 and 3 (π,n)	434	
two react. 4's (n)	251	
reacts 2 and 7 (π,d)	160	
reacts 4 and 7 (n,d)	151	
reacts 2 and 11(π, K)	7	
reacts 4 and 11(n, K)	6	
2 reacts 7 (d)	2	
reacts 7 and 11(d, K)	5	
2 reacts 11 (K)	1	
		1068
Three 1-C fits		566
More than three 1-C fits		376
Total		3607

a. see table 1 for a list of reactions by reaction number.

Table B.3 (continued)

b. composed of 2302 S.R. and 1305 F'stein events. The ratio of S.R/F'stein is somewhat different than in table 8/19-2 because some 4-C S.R. events were wrongly rejected. Most were later caught and measured on the F'stein's.

REFERENCES

Ab-1. H. D. I. Abarbanel, Phys. Lett. 34B, 69 (1971)

Ab-2. M. A. Abolins et al., Phys. Rev. Lett. 25, 126 (1970)

Ak-1. C. W. Akerlof et al., Phys. Rev. D3, 645 (1971)

Al-1. Alston et al., Alvarez Group IBM Program PANAL, Lawrence Berkeley Laboratory - Alvarez Group Memo 358, Feb. 1963

Al-3. J. V. Allaby et al., High Energy Particle Spectra from Proton Interactions at 19.2 GeV/c, CERN yellow report NP 70-12, 23 Apr. 1970

Al-4. J. V. Allaby et al., Comparison of Momentum Spectra of Secondary Particles Produced in Proton-Proton Collisions at 14.2, 19.2, and 24.0 GeV/c, Contributed to the Fourth International Conference on High-Energy Collisions, Oxford, England, 5-7 April 1972, CERN report, 24 March 1972 and to be published in Ox-2.

Al-5. B. Alper et al. (British-Scandinavian Collaboration), Inclusive Particle Production in the Rapidity Range 0 to 1 at the CERN ISR, presented at the XVIth International Conference on High Energy Physics, Batavia, Ill., Sept. 1972

An-4. J. A. Anderson and D. B. Smith, A Method for Separation of the Proton and Pi Plus Momentum Distributions produced in Proton-Proton Interactions, Lawrence Berkeley Laboratory - Group-A Physics Memo 673 (unpublished), Dec. 1968

Be-1. J. Benecke et al., Phys. Rev. 188, 2159 (1969): also see T. T. Chou and C. N. Yang, Phys. Rev. Lett. 25, 1072 (1970)

Be-3. J. V. Beaupre et al. (ABBCCHW Collaboration), Phys. Lett. 37B, 432 (1971)

Be-6. A. Bertin et al. (Bologna Group), Negative Particle Production at the CERN Intersecting Storage Rings, CERN Internal Report NP 71-20, 21 Dec. 1971

Be-7. Edmond L. Berger, Phenomenology of Inclusive Reactions (Rapporteur's Review delivered at the International Colloquium on Multiparticle Dynamics, Helsinki, May 25-28, 1971), Argonne National Lab. ANL/HEP-7134, July 1971

Be-12. Edmond L. Berger et al., Phys. Rev. Lett. 20, 964 (1968)

Be-13. Odette Benary, LeRoy R. Price, and Gideon Alexander, NN and ND Interactions (above 0.5 GeV/c) - A Compilation, Lawrence Berkeley Laboratory report UCRL-20000 NN (unpublished), Aug. 1970

Co-1. Eugene Paul Colton, Pion Production in Proton-Proton Interactions at 6.6 GeV/c (Ph. D. Thesis), UCLA-1025, June 1968

Co-2. Eugene Colton and Alan R. Kirschbaum, Study of $|T_2| = 3/2$ $\Delta(1238)$ Production in pp Interactions at 6.6 GeV/c, Lawrence Berkeley Laboratory LBL-730, Feb. 1972 (to be submitted to Phys. Rev.)

Co-3. Eugene Colton et al., $pp \rightarrow \Delta^{++}p\pi^-$: OPE, pole extrapolation and the Deck Effect, UCLA-1023 (1968).

Co-4. Eugene Colton et al., Phys. Rev. Lett. 21, 1548 (1968)

Co-5. Eugene Colton and Eugene Gellert, Phys. Rev. D1, 1976 (1970)

Co-6. Eugene Colton et al., Phys. Rev. D3, 1063 (1971)

Cr-1. David J. Crennel et al., Phys. Rev. Lett. 28, 643 (1972)

Da-2. Proceedings of the International Conference on Inclusive Reactions Held at the University of California, Davis, Feb. 4 and 5, 1972; Edited by R. L. Lander (University of California, Davis, 1972)

Da-3. O. I. Dahl, T. B. Day, and F. T. Solmitz, SQUAW - Kinematic Fitting Program, Lawrence Berkeley Laboratory - Group-A programming note P-126, Aug. 1965

Di-1. A. N. Diddens and K. Schlupmann, Particle Production in Proton-Proton Interactions, CERN report, 1971 (to be published in Landolt-Bornstein)

Du-1. William M. Dunwoodie, Strange Particle Production in Proton-Proton Interactions at 5.4 and 6.6 GeV/c (Ph. D. Thesis), UCLA-1033, Dec. 1968

Du-2. W.M. Dunwoodie et al., One-Particle-Exchange Analysis of the Reactions $pp \rightarrow YNK$ at 5.4 and 6.6 GeV/c, in Proceedings of the XIV International Conference on High Energy Physics, Vienna, Austria, 1968 (to be published)

Fe-1. Richard P. Feynman, The Behavior of Hadron Collisions at Extreme Energies, in High Energy Collisions / Third International Conference / Stony Brook, 1969, edited by C. N. Yang and others (Gordon and Breach, New York, 1969); and also Richard P. Feynman, Phys. Rev. Lett. 23, 1415 (1969)

Fe-2. T. Ferbel, Phys. Rev. Lett. 29, 448 (1972)

Fe-3. Thomas Ferbel (Dept. of Physics and Astronomy, Univ. of Rochester), personal communication, June 1972 (Ferbel says that the 6.6 data point is slightly misplotted on his graph.)

Fo-1. K. J. Foley et al., Phys. Rev. Lett. 11, 425 (1963)

Fo-2. K. J. Foley et al., Phys. Rev. Lett. 19, 857 (1967)

Fr-1. W. R. Frazer et al., Rev. of Modern Phys. 44, 284 (1972)

Ga-1. Margaret Alston-Garnjost, Energy Dependence of Inclusive Distributions in Pion Induced Reactions, in Da-2, pp 182, and also Lawrence Berkeley Laboratory report LBL-735, Feb. 1972

Ga-2. Margaret Alston-Garnjost et al., Phys. Lett. 39B, 402 (1972)

Ga-5. Margaret Alston-Garnjost (Lawrence Berkeley Laboratory), personal communication, Sept. 1972

Ge-1. Eugene Gellert et al., Phys. Rev. Lett. 17, 884 (1966)

Ge-2. Eugene Gellert, The Inclusive Reaction $pp \rightarrow \pi^-$ + anything at 6.6 GeV/c Compared to Higher Energies, in Da-2, pp 198, also Lawrence Berkeley Laboratory report LBL-784, Feb. 1972

Ha-1. J. D. Hansen et al., Compilation of Cross Sections: I - Proton Induced Reactions, CERN/HERA 70-2 (unpublished), Oct. 1970

Ha-2. J. Hanlon (Vanderbilt Univ, Tenn., and Brookhaven National Lab.), personal communication, Aug. 1972

Ki-1. Robert Ronald Kinsey, Zero Strangeness Resonance Production in 6 GeV/c Proton-Proton Collisions (Ph. D. Thesis), Lawrence Berkeley Laboratory UCRL-17704, June 1968

Kr-1. A. D. Krisch, Phys. Rev. Lett. 19, 1149 (1967)

La-1. M. E. Law et al., A Compilation of Data on Inclusive Reactions, Lawrence Berkeley Laboratory LBL-80 (a Particle Data Group publication), Aug. 1972

Ma-2. Z. Ming Ma and Eugene Colton, Phys. Rev. Lett. 26, 333 (1971)

Mo-1. K. C. Moffeit et al., Phys. Rev. D5, 1603 (1972)

Mu-1. H. J. Mück et al., Phys. Lett. 39B, 303 (1972)

Mu-2. A. H. Mueller, Phys. Rev. D2, 2963 (1970)

Mu-3. H. J. Mück et al., Inclusive Particle Production in pp Interactions at 12 and 24 GeV/c: I. The Central Region, II. The Proton Fragmentation Region, "Interner Bericht" DESY F1-72/1, April 1972, and submitted to Ox-2

Ox-2. The Fourth International Conference on High Energy Collisions, St. Catherine's College, Oxford, U.K., 5-7 April 1972, Conference Proceedings (to be published)

Pa-1. Particle Data Group, Rev. of Modern Phys. 43, No. 2 part II (1971) and also Phys. Lett. 39B, No. 1 (1972)

Pa-3. R. S. Panvini et al., Phys. Lett. 38B, 55 (1972)

Po-1. POOH, A Spiral Reader Filter Program (ca. 1967), No writeup exists - see G. Lynch, J. J. Wilson and others in Group-A of the Lawrence Berkeley Laboratory for details.

Qu-1. C. Quigg, Inclusive Reactions, Stonybrook, in Particles and Fields-1971, edited by A. C. Melissinos and P. F. Slattery (Am. Inst. of Physics, New York, 1971), pp 40

Ra-1. G. Ranft and J. Ranft, Inclusive Reactions: Review of Models on MultipParticle Production, Karl-Marx University TUL-41, Nov. 1970 (based on lectures delivered to the Symposium on High Energy Physics, Kuhlungsborn, DDR, 12-24 Oct. 1970)

Ra-2. L. G. Ratner et al., (presented by A. D. Krisch), Inelastic Proton-Proton Scattering at Very High Energy, in Particles and Fields-1971 (see Qu-1 for details). pp 99

Sa-1. N. P. Samios Phys. Rev. 121, 275 (1961)

Se-1. J. C. Sens, talk at the Oxford Conf., April 1972, submitted to Ox-2

Sh-1. W. D. Shephard et al., Phys. Rev. Lett. 27, 1164 (1971) (Errata, ibid. 28, 260 (1972))

Si-1. W. H. Sims et al., Nucl. Physics B41, 317 (1972)

Sm-1. Dennis Baird Smith, Charged Pion Production in Proton-Proton Interactions between 13 and 28.5 GeV/c (Ph. D. Thesis), Lawrence Berkeley Lab. UCRL-20632, March 1971

Sm-2. Dennis Baird Smith (CERN), personal communication, Oct. 1971

Sm-3. Dennis B. Smith, Robert J. Sprafka, and Jared A. Anderson, Phys. Rev. Lett. 23, 1064 (1969)

So-1. F. T. Solmitz, A. D. Johnson, and T. B. Day, Three View Geometry Program (TVGP), Lawrence Berkeley Laboratory Group-A Programming Note P-117, June 1965

Ve-1. J. C. Vander Velde, Phys. Lett. 32B, 501 (1970)

We-1. W. A. Wenzel, The Bevatron External Proton Beam, Lawrence Berkeley Laboratory - UCRL-10868 (unpublished)

Wi-1. K. G. Wilson, Acta Physica Austriaca 17, 37 (1963)

Yo-2. J. E. Young, Inclusive Reactions; A Survey, M. I. T. Center for Theor. Phys. Publ. No. 227, Sept. 1971 (Lectures given at the Torino Summer School, Torino, Italy, 1971)

---

a. Review Articles: Be-7, Fr-1, Qu-1, Ra-1, Yo-2

b. Data Compilations: Di-1, La-1

c. Conferences mainly on Inclusive Reactions: Da-1, Ox-2

d. Articles on Exclusive Reactions for this Experiment: Be-12, Co-1 to Co-6, Du-1, Du-2, Ge-1, and Ma-2.

e. Articles on Inclusive Reactions for this experiment: Ab-2, Ge-2.

f. Brookhaven pp data (28.5 GeV/c): Ha-2, Pa-3, Si-1.

TECHNICAL INFORMATION DIVISION
LAWRENCE BERKELEY LABORATORY
UNIVERSITY OF CALIFORNIA
BERKELEY, CALIFORNIA 94720